UNIVERSITÀ DEGLI STUDI DI PADOVA

DIPARTIMENTO DI SCIENZE CHIMICHE

CORSO DI LAUREA MAGISTRALE IN CHIMICA

TESI DI LAUREA MAGISTRALE

Thermocatalysis for green hydrogen production: tuning oxygen exchange capability in perovskites

Relatore: Chiar.ma Prof.ssa Antonella Glisenti
Controrelatore: Chiar.ma Prof.ssa Marcella Bonchio

Laureando: Michele De Rocco
Matricola: 2057622

Anno Accademico 2022/2023

We are drowning in information, while starving for wisdom. The world henceforth will be run by synthesizers, people able to put together the right information at the right time, think critically about it, and make important choices wisely.

Edward O. Wilson

Contents

Chapter 1

Introduction

1.1 The need for new energy carriers

With global temperatures constantly increasing at rates never seen before,[1] fossil fuels are being disregarded and many countries are trying to replace them with less impacting energy sources. Coal, oil and gas are slowly giving way to other forms of energy, such as nuclear (with the consequent issues about waste disposal, even for most recent versions of nuclear reactors) and renewable energies (solar, wind, hydroelectric, geothermic and so on).[2]

One of the main issues, though, is that while fossil fuels can be used both as energy source and energy carrier (they are indeed delivered to any final user in various refined compositions such as petrol, gasoline, gas), some renewable energy sources have an unstable electricity production that is transmitted in a small amount of time to the device that needs it. What if we generate a lot of electricity when it is not needed, or need more when the natural sources are not available? Electricity could be stored in batteries, but producing batteries for the whole world is difficult, and even the growing demand for just car batteries is thought to be sustainable only if the lithium content per kW h is decreased.[3] Besides, delivery would still be an issue in terms of weight and size (the energy density, compared to fuels, is very low).[4]

For energy storage and delivery various synthetic fuels are being taken into account as possible energy carriers: energy from various renewable sources (in form of electricity, heat or light) can be used to sustain unfavourable reactions, activating molecules such as CO_2, H_2O and N_2, transforming them in products with high energy density as CH_4 or other hydrocarbons, H_2 and NH_3. These chemicals can then be stored, delivered and consumed in high-efficiency systems as Fuel Cells.

Furthermore, the byproducts of the involved reactions (usually oxidations) are the same small molecules mentioned before: with adequate capture systems, these could be then converted again to fuels (always employing renewable or sustainable energy sources), realizing a closed system with net-zero emissions.[5]

1.1.1 Why hydrogen?

Hydrocarbons, hydrogen, ammonia all have various pros and cons, in terms of compatibility with present systems, toxicity, products (e.g. CO_2 for hydrocarbons), ease of storage and so on.

Hydrogen in particular has several interesting positive aspects: it has one of the highest energy densities if compared to other fuels (about 33kWh/kg),[6] no dangerous or toxic byproducts are produced in its consumption (steam being the only one) and there are many efficient technologies already developed for its use. At the moment, the employment of this carrier faces three main issues, two of which are the difficulty of storage (it is usually stored in tanks at a very high pressure, about 700 atm) and the flammability in the case of liquid/pressurized hydrogen. These problems might be solved, at least partially, by innovative storage solutions such as incorporation in metal alloys or adsorption on porous structures.[7]

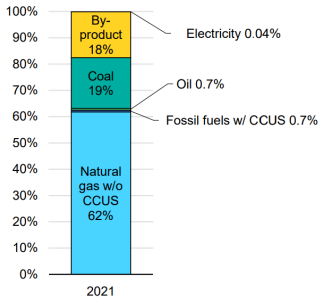

Figure 1.1: Sources of hydrogen production.[8]

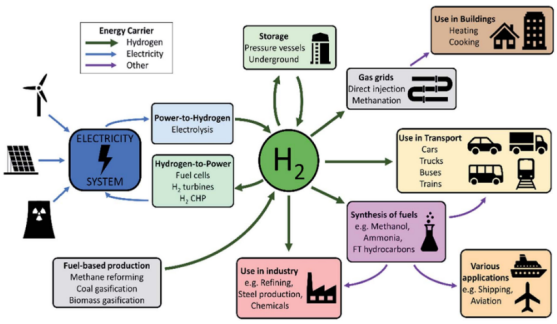

Figure 1.2: Some of the various applications of hydrogen.[9]

The third issue is the key point that led to the writing of this thesis: nowadays, the vast majority of hydrogen used for all applications (be it energy or chemicals) comes from hydrocarbons. Almost of 82% of it is the so-called "grey" hydrogen, produced from natural gas through reforming (about 62%) or extracted from coal: this means that the CO_2 emissions are not lowered by the usage of this type of fuel. Almost 18% is obtained as byproduct of other reactions. A small fraction (0.7%), then, is "blue" hydrogen, also reformed from hydrocarbons, but with Carbon Capture systems.

Finally, just 0.04% is the true "green" hydrogen, obtained through water splitting fuelled by renewable energies (mainly electricity, through electrolysis), therefore without contributing to the emission of pollutants into the environment.[8] Green approaches to hydrogen production through electrolysis are being developed, with even the use of sea water.[10]

1.1.2 Green hydrogen production

Besides the aforementioned electrolysis, other ways of splitting water involve solar light (photolysis) and heat from the Sun or other sources (thermolysis). These routes are less explored than electrolyzers and there is plenty of room for improvement.[11] In particular, this thesis will deal with catalysts for thermocatalytic water splitting, thought to be employed in solar concentrators.

In such structures, light from the Sun is reflected on curved mirrors and directed on the catalyst placed in the focal point, reaching temperatures up to 2000 °C.[12] The catalyst is usually a reducible oxide that can release part of the oxygen in a reaction of thermal reduction, with general equation

$$\mathrm{MO}_x \xrightarrow{\Delta} \mathrm{MO}_{x-\delta} + \frac{\delta}{2}\mathrm{O}_2$$

After that, a second step involves an oxidation from water, bringing the oxide back to its original composition:

$$\mathrm{MO}_{x-\delta} + \delta\mathrm{H}_2\mathrm{O}_{(g)} \longrightarrow \mathrm{MO}_x + \delta\mathrm{H}_2$$

This second reaction allows the regeneration of the starting material. These two reactions form a thermocatalytic cycle which, if repeated, can produce good amounts of hydrogen gas.

Various oxides are used for this kind of reactors, identifying two main categories: volatile and non-volatile. In the first case, the reduced oxide is in the gas phase, having to undergo a solid-to-gas transition followed by a gas-to-solid one (it is the case of ZnO/Zn, GeO_2/GeO and others), while in the second the oxide stays in the same phase (usually solid) in all steps (for oxides such as Fe_3O_4, CeO_2, perovskites and so on).[12]

Despite having high theoretical capacity of hydrogen production (since the reduction is stoichiometric, releasing a great amount of oxygen), volatile oxides are very difficult to deal with, because the phase transition (mainly in the gas-to-solid step) requires precise control of the morphology in order to avoid sintering and to obtain a material that can exchange oxygen again as in the first step. Catalyst synthesis usually follows precise steps to produce a material in the desired phase and structure, while reaction conditions might not be favourable to the restoration of the same properties.

Materials employed in non-volatile processes, on the contrary, can retain their morphology, even though they might undergo some phase changes in the case of stoichiometric reduction of the oxides. This is avoided in the case of partial reduction of the material, in which metal ions change their oxidation state without re-arranging the crystal lattice, and in the case of substoichiometric oxygen release, in which vacancy formation allows the exchange of a part of the reticular oxygen without altering the structure. This will be further discussed in section 1.3.[13,14] For this reason, this simpler approach has been chosen, focusing on tuning the activity of materials whose morphology is stable.

1.2 State of the art

For non-volatile cycles, three main categories of catalysts are used: ferrite-, ceria-, and perovskite-based oxides.

In the first case, the starting point is Fe_3O_4, which can be doped with various cations to increase reducibility and enhance stability (Mg, Mn, Co, etc.); the cycle oscillates between Fe_3O_4 and FeO, with a stoichiometric reduction of the material.[15] The best results have been obtained with Nickel-doped ferrites, with reduction temperatures below 1400-1500 °C, but with low cycling stability.[16,17] The obtained H_2 per cycle is ∼15mL/g.[18]

CeO_2 reduction, on the other hand, happens with a non-stoichiometric release of oxygen, in a $CeO_2/CeO_{2-\delta}$ redox pair.[19] Reduction temperature lays between 1400 and 1500 °C, as for ferrites. The obtained hydrogen depends on the dopants and the support material, spanning between less than 4 mL/g for simple CeO_2 reduced at 1400 °C[20] and more than 8 mL/g for Zr-doped ceria.[21]

In a similar manner, even perovskite oxides have a step of reduction that consists mainly in the formation of oxygen vacancies in the crystal lattice and the general catalytic couple is $ABO_3/ABO_{3-\delta}$. Both reduction temperature and hydrogen production can vary heavily with the composition, with the former falling between 1000 °C and 1400 °C and the latter between 2 mL/g and 20 mL/g.[22]

It can be observed that, with the objective of keeping temperatures relatively low, perovskites are the best candidates. In particular, in two recent works by Pérez et al.[23] and Orfila et al.[24] two perovskites, respectively $La_{0.8}Al_{0.2}NiO_3$ and $La_{0.8}Sr_{0.2}CoO_3$, prove themselves capable of producing good amounts of hydrogen (4.4 mL/g and 15.8 mL/g respectively) at low reduction temperature (800 °C and 1000 °C).

Some of the most relevant materials are detailed in table 1.1, focusing on reduction temperature and oxygen release. Where it has not been declared in literature, the released

oxygen is calculated assuming a stoichiometric 2:1 ratio between hydrogen and oxygen and denoted with an asterisk.

Table 1.1: State-of-the-art materials for thermocatalytic water splitting.

Material	T_{red} (°C)	H_2 (mL/g STP)	O_2 (mL/g STP)
$Ni_xFe_{3-x}O_4$[18]	1400	11	5.5*
$Ni_xFe_{3-x}O_4/ZrO_2$[18]	1400	15	7.5*
CeO_2[21]	1450	3.8	1.9*
$Ce_{0.8}Zr_{0.2}O_2$[25]	1400	9.5	4.8*
$LaCoO_3$[26]	1300	/	8.3
$La_{0.65}Sr_{0.35}MnO_3$[27]	1400	/	3.7

1.3 Perovskites

Perovskites are a type of metal oxide with general formula ABO_3. A and B are two cations, usually with A larger than B. This class of materials is named after $CaTiO_3$, which in turn gets its name from Lev Perovskij (1792-1856), a Russian mineral collector. The crystal system of $CaTiO_3$ is cubic (space group *Pm3m-*O_h), with 12-fold coordination for Ca and 6-fold for Ti, as in figure 1.3.[13]

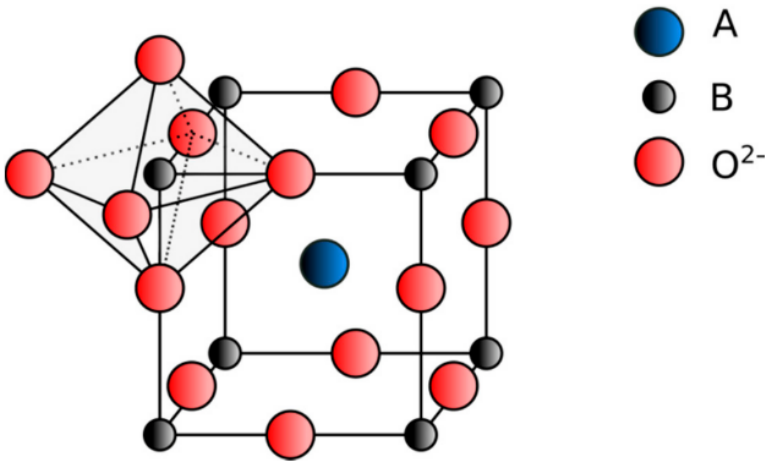

Figure 1.3: Typical ABO_3 perovskite structure.[22]

Nevertheless, the composition is greatly variable, with many dodeca-coordinated cations that can occupy the A-site (such as Sr^{2+}, Ba^{2+} and several rare earths as La^{3+}, Ce^{3+}, Nd^{3+} and so on) and many hexacoordinated cations in the B-site (often transition metals,

for example Co^{3+}, $Mn_3{}^+$, Ti^{4+}). The charge balance needs to be maintained, but +3/+3, +2/+4 and +1/+5 combinations can be found.

Sometimes, two or more ions can contribute to the total composition of one site: this is the case of *doped* perovskites, with general formula $A^{i}_{1-x}A^{ii}_{x}BO_3$ or $AB^{i}_{1-x}B^{ii}_{x}O_3$.

1.3.1 Distortions

Despite the cubic perovskite being the standard one, the same coordination numbers can be arranged in different structures in the case of ions with different sizes, with orthorhombic, rhombohedral, tetragonal, monoclinic, and triclinic geometry. In 1926, V. M. Goldschmidt derived a tolerance factor that could foresee the geometry of the desired phase starting from the ionic radius of the metals:[28]

$$t = \frac{r_A + r_O}{\sqrt{2}(r_B + r_O)} \tag{1.3.1}$$

The ideal perovskite ($SrTiO_3$) has $t = 1.00$ and cubic structure. Deviation from this value correspond to a higher stability of other geometries:[29]

- $t > 1$: hexagonal;
- $0.89 < t \leq 1$: cubic;
- $0.8 < t \leq 0.89$: orthorhombic and rhomboedral;
- $t \leq 0.8$: various structures, such as ilmenite.

1.3.2 Nonstoichiometry

In perovskites, the deficiency of a part of the ions in the crystal lattice is fairly common, leading to substoichiometric compounds. In particular, oxygen vacancies are the most common, usually leaving regular holes in the lattice.[13]

The amount of vacancies depends on the composition of the perovskite, being a very tunable property. In particular, in lanthanum perovskite doping in the A-site with alkaline earth metals allows a higher degree of oxygen deficiency because of the different charge. Among them, strontium is the most used because of the high size compatibility: ionic radius for dodeca-coordinated La^{3+} is 1.50 nm, while for Sr^{2+} it is 1.58 nm.[30] Furthermore, the charge difference between strontium and lanthanum is compensated by oxidation of B-site cations (usually in +3 oxidation state in the case of $LaMO_3$), with the formation of M^{4+} species which are more readily reduced.[14]

Good results have been observed even with just 20% of strontium content in the A-site,

with an increasing oxygen release with higher percentages.[31] It has to be noted, though, that higher strontium content results in a more difficult oxidations step (a higher pressure of water vapour is needed).[32] For this reason, only perovskites with A-site composition of $La_{0.8}Sr_{0.2}$ and $La_{0.6}Sr_{0.4}$ have been taken into account.

1.4 Investigated materials

The objective of this work is to obtain catalysts for low-temperature water splitting to be employed in solar concentrators. Using a lower temperature allows to have more tolerant requirements for the structure and, possibly, to use heat sources other than sun for the reaction.[33,34]

With this objective, the work will be structured in the following steps: the starting materials of choice have been two perovskite oxides, namely $La_{0.8}Al_{0.2}NiO_3$ and $La_{0.8}Sr_{0.2}CoO_3$,[23,24] mentioned in section 1.2, chosen because of their low reduction temperature (800 °C and 1000 °C respectively). Then, the substitution (at least partial) of cobalt and nickel has been pursued, with candidate ions known for their catalytic activity for these reactions and compatible in size. In particular, iron and manganese have been chosen, since the synthetic route of lanthanum perovskites with these B-site cations is known and they are known to be active in similar reduction reaction (both of H_2O and CO_2).[35–39] Besides, the ionic radii ($r_{Mn} = 0.72\,\text{nm}$, $r_{Fe} = 0.69\,\text{nm}$) are compatible both with Ni ($r_{Ni} = 0.70\,\text{nm}$) and Co ($r_{Co} = 0.685\,\text{nm}$) while in hexacoordination,[30] and the precursors happen to be much less toxic than those of nickel and cobal.[40]

While considering the composition of the first literature perovskite, $La_{0.8}Al_{0.2}NiO_3$, some doubts on the effective stability emerge. The A-site doping with aluminium is incoherent with the size of the ions, since $r_{La} = 1.50\,\text{nm}$ and $r_{Al} = 0.675\,\text{nm}$ (less than 50% of r_{La}). A B-site doping would be more reasonable, as $r_{Ni} = 0.70\,\text{nm}$. Besides, the reported Al radium is measured for the hexacoordinated +3 ion, while lanthanum is dodeca-coordinated (as the typical A-site ion), and there is no value for aluminium in a similar coordination. The same coordination is observed for nickel and is typical of B-site ions.

In their work, Pérez et al.[23] cited a previous work by Wang et al.[41] in which the effect of A-site Al doping in $SrTiO_3$ is investigated through means of first-principle calculations, to support the hypothesis of Al going in the A-site. Nevertheless, typical aluminium doping in similar perovskites have always been observed to have an effect in the B-site of the perovskite, for various perovskites such as $La_{1-x}A_xMn_{1-y}Al_yO_3$,[31,37,42]

and $SrFe_{1-x}Al_xO_3$.[43]

For this reason, the possibility that the actual composition is $LaAl_{0.2}Ni_{0.8}O_3$ has been taken into account and will be discussed in section 3.1 while illustrating the results of the various syntheses.

1.5 Aim of the thesis

In the following work, the previously mentioned perovskite oxides will be synthesized, analysed and evaluated as possible catalysts for thermochemical water splitting below 1000 °C. The synthetic route will be balanced between obtaining good and pure materials and employing simple precursors, that allow a scalable synthesis with low environmental impact, following the green chemistry principles.[44]

The synthesized materials will be analysed by means of XRD and SEM to sample the crystal structure and morphology, EDX and XPS to analyse composition (the latter exploited also for oxidation states analysis), N_2 adsorption for surface area measurements. Details of the employed instruments are specified in section 2.3.

The catalytic activity will be measured through TPR (Temperature Programmed Reduction) first, in H_2 flow, and through TPD-TPO (Temperature Programmed Desorption - Oxidation) cycles. In the second case, the material is heated in a helium flow up to 1000 °C, re-oxidised in 5% O_2-He flow, then thermally reduced again.

Chapter 2

Experimental

In this chapter, the experimental approach followed in the research activity will be discussed. After a concise list of the chemicals used during the syntheses, the synthetic routes and the characterisation methods will be explained in detail.

2.1 Chemicals

Metal precursors:

- Al: $Al(NO_3)_3 \cdot 9\,H_2O$, $\geq$ 98.5%, Emsure
- Co: $Co(C_5H_7O_2)_3$, 97%, Aldrich
- Fe: Fe, 99.98%, Aldrich
- La: La_2O_3, $\geq$ 99.9%, Aldrich
- Mn: $(CH_3COO)_2Mn \cdot 4\,H_2O$, $\geq$ 99%, Aldrich
- Ni: $Ni(NO_3)_2 \cdot 6\,H_2O$, $\geq$ 97.0%, Aldrich
- Sr: $Sr(NO_3)_2$, $\geq$ 98%, Sigma-Aldrich

Complexing agents and others:

- Ammonia, 32%, Supelco
- Citric acid monohydrate, $\geq$ 99.0%, Aldrich
- Ethylene glycol, $\geq$ 99.0%, Emplura
- Nitric acid, $\geq$ 65%, Sigma-Aldrich

2.2 Synthesis

Based upon the previous considerations in section 1.3 and 1.4, the investigation will start from "$La_{0.8}Al_{0.2}NiO_3$"/$LaAl_{0.2}Ni_{0.8}O_3$ (referred to as LAN) and $La_{0.8}Sr_{0.2}CoO_3$ (LSC), assessing their activity to test the reproducibility. The first perovskite has proven to be very difficult to obtain with good purity, and a segregation of NiO and other perovskite phases is always observed. For this reason a partial substitution of the B-site cation has been operated only on LSC: first with 10% of nickel, to determine the contribution of an element known to work well for this reaction, in particular in ferrites,[18,45–47] and then with 25% and 50% of iron and manganese, to test the dependence of the activity on the percentage of doping. On top of that, the two 25% compositions have been also synthesized with a different A-site dopant content (La:Sr=6:4), to measure how much the A-site ratio affects oxygen release.

In the following table, all the compositions are clarified.

Table 2.1: Target materials and their abbreviations.

Composition	Abbreviation
$LaAl_{0.2}Ni_{0.8}O_3$	LAN
$La_{0.8}Sr_{0.2}CoO_3$	LSC
$La_{0.8}Sr_{0.2}Co_{0.9}Ni_{0.1}O_3$	LSCN10
$La_{0.8}Sr_{0.2}Co_{0.5}Fe_{0.5}O_3$	LSCF50
$La_{0.8}Sr_{0.2}Co_{0.75}Fe_{0.25}O_3$	LSCF25
$La_{0.6}Sr_{0.4}Co_{0.75}Fe_{0.25}O_3$	LS40CF
$La_{0.8}Sr_{0.2}Co_{0.5}Mn_{0.5}O_3$	LSCM50
$La_{0.8}Sr_{0.2}Co_{0.75}Mn_{0.25}O_3$	LSCM25
$La_{0.6}Sr_{0.4}Co_{0.75}Mn_{0.25}O_3$	LS40CM

The synthesis of the target materials follows a simple *self-combustion synthesis* route, which is cost- and time-effective on laboratory scale, besides usually yielding pure products in the desired phase and morphology. Each synthesis was set to give 2 grams of product; final yields ranged between 81.8% and 96.4%. In particular, two main methods have been followed, which are illustrated in the following paragraphs.

2.2.1 Marcilly method

Described by Christian Marcilly in 1970,[48] Marcilly method uses citrate as chelating agent. Nitrates of the desired metals (or other salts, oxides or even the metallic element, to which a stoichiometric amount of HNO_3 is added) are dissolved in water, together with

an excess of citric acid, which acts as chelating agent for a better dispersion of the cations, and HNO_3, which will serve as oxidizing agent in the combustion (the total amount of 65% nitric acid follows the ratio 9 mL:1 g for each gram of desired product). The solution is heated at 70 °C for two hours, after which NH_3 is added until the pH reaches a value of 7. Then, the solution is heated even further (90-100 °C, hotplate at 140 °C) and allowed to evaporate until the resulting material is dry (usually, 24 h).

The obtained product is then heated at over 350 °C, temperature at which the auto-combustion process begins. The citrate, which acts as complexing agent for the metal ions and thus mixes them randomly, reacts with the nitrate giving an amorphous network in which metals, oxygen and the leftover organic part are intimately mixed. This is then ground and calcined in an oven to remove the remaining carbon and to re-crystallise the mixed oxide in the single, desired perovskite phase. All the materials were heated with a ramp of 10 °C/min and then kept at 800 °C (for LAN) or 1000 °C (for all the other perovskites) for 6 h. The cooling ramp used the same rate.

A citrate:metal rate of 1.9 has been used in the synthesis of $La_{0.8}Sr_{0.2}CoO_3$, $La_xSr_{1-x}Co_{1-y}Mn_yO_3$ and $La_xSr_{1-x}Co_{1-y}Fe_yO_3$, known to work well in the synthesis of $LaCoO_3$-based perovskites.[49,50]

2.2.2 Pechini method

Maggio Pechini patented a similar method in 1967,[51] using citrate and ethylene glycol as complexing agents. The procedure is similar to Marcilly route, but ethylene glycol (EG:M=6:1) is added before heating at 70 °C for 2h.

This method proved to be suitable for oxides more susceptible to segregation, such as those containing nickel, that has the tendency to segregate as NiO. For this reason, it has been applied for the synthesis of $La_{0.8}Al_{0.2}NiO_3$ and $La_{0.8}Sr_{0.2}Co_{0.9}Ni_{0.1}O_3$. The citrate to metal ratio, which is 1.5, was chosen following Pérez et al.[23] for LAN synthesis and applied to LSCN10 because of the presence of nickel.

Calcination conditions are the same as the previously mentioned ones.

2.3 Characterization

Powder X-Ray Diffraction (XRD) analysis was performed in order to identify the phases that are contained in the product. A Bruker D8 Advance diffractometer in Bragg–Brentano geometry was employed, with a Cu Kα source (λ=0.154 nm). The patterns were acquired in the range of 2θ=20-80°, with steps of 0.02° and dwell time of

0.35 s/step.

Scanning Electron Microscopy (SEM) images were acquired with a Zeiss SUPRA 40VP microscope at 5 kV. For quantification of elements, SEM was coupled with Energy-Dispersive X-ray analysis (EDX) at 20 kV. In the following chapter, images at magnification of 5000x and 25000x will be shown. Images at 15000x magnification can be found in Appendix A.1.

N2 adsorption isotherms were collected at −196 °C with a Micromeritics ASAP2020 Plus instrument, in the relative pressure range (p/p0) of 0.01–1.00, and vice versa; prior to experiments, the samples (0.5 g to 1.0 g) were outgassed in a vacuum (p<1.3 Pa) at 300 °C for 3 h. Specific surface areas (SSA) were determined according to the Brunauer — Emmett — Teller (BET) model.[52]

X-ray Photoelectron Spectroscopy (XPS) was performed with a Thermo Scientific ESCALAB QXi spectrometer, employing a monochromatized Al Kα source (hν=1486.68 eV) and a charge compensation gun. Survey spectra were acquired at 100 eV pass energy, 0.5 eV/step and 25 ms/step dwell time. Elemental quantification was carried by the integration of the photopeaks, after Shirley-type background subtraction.

2.3.1 Crystallite size

The broadening of reflections observed in a diffraction pattern can be related to the size of the smallest coherently-diffracting domains, so-called crystallites.[53] Crystallite size can vary from few nanometres to several micrometres, and their size depends on the prevalence of nucleation over growth (small crystallites) or vice-versa.

Depending also from the shape factor $\mathcal{K}$ and the X-ray wavelength λ, from the reflection position θ and the FWHM (Full Width at Half Maximum) β the crystallite average diameter τ can be calculated through the Scherrer equation:[54]

$$\tau = \frac{\mathcal{K}\lambda}{\beta \cos\theta}$$

2.4 Activity assessment

Temperature Programmed Reduction (TPR), Desorption (TPD) and Oxidation (TPO) measurements were performed with a Micromeritics Autochem II 2920 instrument, with TC detector at 175 °C.

2.4.1 TPR

50 mg of the obtained product were placed in a U-shaped quartz reactor over some quartz wool to keep it in place. After 15 minutes of purging in 50 sccm 5% H_2/Ar at room temperature, the same gas flow was kept while heating at 10°C/min up to 900 °C. The TCD reading was used to measure the consumed H_2 that reacted with the oxide to give H_2O, conveniently condensed in a cold trap kept at about −80 °C. The consumed hydrogen is quantified through a previously conducted calibration.

2.4.2 TPD—TPO

For evaluation of oxygen exchange properties, 200 mg of sample were placed in the aforementioned reactor. After proper purging, 50 sccm of He were flowed in the reactor under a temperature ramp of 10 °C/min up to 600 °C and then of 5 °C/min up to 1000 °C measuring the thermal conductivity with the "clean" flow as reference. This, coupled with an appropriate calibration, allowed to quantify the released oxygen.

At high temperatures, some of the materials release oxygen as a continuous flow and not in peaks like some others (for instance, LSC), so it was difficult to discern the baseline drift and the oxygen contribution. For this reason, at every hundred degrees starting at 600 °C (the oxygen release at lower temperature is usually negligible) the ramp was suspended and the reactor was excluded from the gas flow, to have a reference measurements of the He flow without O_2 contribution.

On top of that, four measurements of an empty reactor with a were conducted, in order to subtract the contribution of the instrument itself (that is very sensible to slight changes of the experimental set-up). To quantify the apparent oxygen, a mass of 200 mg was set in the program, which is the mass of the samples used, allowing the subtraction of an equivalent contribution to the background.

After the first TPD cycle, an oxidation in 50 sccm 5% O_2/He for the whole cooling ramp (to 100 °C) with a 30 min break at 850 °C was performed, in order to restore the previously released oxygen. After that, a further heating cycle in helium was conducted to investigate the cyclability of the material.

2.4.3 Reproducibility

To have an insight on the reproducibility of the conducted measurements, the error was calculated on the measured backgrounds. The raw values are given in the table 2.2 with, as penultimate line, the average and relative error. $\frac{Average}{Error}$ ratio is reported in the

last line.

Table 2.2: Background values for each interval (in °C) for oxygen release, in mL/g.

Background	600-700	700-800	800-900	900-1000
B1	1.8907	2.0452	2.1012	3.4787
B2	1.7982	1.8073	1.9697	3.3156
B3	2.0987	2.0400	2.1104	3.1704
B4	1.8948	1.9418	2.1071	3.0866
Average±error	1.92 ± 0.13	1.96 ± 0.11	2.072 ± 0.068	3.26 ± 0.17
A/E	6.6%	5.7%	3.3%	5.3%

Chapter 3

Characterisations

3.1 LAN

3.1.1 Crystal structure

As discussed in section 1.4, this first material posed some issues in terms of synthesis of a pure phase. La-Al-Ni perovskite was chosen because of its low reduction temperature and high activity in the water splitting reaction. The literature composition $La_{0.8}Al_{0.2}NiO_3$ proved to be unrealistic for geometric constraints over the ion size. Therefore, it has been changed to $LaAl_{0.2}Ni_{0.8}O_3$. The most representative synthetic attempts are illustrated, in order to discuss both compositions and both synthetic routes.

Diffraction patterns of the first composition highlights the presence of many impurities, with a great amount of segregated NiO phase. This happens with samples synthesized both with Marcilly and Pechini method, as can be seen in figure 3.1. Moreover, a relevant amount of Ruddlesden-Popper perovskite $La_4Ni_3O_{10}$ can be observed, in particular from a series of close diffraction reflections at about $2\theta = 42°$.[55] The selection of this composition, $LaAl_{0.2}Ni_{0.8}O_3$, immediately leads to a great decrease of the free NiO phase even through Marcilly route, but it is only with Pechini method that a sufficiently pure sample is obtained.

The calculated Goldschmidt tolerance factor is 1.017, which predicts an hexagonal system:[29] this is in agreement with the observed diffraction pattern, that matches the one of hexagonal $LaAl_{0.1}Ni_{0.9}O_3$.

The crystallite size, calculated through Scherrer's equation, is fairly low. The table 3.1 sums up the results, that are all around 20 nm.

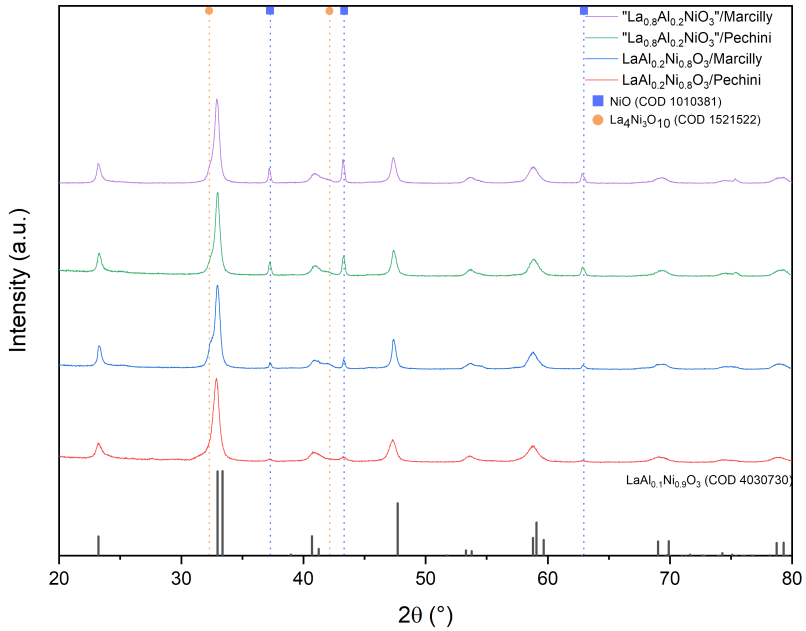

Figure 3.1: Diffraction pattern of the various La - Al - Ni perovskites.

Table 3.1: Crystallite size of LAN perovskites.

Sample	Crystallite size (nm)
"$La_{0.8}Al_{0.2}NiO_3$"/M	19.9
"$La_{0.8}Al_{0.2}NiO_3$"/P	23.4
$LaAl_{0.2}Ni_{0.8}O_3$/M	21.2
$LaAl_{0.2}Ni_{0.8}O_3$/P	18.0

Post-reaction

Only one of the synthesized samples was chosen for further characterisations and investigation of the activity. This happens to be the last illustrated one in the previous figure, which shows the lowest contamination of undesired phases. In figure 3.2, its diffraction pattern is compared to the pattern of the same sample after two catalytic cycles (a thermal reduction followed by an oxidation in 5% O_2/He and then another thermal reduction).

The sample composition is preserved only partially. An increase of NiO and $La_4Ni_3O_{10}$ can be seen by the relative intensity of the reflections. New reflections at $2\theta = 23.9°$ and 31.2° suggest the formation of a new phase: the best hypothesis is the RP perovskite La_2NiO_4.[55]

This suggests that the cyclability of the material is hard to obtain, with the impurities

rising for every new cycle performed on it.

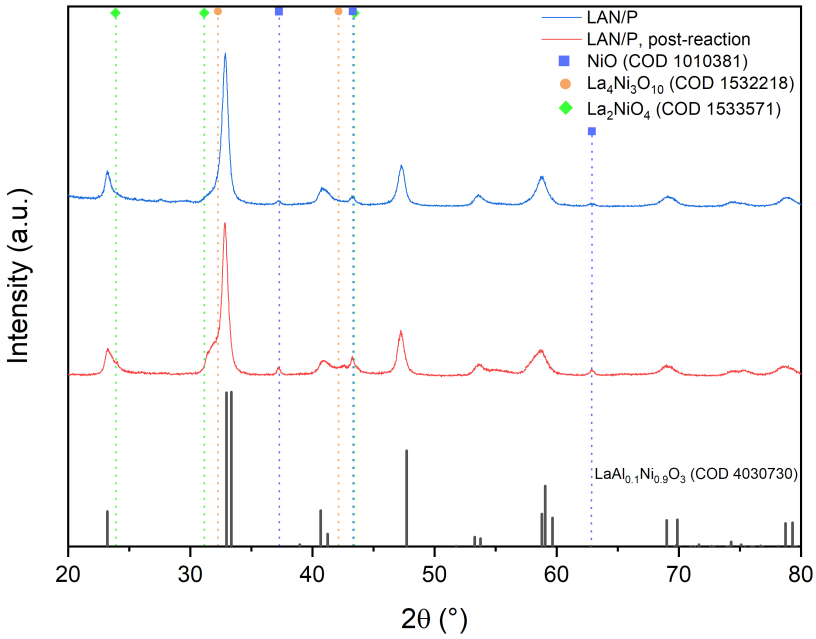

Figure 3.2: Diffraction pattern of the purest LAN perovskite, before and after the red-ox-red cycle.

3.1.2 Morphology

As can be seen in figures 3.3 and 3.4, the material shows a fine structure made of both bigger (about 10 µm) and smaller ($\leq$ 1 µm) scale-like particles. Overall, it has the appearance of a compact material.

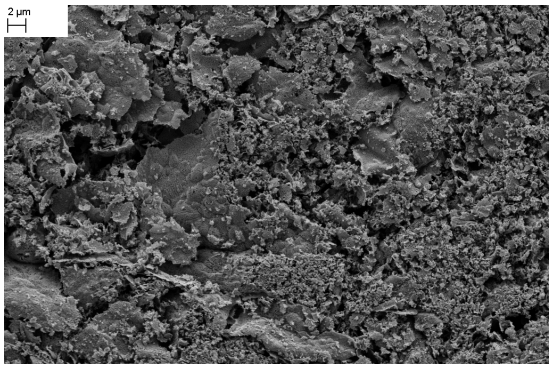

Figure 3.3: LAN — 5000x

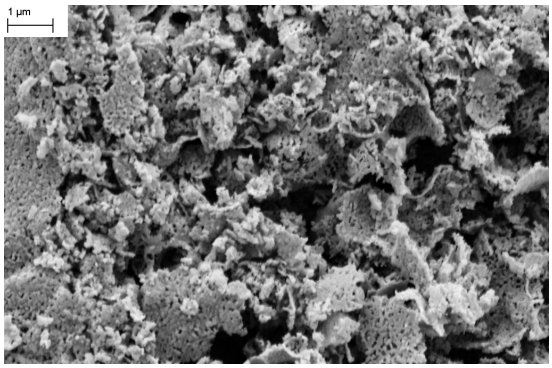

Figure 3.4: LAN — 25000x

Post-reaction

SEM images of the post-reaction material (figures 3.5 and 3.6) show some differences in the morphology, in particular some sintering between particles (although it might be due to different morphologies in the same material), but many of the observable features are maintained.

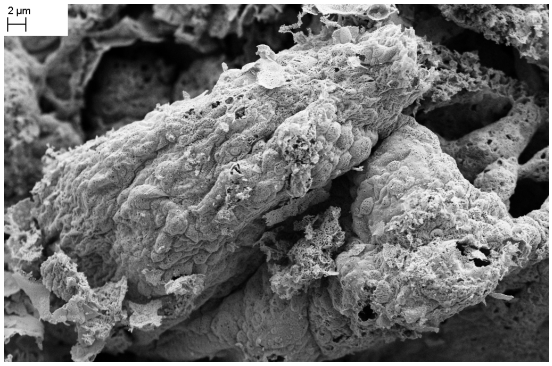

Figure 3.5: LAN post-reaction — 5000x

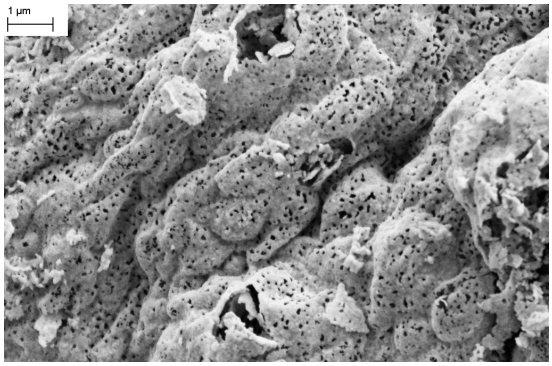

Figure 3.6: LAN post-reaction — 25000x

3.1.3 Composition

Table 3.2: EDX composition of LAN.

Element	Theoretical	Fresh	Post-reaction
La	1.00	0.97	1.14
Al	0.20	0.22	0.25
Ni	0.80	0.81	0.61

EDX measurements on the composition of the sample, as in table 3.2, show that the synthesis was successful in keeping the right proportion between the cations and that there is not any significant segregation in the first micrometres of the sample. It was not possible to obtain good results through XPS survey, since the main peaks of La, Al and Ni have a partial overlapping that makes it impossible to quantify the proportions of these elements.(source)

Post-reaction

After the two catalytic cycles, there is an increase of the La:Ni ratio measured by EDX. This can be explained by the segregation of a La-rich phase (La_2NiO_4), as seen in the diffraction pattern.

3.1.4 Surface area

The specific surface area (SSA), measured through N_2-physisorption (see chapter 2), is $9.86 \pm 0.14\,m^2/g$. This is coherent with literature values for $LaNiO_3$ synthesized with Pechini's method, that range between $6\,m^2/g$ and $12\,m^2/g$ depending on the calcination temperatures.[56]

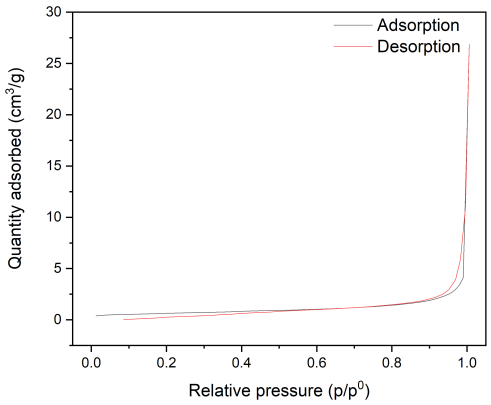

Figure 3.7: Isotherms of LAN in N_2.

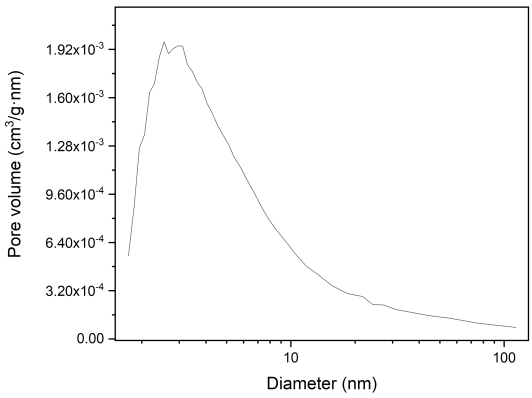

Figure 3.8: Pore size distribution of LAN.

Figure 3.7 depicts a typical adsorption isotherm of a perovskite as those investigated in the thesis activity. Isotherms of all the other materials are illustrated in the Appendice (figures A.18 to A.25) and they all confirm the mesoporosity of the materials.[52]

Pore size distribution curve is illustrated in figure 3.8. The most common pore size is 2.8 nm, with the majority ranging between 1.9 nm and 6.6 nm: the material is mesoporous, with some degree of microporosity.[57]

3.1.5 TPR

The TPR profile of this first material, as illustrated in picture 3.9, shows a series of peaks, corresponding to temperature ranges in which hydrogen is consumed while reacting with the material in a reduction reaction. The first two stages, close in temperature, have their maximums at 370 °C and at 425 °C respectively.

They match really closely those reported for pure $LaNiO_3$, that fall at 368 °C and 480 °C.[58] The second one falls about 55 °C lower than the literature peak: this could be a sign that the Al doping is indeed effective in allowing an easier reduction of the material.

The two processes that underlie these two peaks are the two steps of reduction of Ni^{3+} in the perovskite: the first peak is the $Ni^{3+} \longrightarrow Ni^{2+}$ step, followed by $Ni^{2+} \longrightarrow Ni^0$.[58] The total consumption of H_2 in these two processes, however, accounts for about a third

of the material (0.38 mol/mol of H_2 versus 0.8 mol/mol of Ni in LAN, in a reaction with stoichiometric ratio Ni^{3+}:H_2=2:3).

The remaining broad peak, with a maximum at about 700 °C but spreading between 590 °C and almost 900 °C, accounts for 0.25 mol/mol of H_2 more. It is unlikely to be attributed to Al, since both $LaAlO_3$ and Al_2O_3 do not react with hydrogen at temperatures below 900 °C.[59,60] This last peak probably still belongs to the series of Ni reductions, for a total of 0.63 mol/mol of H_2 consumed, which is about 53% of the amount of Ni in the sample (considering a 2:3 ratio of H_2:Ni for total reduction of $Ni^{3+} \longrightarrow Ni^0$). It has been observed previously that NiO or other nickel compounds can be stabilised if they are supported by other materials, such as alumina, giving a broad peak in the TPR profile at much higher temperatures than unsupported NiO, which usually falls between 200 °C and 250 °C.[61,62]

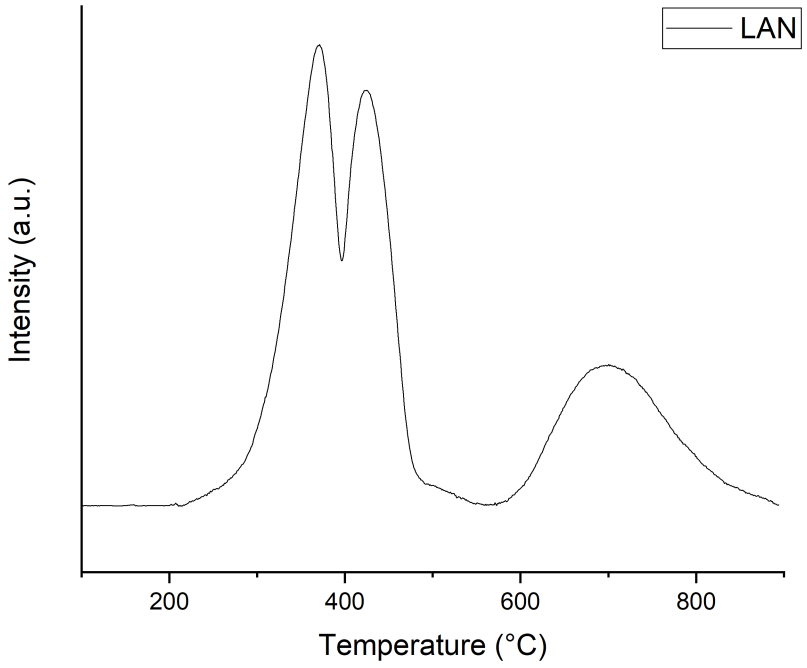

Figure 3.9: TPR profile of the LAN perovskite.

3.2 LSC — LSCN

3.2.1 Crystal structure

LSC material, with composition $La_{0.8}Sr_{0.2}CoO_3$, was reported in literature as very active in water splitting at low temperatures and for this reason it has been chosen as starting material to work with. The first operated substitution was a B-site doping with nickel, $La_{0.8}Sr_{0.2}Co_{0.9}Ni_{0.1}O_3$ (LSCN10).

The synthesis of LSC material proved to be straightforward, being it obtained through standard Marcilly route with high purity. LSCN10, on the other hand, needed Pechini route to avoid high segregation of NiO.

For both of them, the main byproducts was a Ruddlesden-Popper perovskite phase $La_{1+x}Sr_{1-x}MO_4$, with M being either Co or Ni in the case of LSCN10: this can be observed mainly through the highest reflection at $2\theta = 31.7°$, as in figure 3.10. $La_{1+x}Sr_{1-x}CoO_4$ and $La_{1+x}Sr_{1-x}NiO_4$ have very similar diffraction patterns, with many reflections overlapping: the few visible reflections are highlighted with ochre squares and are very low in intensity. For this reason, even the reflection at $2\theta = 31.7°$, due to a FWHM of $2\theta = 0.18°$, does not allow the discrimination between the Co and the Ni species. However, the increase in intensity in comparison to the undoped material of the 31.7° reflection, which is very subtle, might suggest that at least part of the Nickel is part of the crystal structure of the perovskite material.

As predicted by the Goldschmidt tolerance factor, which is higher than 1.01 for both perovskites, the system is hexagonal, matching in all reflections the selected reference (COD 1533518).[55]

The crystallite size, calculated through Scherrer's equation, is higher than the previous material, both of the two LSC oxides being above 40 nm (the precise values are in table 3.3).

Table 3.3: Crystallite size of LSC — LSCN10 perovskites.

Sample	Crystallite size (nm)
LSC	52.1
LSCN10	43.7

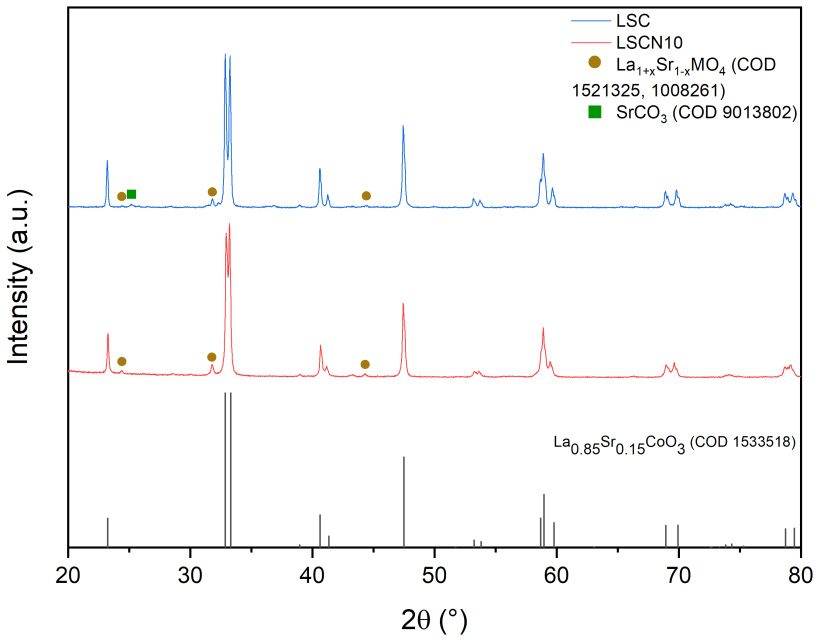

Figure 3.10: Diffraction pattern of the two LSC-based materials.

Post-reaction

The comparison between fresh and post-reaction LSC material is shown in figure 3.11. There is not any particular difference to notice, in agreement with the literature regarding the material,[24] confirming the high resistance to sintering and degradation during many catalytic cycles.

On the other hand, LSCN10 (which didn't have a great purity even when fresh — see figure 3.12 for comparison) shows a sharp increase in the secondary phases after just two cycles of reduction (the diffraction pattern is in Appendix A, figure 3.12). The increase of $La_{1+x}Sr_{1-x}MO_4$, with M being either Co or Ni, is relevant; moreover, a phase of cobalt oxide, highlighted with blue squares, appears.

This suggests that the material is unstable over a long number of cycles and therefore not suitable for catalytic applications, since the integrity of the original phase is compromised.

3.2.2 Morphology

Both the materials have scale-like morphology with particles ranging between more than 10 µm and about 2-3 µm. The scales show high macroporosity. Figures 3.13 to 3.16

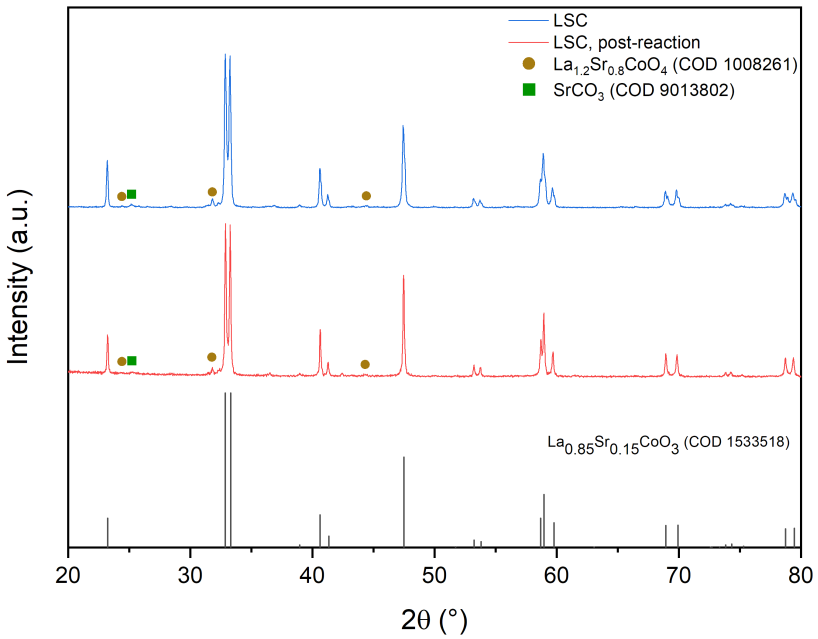

Figure 3.11: Comparison between LSC diffraction patterns before and after the red-ox-red cycle.

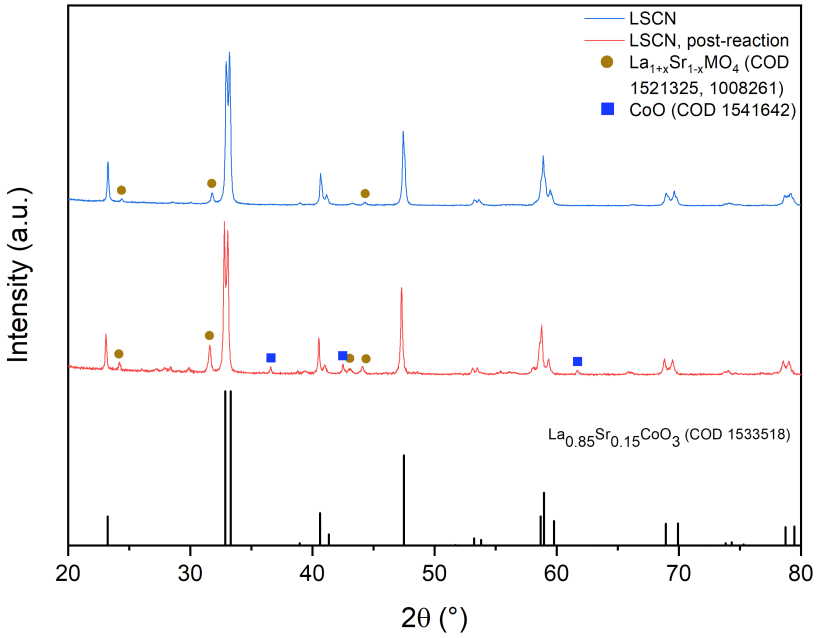

Figure 3.12: Comparison between LSCN10 diffraction patterns before and after the red-ox-red cycle.

show images of these two materials at 5000x and 25000x.

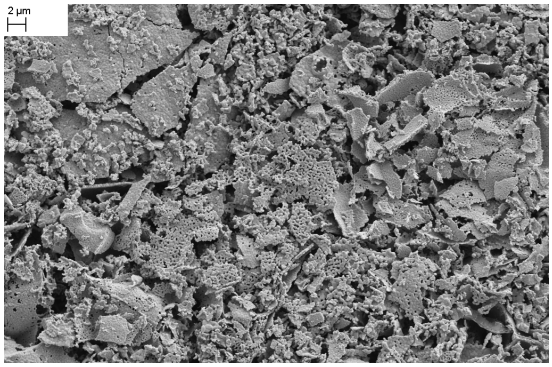

Figure 3.13: LSC — 5000x

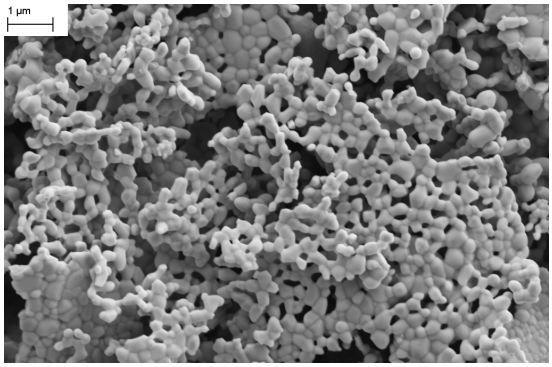

Figure 3.14: LSC — 25000x

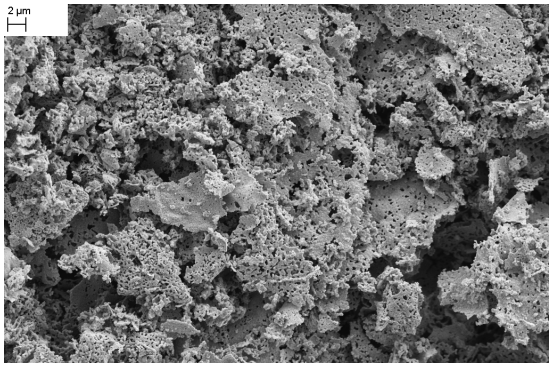

Figure 3.15: LSCN10 — 5000x

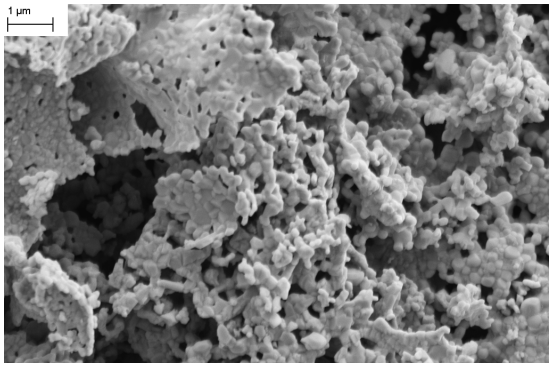

Figure 3.16: LSCN10 — 25000x

Post-reaction

After two catalytic cycles, the morphology (figures 3.17 to 3.21) does not show relevant differences. The reticulate structure of the scales is preserved.

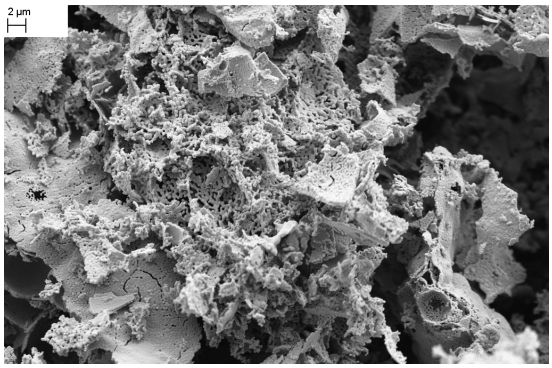

Figure 3.17: LSC post-reaction — 5000x

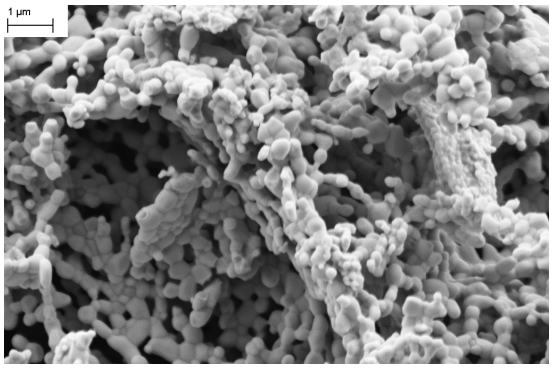

Figure 3.18: LSC post-reaction — 25000x

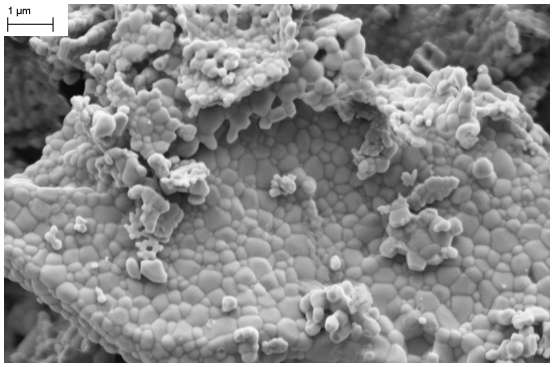

Figure 3.19: LSC post-reaction — 25000x

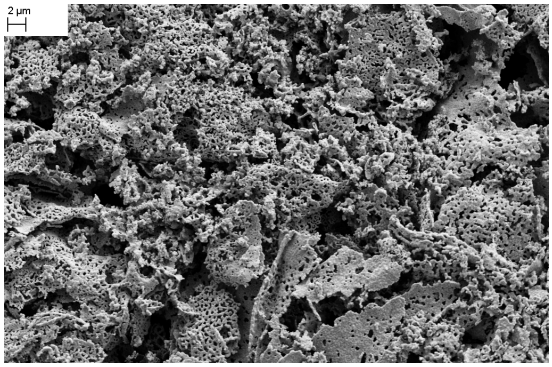

Figure 3.20: LSCN10 post-reaction — 5000x

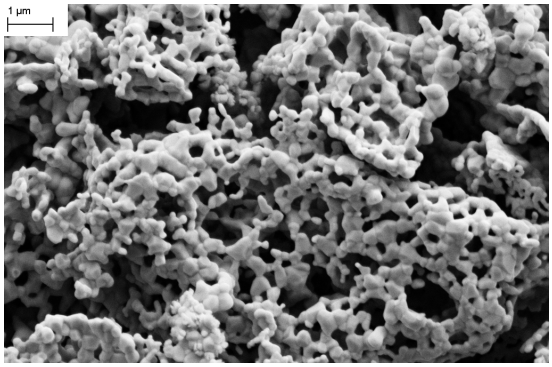

Figure 3.21: LSCN10 post-reaction — 25000x

3.2.3 Composition

Table 3.4: Composition of LSC.

Element	Theoretical	Fresh		Post-reaction	
		EDX	XPS	EDX	XPS
La	0.80	0.84	0.77	0.78	0.69
Sr	0.20	0.18	0.35	0.26	0.35
Co	1.00	0.98	0.89	0.96	0.96

The measured EDX composition, reported in tables 3.4 and 3.5, is almost coherent with the theoretical one in the case of LSC, with a 5% excess of Co and a 10% defect of Sr, while in LSCN10 the percentage of Sr is lower than expected of about 30% and Co in a 13% excess. This might be due to a segregation of a Co-rich and Sr-poor phase in the first layers.

In the case of LSC, the slight excess of La and defect of Sr in the EDX quantification can be explained by the XPS composition, which shows a great excess of Sr on the surface

Table 3.5: EDX composition of LSCN10.

Element	Theoretical	Fresh	Post-reaction
La	0.80	0.73	0.95
Sr	0.20	0.14	0.25
Co	0.90	1.02	0.69
Ni	0.10	0.12	0.11

(a phenomenon widely reported in literature)[63–66], due mainly to the exposure to high temperatures in oxidizing environment.[67] This superficial excess must be balanced by a Sr defect in the deeper layers, which are those investigated by EDX analyses (with a depth ranging from 30 nm to 1 µm), that actually show a La excess.

For LSCN10, the overlapping between Ni2p and La3d$\frac{3}{2}$ peaks makes it impossible to determine the exact composition by XPS measurements. Furthermore, since the percentage of Ni is just 10% in the B-site, the Ni3p peak at about 70 eV is too weak to be quantified.[68]

Post-reaction

In LSC, after the two catalytic cycles, there is not any relevant change to note: Sr remains in large excess, balanced by a defect in La; Co, on the other hand, moved towards the ideal value. This is a proof of the great stability of the material.

LSCN10, on the other hand, shows an increase in La and Sr percentages, with a decrease of Co: this might be due to the segregation of $La_{1+x}Sr_{1-x}MO_4$ phases, which are rich in A-site ions.

3.2.4 XPS: qualitative analysis

For LSC (and LSCF50 and LSCM50, as main representatives of LSCF and LSCM families respectively) a deeper XPS analysis has been conducted, focusing on the main peak for each element present in the perovskite. Peaks of La3d, O1s, Co2p, Sr3d, C1s before the reaction are compared to the same elements after two catalytic cycles.

La3d photopeaks (3.22) are characterized by a particularly interesting shape being composed by at least two contributions for each spin-orbit splitting peak. Focusing on the 3d$\frac{5}{2}$ signal, two main components can be observed at 834.9 eV and 838.0 eV. The component at higher binding energy (BE) is due to a shake-up phenomenon characteristic of La in oxidation state 3. The peak at lower BE is centred at 834.9 eV in the fresh sample and at 834.0 eV in the sample after reduction. The slightly different shape is compatible

with a less relevant presence of hydroxides/carbonates impurities after the treatment.[69]

In the O1s (3.23) signal two main peaks at 528.8 eV and 531.3 eV can be observed. These two peaks are attributed, respectively, to oxygen in lattice (as that in the perovskite) and in carbonates and hydroxides terminations, so confirming the suggestions gained by La 3d peak study.[69] The relative intensity of the two in the fresh material indicates that the amount of carbonates is high: this is typical for LSC perovskites.[69,70] The main reason for the increase of the higher BE component in the post-reaction material is the impurity due to SiO_2, with a main peak at 532 eV,[68] residual of the quartz wool used to realise the catalytic bed.

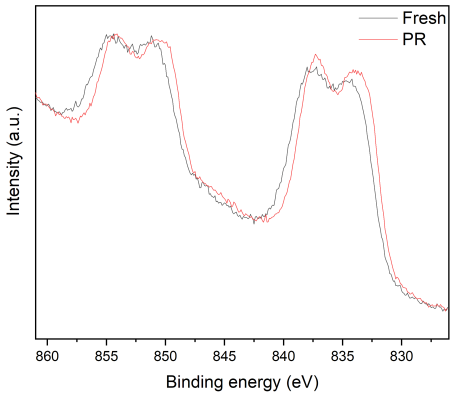

Figure 3.22: LSC - La3d.

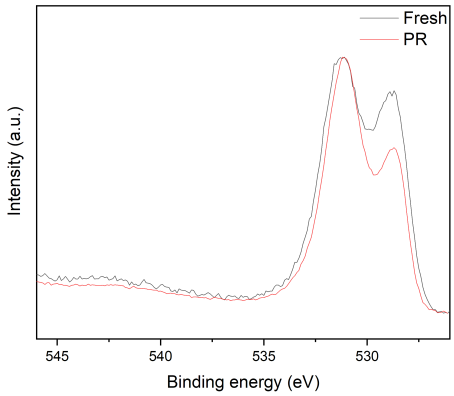

Figure 3.23: LSC - O1s.

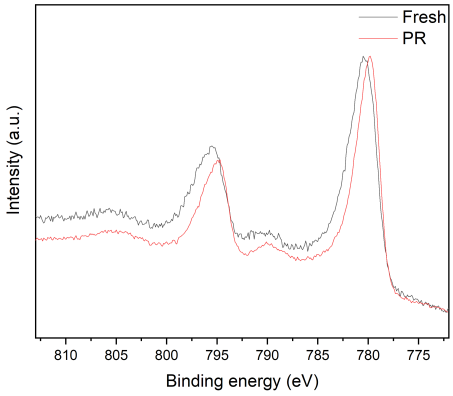

Figure 3.24: LSC - Co2p.

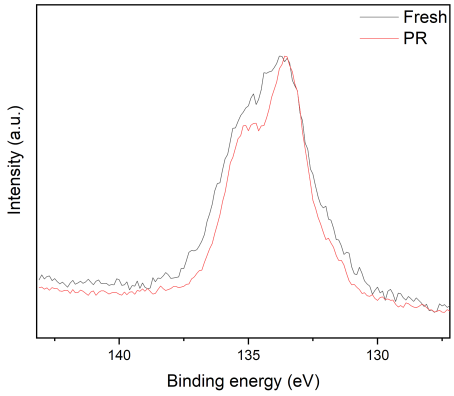

Figure 3.25: LSC - Sr3d.

Co2p (3.24) shows typical cobalt(III) features, with the first main peak (Co2p$\frac{3}{2}$) at about 780 eV. The absence of a satellite at 786 eV allows to exclude the presence of

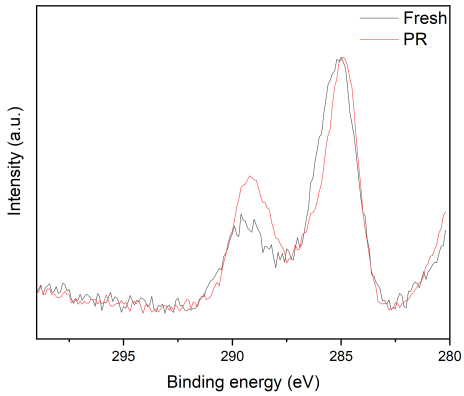

Figure 3.26: LSC - C1s.

Co^{2+}.[69] Also in this case the decrease of the Full Width at Half Maximum suggests a less heterogeneous situation after the reduction treatment.

Sr3d (3.25) shows two close peaks, due to the $3d\frac{3}{2}$ and $3d\frac{5}{2}$ contributions. The maximum falls at higher BE than what would be expected for strontium oxide (133.5 eV, compared to 132.9 eV): this is in agreement with a great amount of superficial carbonates, as reported in literature for LSC, observed even in the diffraction pattern.[69,70]

C1s (3.26) confirms the hypothesis about the presence of a large amount of carbonates. The most intense peak is due to adventitious carbon, at 284.8 eV, but the peak at higher binding energies (above 289 eV), typical of O−C=O, is much more intense than what could be expected for a pure perovskite.[69] The relative intensity of the peak at higher BE increases after the reaction: this might be indicative of a decrease in purity, although in disagreement with results for the other elements.

3.2.5 Surface area

Despite the different synthetic route, the two materials show a fairly similar specific surface area: $3.93 \pm 0.17\,m^2/g$ for LSC and $3.878 \pm 0.094\,m^2/g$ for LSCN10.

As a general rule, despite being usually well below $20\,m^2/g$,[13] the surface area of perovskite oxides is highly dependent on the synthetic conditions. In particular, sol-gel methods usually yield the highest areas, while co-precipitation methods rank the lowest.[71] It is possible to synthesize perovskites with high surface area ($> 25\,m^2/g$) with specific procedures, such as the use of templates, but these procedures are not easily compatible with the industrial up-scale so, in this thesis work, they have not been adopted.[72] Moreover, it deserves to be considered that the calcination temperature plays

the major role in determining the final product's specific surface area: it has been observed that calcination above 800 °C drastically diminishes those values, bringing them below 10 m^2/g.[72,73]

Pore size distributions, in figure 3.27, suggest that these two materials are mesoporous,[57] with maximums slightly above 3.0 nm and a range from 1.9 nm to 7.6 nm.

The surface area of LSC has been measured again after two catalytic cycles, with a result of $5.31 \pm 0.29\ m^2/g$. The reasons of this relevant increase (+35%) are still unclear, although it is evident that a re-arrangement of the fine morphology (no relevant change has been observed by means of electron microscopy) has taken place during the heating cycles. Pore size distribution (in figure 3.27) shows a trend which is similar to the fresh material, with a maximum for pores that are 3.2 nm in diameter and ranging from 1.8 nm to 8.2 nm.

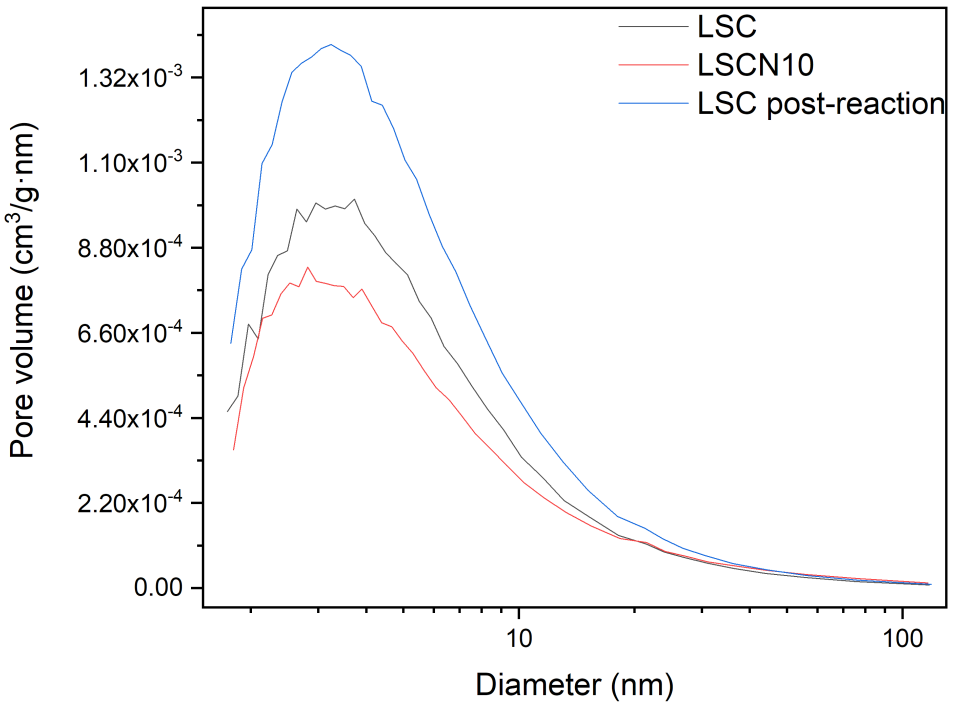

Figure 3.27: Pore size distribution of LSC materials.

3.2.6 TPR

The attribution of the observable peaks (see figure 3.28) for LSC and LSCN10 perovskites is a little bit less straightforward.

LSC shows two main peaks: one at 448 °C and one, more intense, at 660 °C. Both of them are quite broad, the first one ranging 320 °C to 510 °C, and the second one 560 °C to 750 °C. In particular, the first peak shows an evident shoulder at lower temperature: this is a smaller peak hidden by the bigger one, that accounts for the first step of the reduction. The first process is $Co^{4+} \longrightarrow Co^{3+}$, for the small portion of cobalt in +4 oxidation state (hence the lower height of the peak, below 400 °C). Then, at slightly higher temperature, the second step happens ($Co^{3+} \longrightarrow Co^{2+}$, between 400 °C and 500 °C), and finally $Co^{2+} \longrightarrow Co^{0}$, above 600 °C.[74,75]

Because of the overlapping between Co(IV) and Co(III) peaks, it is difficult to separate the contributions: the total consumption of H_2 for these two processes is 0.57 mmol/g, which is coherent with the amount of Co in the perovskite (1 mol/mol), considering the stoichiometric ration 2:1 between H_2 and Co in the reduction $Co^{3+} \longrightarrow Co^{2+}$ (and the slight excess for Co(IV)). The second peak, with stoichiometric ratio 1:1, amounts to 0.85 mol/mol, a reduction of 85% of the total Co in the perovskite. This could be a sign of the ready availability of the material to the reduction reaction.

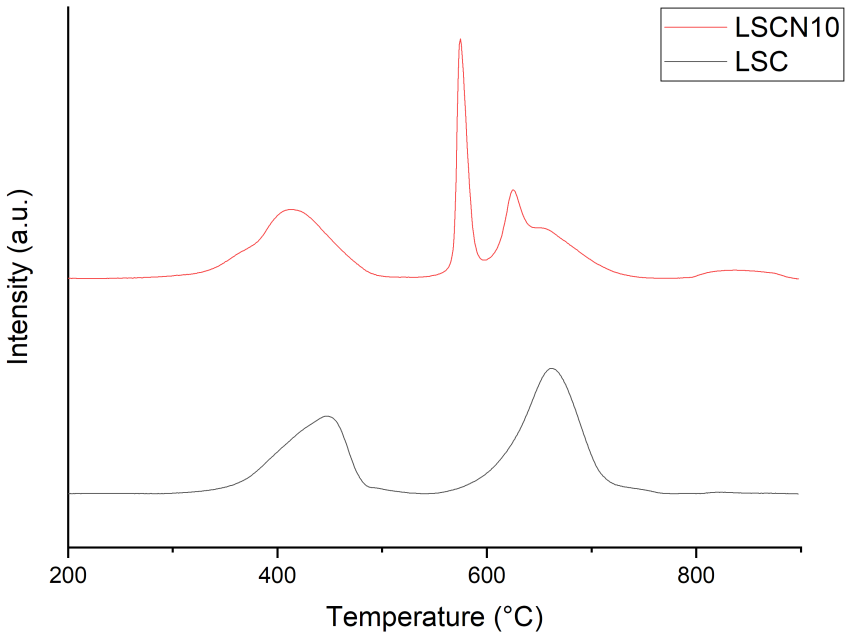

Figure 3.28: TPR profile of LSC and LSCN10 perovskites.

The TPR profile of LSCN10 is similar, with the addition of two sharp peaks at 575 °C and 625 °C. It is worth noting that the other two peaks are shifted at slightly lower temperatures: the first one is at 413 °C (ranging from 300 °C to 500 °C), the second and narrow one at 575 °C (from 550 °C to 600 °C), and finally the last one at 625 °C (ranging from 600 °C to 750 °C). Likely, this TPR profile is somewhat the combination of the previous one and the one for LAN (see figure 3.9): the first peak is due to the reduction of Co^{4+} and Co^{2+}, the second one to $Ni^{3+} \longrightarrow Ni^{2+}$ and the last one is the overlapping (as can be seen from the narrow central peak with an evident shoulder at 650 °C) of $Ni^{2+} \longrightarrow Ni^{0}$ and $Co^{2+} \longrightarrow Co^{0}$. The two nickel peaks fall at temperatures much higher than those observed for LAN (370 °C and 425 °C, as in section 3.1): this might be explained by a stabilisation of the nickel ions due to the different chemical environment they are in, similarly to what had happened for the peak at 700 °C of LAN. In table 3.6, hydrogen consumption values are summarised.

Table 3.6: Hydrogen consumption of LSC materials in the two main steps of reduction.

Sample	Metal (mol/mol)	T (°C)	H_2 (mol/mol)
LSC	1 (Co)	300-500	0.57
		550-750	0.85
LSCN10	0.9 (Co)	300-500	0.51
	0.1 (Ni)	550-600	0.24
	0.8 (Co), 0.1 (Ni)	600-750	0.28

The hydrogen consumption in the first step, about 0.57 mol/mol, is compatible with the reduction of all the Co(III) in the sample (0.9 mol/mol), taking into account the extra shoulder due to the small amount of Co(IV). However, the first sharp peak ($Ni^{3+} \longrightarrow Ni^{2+}$) corresponds to an hydrogen consumption of 0.24 mol/mol, much higher than those expected for the 0.1 mol/mol of Ni present in the material. Likely, this is due to the overlapping between the Ni and Co peaks, that makes difficult a correct evaluation of the contribution of the two elements. Moreover, the last peak (which should account for the reductions of both nickel and cobalt to metal, in stoichiometric ratio 1:1 with hydrogen) shows a very modest hydrogen consumption (0.28 mol/mol), showing that not all the material is available for the reaction.

3.3 LSCF

3.3.1 Crystal structure

The first series of doped La-Sr-Co perovskites has Fe in the B-site. All the materials has been obtained with good purity through a Marcilly route. The exact compositions for each abbreviation is explained in table 3.7.

Table 3.7: LSCF materials.

Composition	Abbreviation
$La_{0.8}Sr_{0.2}Co_{0.5}Fe_{0.5}O_3$	LSCF50
$La_{0.8}Sr_{0.2}Co_{0.75}Fe_{0.25}O_3$	LSCF25
$La_{0.6}Sr_{0.4}Co_{0.75}Fe_{0.25}O_3$	LS40CF

It is not possible to compare the diffraction pattern to any pattern in the database, since there is not any registered material with similar composition. The closest match is $SrCo_{0.4}Fe_{0.6}O_3$ (COD 1528296)[55] and it has been used as reference in figure 3.29. Two of the reflections observed for the synthesized material (2θ = 23.0° and 52.9°) are almost absent in the reference pattern: this appears to be typical of perovskites with Sr in A-site position, if compared with La-perovskites. This hypothesis is confirmed by the comparisons between $LaCoO_3$ and $SrCoO_3$ and between $LaFeO_3$ and $SrFeO_3$, as both the Sr perovskites lack the intense reflections in the mentioned regions.[55] For this reason, it is clear that the presence of two intense reflections in the experimental pattern which cannot be seen in the reference is due to the different A-site composition.

The main impurity, as highlighted in the figure, is a Ruddlesden-Popper phase, namely $LaSrCo_{0.5}Fe_{0.5}O_4$, that has the main visible reflection at $2\theta = 31.6°$.[55]

The effectiveness of the doping of $La_{0.8}Sr_{0.2}CoO_3$ with Fe can be extrapolated from the precise position of the reflections. In particular, in figure 3.30 the main peak (between 2θ = 32° and 34°) is compared to those of "pure" phases $LaFeO_3$ and $LaCoO_3$.[55] For reference, the reflection of $SrCo_{0.4}Fe_{0.6}O_3$ is shown. In this comparison, LSCF50 falls in the middle, as it could be expected from this composition, while both LSCF25 and LS40CF, with Co : Fe = 75 : 25, fall closer to $LaCoO_3$ and more or less in the same position between them.

All the Goldschmidt tolerance factors of these oxides (detailed in table 3.8) fall in the range between 1.015 and 1.025, then predicting a hexagonal system. Nonetheless, the observed patterns agree with a cubic system, as the position and the splitting of the reflections closely resemble those of the aforementioned $SrCo_{0.4}Fe_{0.6}O_3$, which is indeed

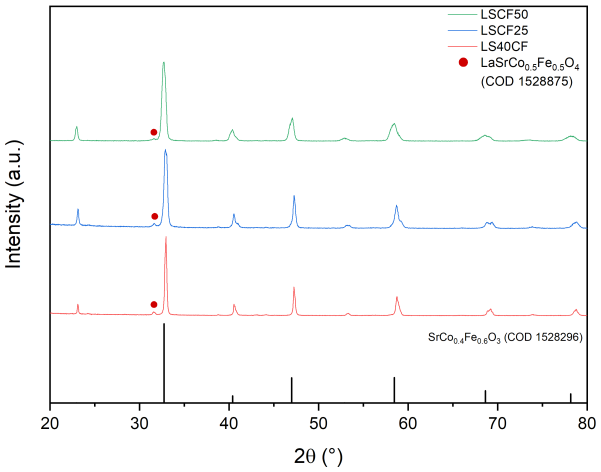

Figure 3.29: Diffraction pattern of the LSCF-based materials.

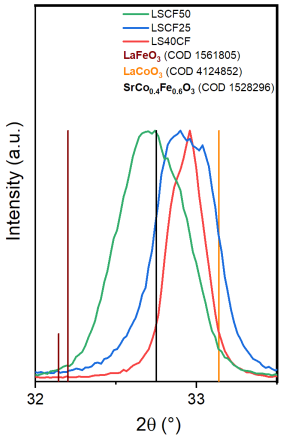

Figure 3.30: Detail.

cubic. This might be due to the value of Goldschmidt tolerance factor, which is really close to the threshold value of 1 between hexagonal and cubic systems.

Table 3.8: Goldschmidt tolerance factor of LSCF perovskites.

Sample	Tolerance factor
LSCF50	1.016
LSCF25	1.017
LS40CF	1.025

The crystallite size, calculated through Scherrer's equation, matches that of the previous materials, ranging from 20 nm to 40 nm. The exact results can be found in table 3.9. The trend of the size correlates with the percentage of Co in the oxide, with an increase of 61% from LSCF50 to LSCF25 and of 85% from LSCF50 to LS40CF (both LSCF25 and LS40CF have 75% Co in the B-site).

Table 3.9: Crystallite size of LSCF perovskites.

Sample	Crystallite size (nm)
LSCF50	21.6
LSCF25	34.8
LS40CF	40.0

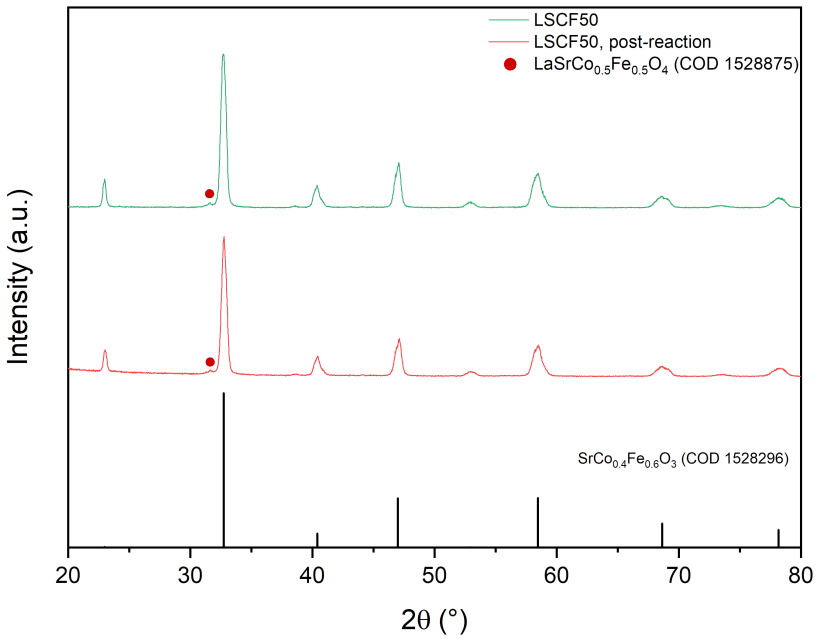

Figure 3.31: Comparison between LSCF50 diffraction patterns before and after the red-ox-red cycle.

Post-reaction

There is not any particular difference to be noted in the pattern after the treatment of the sample. The same impurity present in the original material can be observed again (mainly at $2\theta = 31.6°$) without increasing in quantity.

The pattern of post-reaction LSCF50, compared to fresh LSCF50, is shown in figure 3.31. Diffraction patterns of the two remaining samples can be found in figure 3.32.

3.3.2 Morphology

Figures 3.33 to 3.38 show SEM images at various magnifications. As for the previous materials, the scale-like morphology is confirmed with high macroporosity on the scales. Apparently, a higher Co percentage correlates with bigger particle size, but the porosity is lower.

Post-reaction

Images of reacted LSCF50 (3.39 and 3.40) do not indicate a relevant sintering in the material after two catalytic cycles. Similar images of LSCF25 and LS40CF can be found

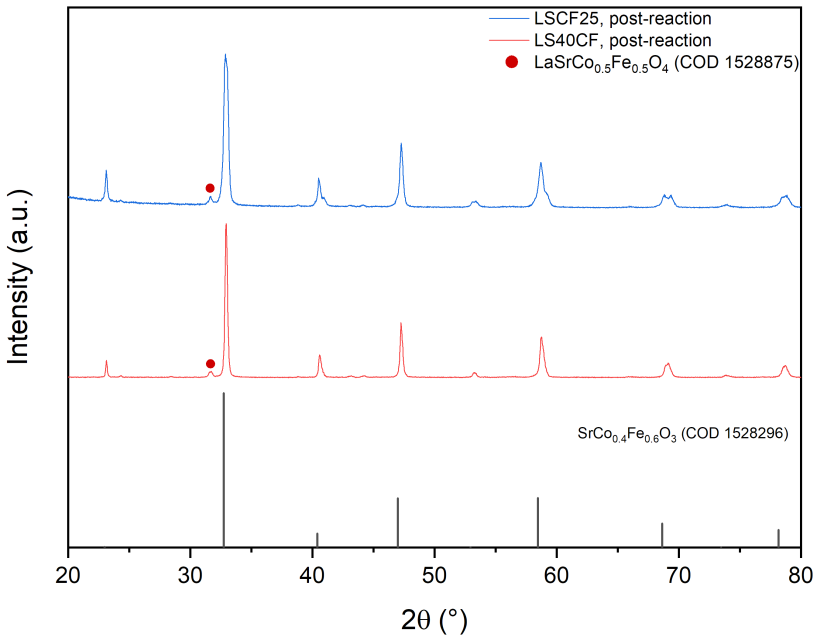

Figure 3.32: Diffraction patterns of LSCF25 and LS40CF after the red-ox-red cycle.

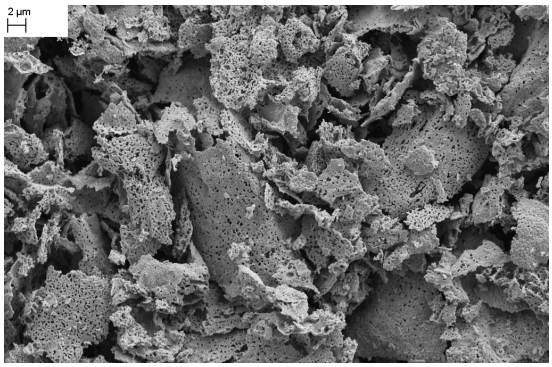

Figure 3.33: LSCF50 — 5000x

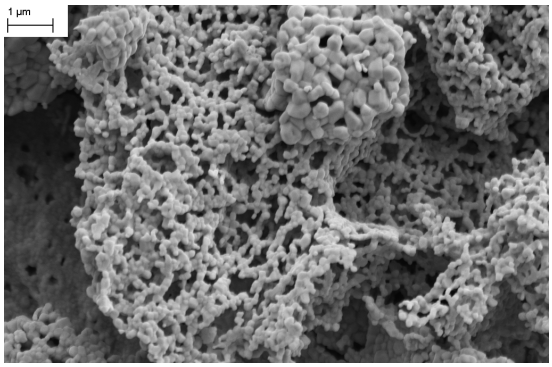

Figure 3.34: LSCF50 — 25000x

in the appendices (A.10 to A.13) and confirm this hypothesis.

3.3.3 Composition

The measured EDX composition matches quite closely the theoretical one. Nevertheless, while Co and Fe proportions are mainly maintained (both between them and in the material), La and Sr show a slight deviation from the theoretical value, with La being higher than expected and Sr being lower. Only in LS40CF this behaviour is more evident as can be read in table 3.12, with the "actual" ratio being much closer to 80:20 (instead

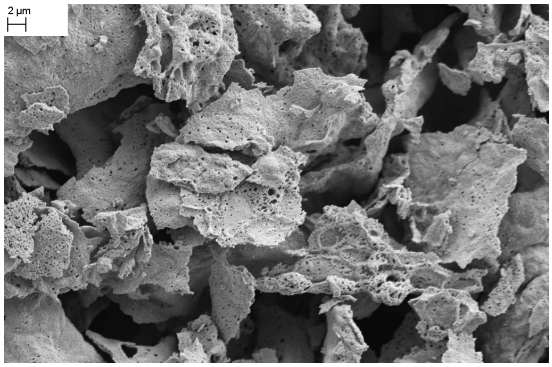

Figure 3.35: LSCF25 — 5000x

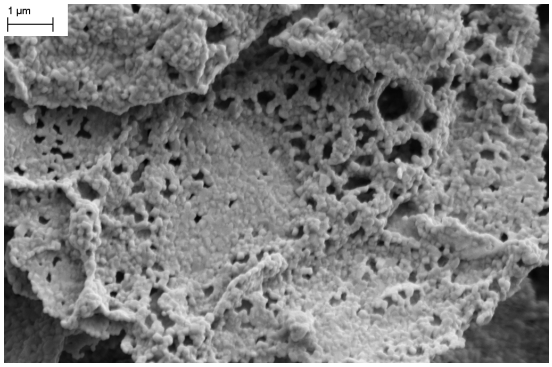

Figure 3.36: LSCF25 — 25000x

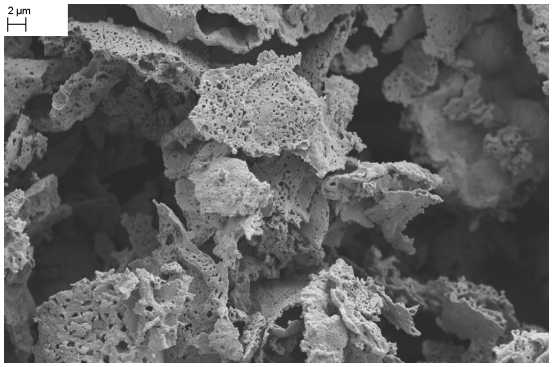

Figure 3.37: LS40CF — 5000x

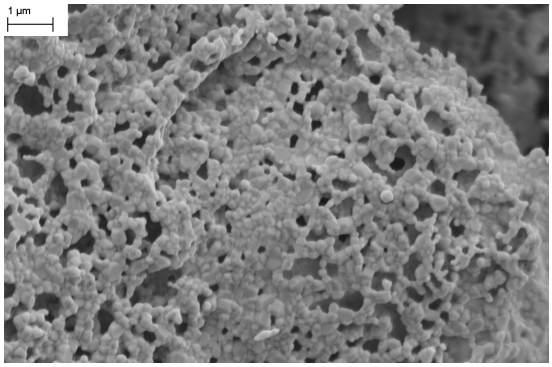

Figure 3.38: LS40CF — 25000x

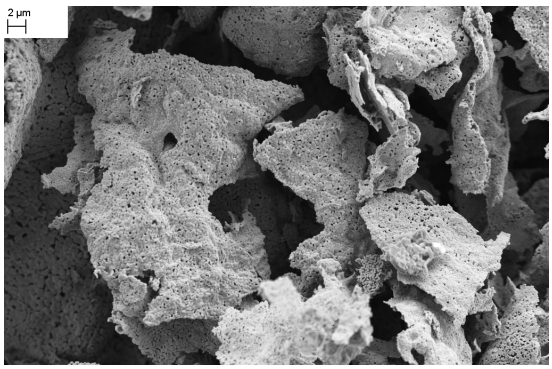

Figure 3.39: LSCF50 post-reaction — 5000x

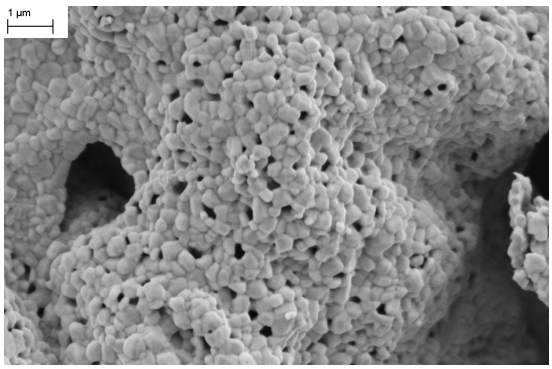

Figure 3.40: LSCF50 post-reaction — 25000x

of 60:40), similarly to LSCF25 and LSCF50.

XPS results are consistent with the surface segregation of A-site cations, in particular Sr results present in higher amount with respect to EDX composition. Fe and Co are present in different amount with respect to EDX: in particular, cobalt is more abundant than the nominal value in LSCF50 while iron is deficient. This is unusual because the tendency is toward Fe surface segregation in perovskites in which both these cations are present.

Table 3.10: Composition of LSCF50.

Element	Theoretical	Fresh		Post-reaction	
		EDX	XPS	EDX	XPS
La	0.80	0.87	0.89	0.89	0.70
Sr	0.20	0.18	0.25	0.16	0.56
Co	0.50	0.45	0.64	0.48	0.51
Fe	0.50	0.50	0.23	0.48	0.21

Table 3.11: Composition of LSCF25.

Element	Theoretical	Fresh		Post-reaction	
		EDX	XPS	EDX	XPS
La	0.80	0.88	0.75	0.88	0.86
Sr	0.20	0.17	0.21	0.15	0.23
Co	0.75	0.69	0.68	0.70	0.63
Fe	0.25	0.26	0.36	0.27	0.28

LSCF50 (table 3.10) shows the greatest divergence between EDX and XPS, with EDX measurements being in good agreement with theoretical values.

Post-reaction

For LSCF25 and LS40CF, as in tables 3.11 and 3.12, the composition doesn't change much in the two cycles, except for the great increase in superficial Sr in LS40CF.

On the other hand, similarly to what has previously been observed for LSCF50, Sr segregation after two cycles is very high (reaching 28% of the total metallic atoms on the surface), while there is a further decrease of the already low Fe percentage.

3.3.4 XPS: qualitative analysis

Fe2p can be seen in figure 3.41. The profile is typical for Fe^{3+} oxides, with the main peak at 710.8 eV. Fe^{2+}, that should have a contribution at 709 eV, can be excluded.[69] The coincidence between pre- and post-reaction curves indicates that iron ions near neighbours are not altered by the activity.

Comparing the O1s signals (3.42) recorded in the fresh materials, the analysis suggests that there are less superficial carbonates and hydroxides than in LSC. The increase in the peak at higher BE (531 eV) in the post-reaction material is due mainly to the addition of SiO_2, as previously explained.[69]

Table 3.12: Composition of LS40CF.

Element	Theoretical	Fresh		Post-reaction	
		EDX	XPS	EDX	XPS
La	0.60	0.74	0.67	0.72	0.55
Sr	0.40	0.20	0.32	0.23	0.55
Co	0.75	0.79	0.72	0.74	0.67
Fe	0.25	0.26	0.28	0.25	0.23

In the La3d spectrum (3.43), the usual splitting between $3d\frac{3}{2}$ and $3d\frac{5}{2}$ can be observed. The position is maintained before and after the reaction, with the first peak centred at 834.6 eV. The two close peaks, though, appear less distinguishable: this is due to the formation of oxyhydroxide species, that increase the FWHM.[68]

In Co2p (3.44), the comparison before pre- and post-reaction material does not show relevant changes in peak position. $2p\frac{3}{2}$ is centred at 780.6 eV in both samples and the absence of a satellite at 786 eV is indicative of the absence of Co(II).[69]

Sr3d (3.45) shows the first peak below 132 eV, but a second and more intense peak at 133.7 eV suggests that the amount of superficial carbonates is relevant. Furthermore, C1s (3.46), besides an intense peak at 284.8 eV which is due to adventitious carbon, shows another peak at 288.9 eV due to carbonates.[69]

An increase between the fresh and post-reaction material in terms of carbonates (both in Sr3d and in C1s) can be observed. This could be explained by a higher reactivity of the post-reaction superficial species which, despite being cooled in inert atmosphere, can then react with air at room temperature and absorb CO_2.

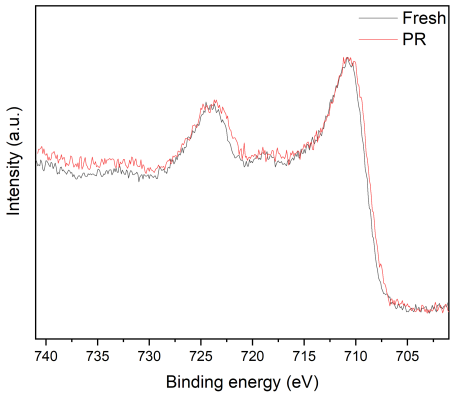

Figure 3.41: LSCF - Fe2p.

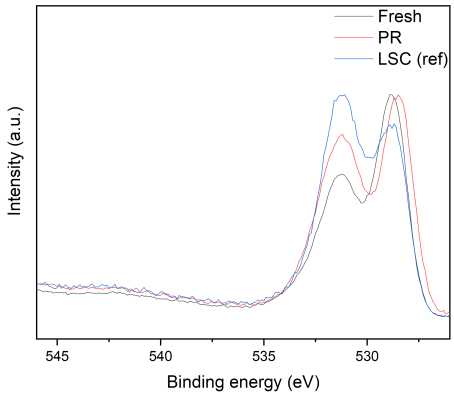

Figure 3.42: LSCF - O1s.

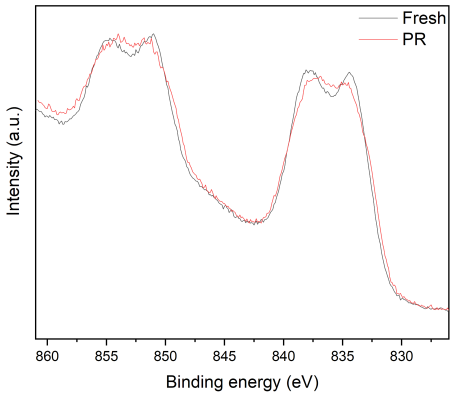

Figure 3.43: LSCF - La3d.

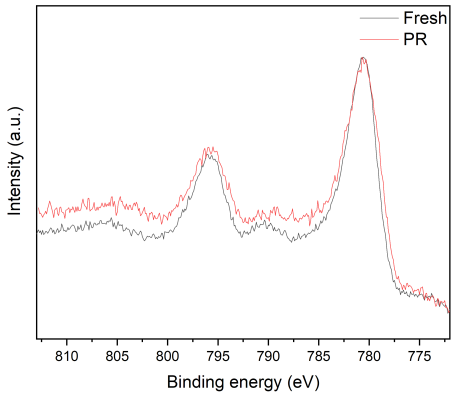

Figure 3.44: LSCF - Co2p.

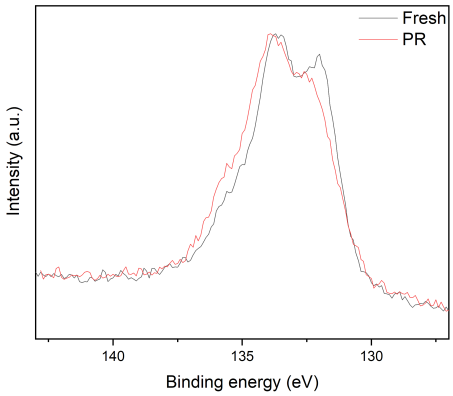

Figure 3.45: LSCF - Sr3d.

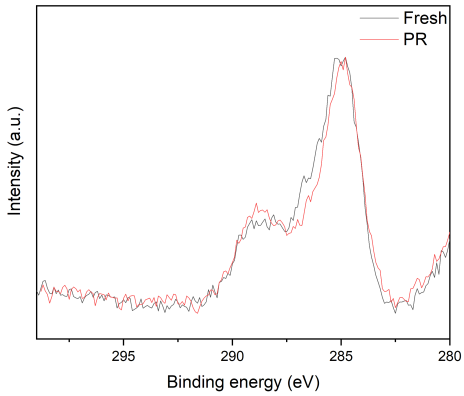

Figure 3.46: LSCF - C1s.

3.3.5 Surface area

Specific surface areas (SSAs) for this family, displayed in table 3.13, range from 1.5 m^2/g to 3.0 m^2/g. They are lower than LSC, while in literature $LaFeO_3$ is found to be usually characterised by SSA higher than $LaCoO_3$ in similar conditions.[72] A dependence on the cobalt content could be partially confirmed by the 18% decrease in SSA from LSCF50 to LSCF25 (with a higher Co content). A further decrease is obtained when increasing the strontium stoichiometry, with a -21% from LSCF25 to LS40CF.

Pore size distributions (PSD), in figure 3.47, show features that are very similar to those observed for LSC and LSCN10, with a maximum at 3.1 nm and the main range between 1.8 nm and 7.7 nm. The materials are mesoporous.[57]

Post-reaction LSCF50 has been analysed again, with a resulting area of 3.85 ± 0.24 m^2/g.

Table 3.13: BET surface areas of LSCF perovskites.

Sample	Specific surface area (m^2/g)
LSCF50	2.754 ± 0.091
LSCF25	2.255 ± 0.088
LS40CF	1.791 ± 0.065

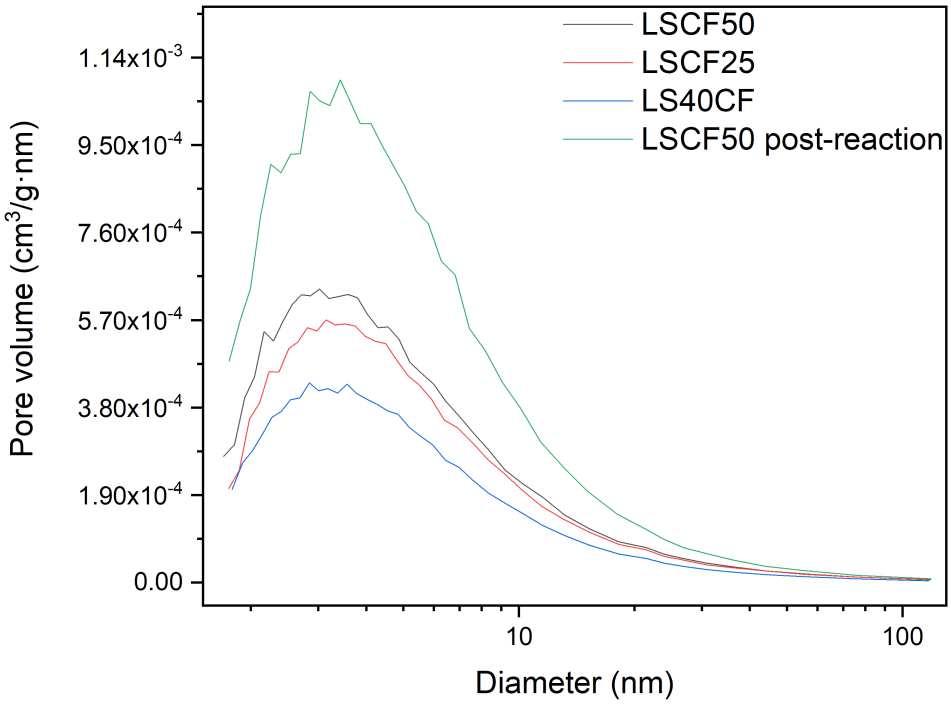

Figure 3.47: Pore size distribution of LSCF materials.

Again, an increase of about 40% is observed, for reasons yet to be elucidated. Pore size distribution, in figure 3.47, is similar to the fresh material, ranging from 1.8 nm to 8.2 nm, with a maximum at 3.2 nm, and also matches perfectly the one of post-reaction LSC (section 3.2).

3.3.6 TPR

The three samples of this family show some similarities despite the different composition, especially at low temperatures, but highly diverse features towards the end of the ramp.

As observed in figure 3.48, all of them have a first peak slightly above 400 °C, which accounts for the reduction of Co(IV) and Co(III) in the sample, according to the literature.[76–78]

This is supported also by the quantification of H_2 consumption: in LSCF50 this is about 0.30 mol/mol, compared to 0.5 mol/mol of Co in the sample (the reaction has 1:2 ratio for the reduction of $Co^{3+} \longrightarrow Co^{2+}$ and a part of Co is Co(IV)); in LSCF25 0.38 mol/mol compared to 0.75 mol/mol; finally, in LS40CF, 0.50 mol/mol compared to 0.75 mol/mol, which is much higher than 1:2 because of the greater amount of Co(IV) due to the higher percentage of Sr in the material.[79]

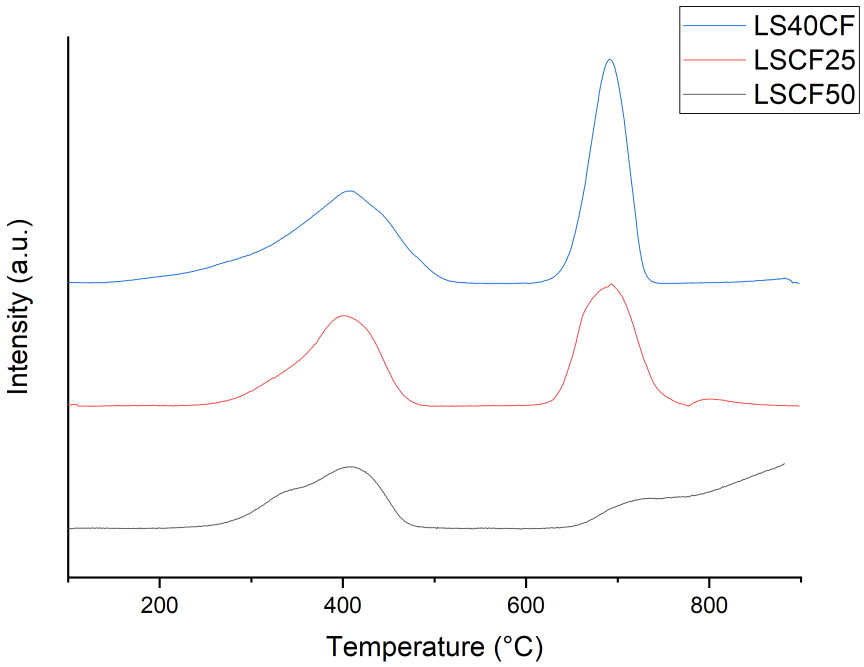

Figure 3.48: TPR profile of the three LSCF perovskites.

The behaviour at higher temperatures is more difficult to understand completely. LSCF50 shows an increase of the signal without defining a peak, with a monotonous growth until 900 °C (the end of the measurement). This is due to the high Fe content, with an observable shoulder at about 700 °C that can be attributed to Co: the position is typical for the element, as evident from the other two curves in the plot, but the peak is overlapping to a continuous growth. The H_2 consumption then comes both from $Co^{2+} \longrightarrow Co^0$ and $Fe^{3+} \longrightarrow Fe^0$ and it is difficult to separate the two contributions, even calculating the number of consumed mmol, since the peak is not complete.[77]

Both LSCF25 and LS40CF, on the other hand, show a well-defined peak with max-

imum at 690 °C. This is due to the already mentioned reduction of Co^{2+} to metallic Co.[77] However, the calculated hydrogen consumption (0.33 and 0.43 mol/mol, respectively) doesn't match the Co content of the perovskites, accounting for 40 to 60% of it. There might be some Co(II) ions that are less accessible or more stabilised and don't take part to the reduction process. However, it should be noted that the increased Sr content in LS40CF enhances the reducibility of the material, since the hydrogen consumption is higher. As previously discussed, the amount of Sr^{2+} has a direct effect on the presence of M^{4+} species, such as Co(IV) and Fe(IV), which has been found to be present in strontium perovskites.[80]

All the quantifications are displayed in table 3.14.

Table 3.14: Hydrogen consumption of LSCF materials in the two main steps of reduction.

Sample	Co (mol/mol)	Temperature range and center (°C)	H_2 (mol/mol)
LSCF50	0.5	300-500 (407) 650-900	0.30 0.32
LSCF25	0.75	300-500 (400) 650-750 (690)	0.38 0.33
LS40CF	0.75	300-500 (405) 650-750 (690)	0.50 0.43

3.4 LSCM

3.4.1 Crystal structure

This other series of La-Sr-Co perovskites was doped with Mn in the B-site. All the materials were synthesized by means of a Marcilly synthesis, which allowed to obtain good results in terms of purity. In table 3.15 the detailed compositions are illustrated.

Table 3.15: LSCM materials.

Composition	Abbreviation
$La_{0.8}Sr_{0.2}Co_{0.5}Mn_{0.5}O_3$	LSCM50
$La_{0.8}Sr_{0.2}Co_{0.75}Mn_{0.25}O_3$	LSCM25
$La_{0.6}Sr_{0.4}Co_{0.75}Mn_{0.25}O_3$	LS40CM

The resulting patterns are then compared to $La_{0.7}Sr_{0.3}MnO_3$ (COD 1533730) and $La_{0.85}Sr_{0.15}CoO_3$ (COD 1533518),[55] as in figure 3.49.

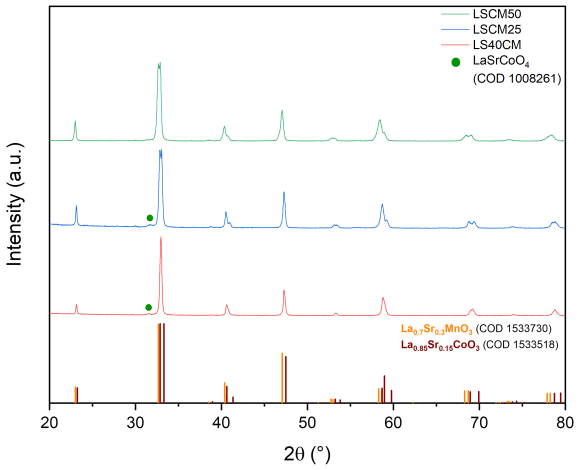

Figure 3.49: Diffraction pattern of the LSCM-based materials.

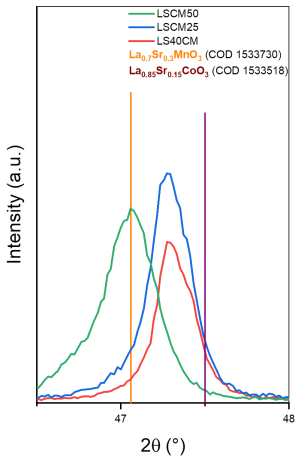

Figure 3.50: Detail.

The main impurity is a Ruddlesden-Popper phase, namely $LaSrCoO_4$, which is visible mainly in the two samples with 75% Co in a reflection at $2\theta = 31.8°$. Apart from that, all the reflections fall in between the two extremes given by the two B-site-pure references, thus suggesting the good distribution of the cobalt into the lattice.

In figure 3.30, a detail of the single reflection between 47° and 48° can be observed: as expected, LSCM50 falls closer to the Mn-pure reference, while LSCM25 and LS40CM have the maximum between the two. It is still unclear why LSCM50 matches many of

the reflections of $La_{0.7}Sr_{0.3}MnO_3$ despite having only 50% Mn in the B-site, although the absence of other phases in the sample (and the slightly different position of some less intense reflections, as those between 52° and 54°) suggests that the doping was indeed successful.

The splitting between the two reflections between 32° and 33° is in agreement with a hexagonal system, as predicted by the Goldschmidt tolerance factor, slightly above 1. Tolerance factors for each material are reported in table 3.16.

Table 3.16: Goldschmidt tolerance factor of LSCM perovskites.

Sample	Tolerance factor
LSCM50	1.008
LSCM25	1.013
LS40CM	1.018

Crystallite size is in line with the previous results, between 25 nm and 40 nm. The trend, visible in the table 3.9, suggests again (as in section 3.3) that a higher percentage of Co correlates with higher crystallite size.

Table 3.17: Crystallite size of LSCM perovskites.

Sample	Crystallite size (nm)
LSCM50	27.6
LSCM25	39.0
LS40CM	36.0

Post-reaction

Similarly to what has been observed for LSCF (section 3.3), no relevant degradation is observed after two reduction cycles. There is just one new impurity, barely visible in figure 3.51, which could be attributed to the Ruddlesden-Popper phase not present in LSCM50 but present in LSCM25 and LS40CM, $LaSrCoO_4$ (see figure 3.49).

Diffraction patterns of the two remaining samples, with similar behaviour, can be found in figure 3.52.

3.4.2 Morphology

The three materials of this family, similarly to LSCF, present themselves in scales of about 10 µm in diameter. A similar trend in size and porosity is observed: materials richer

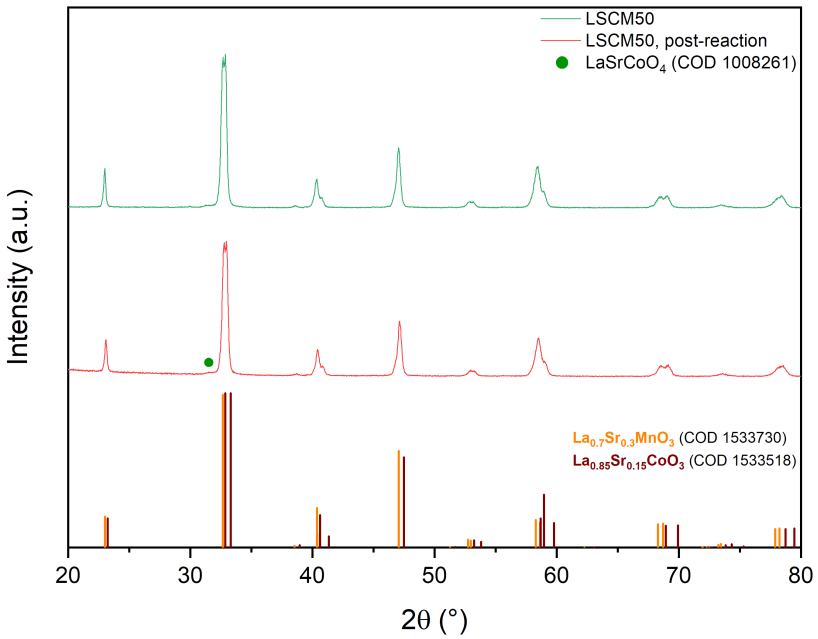

Figure 3.51: Comparison between LSCF50 diffraction patterns before and after the red-ox-red cycle.

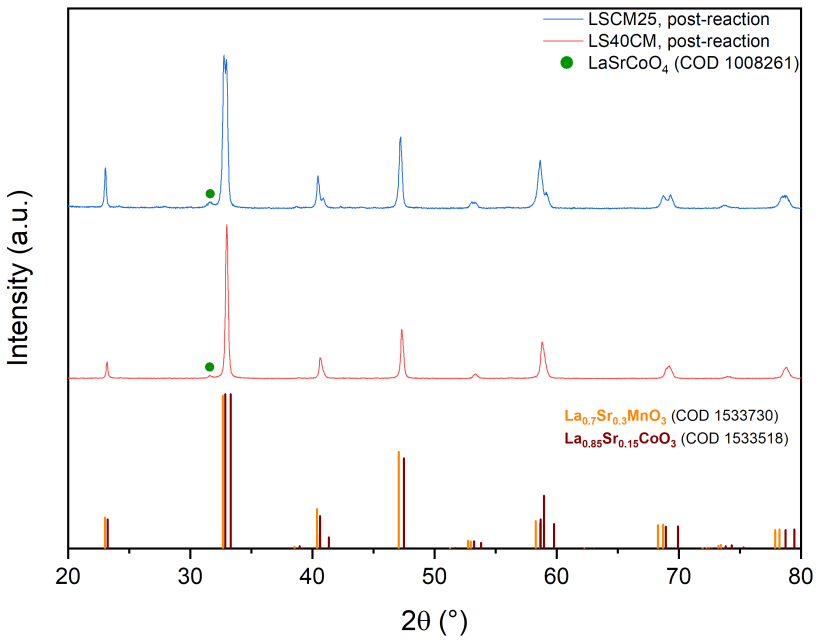

Figure 3.52: Diffraction patterns of LSCM25 and LS40CM after the red-ox-red cycle.

in Co have bigger but less reticulated scales.

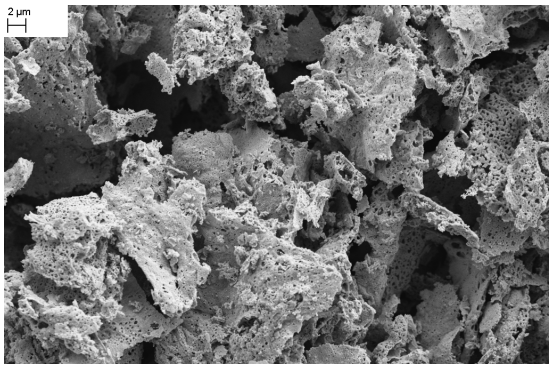

Figure 3.53: LSCM50 — 5000x

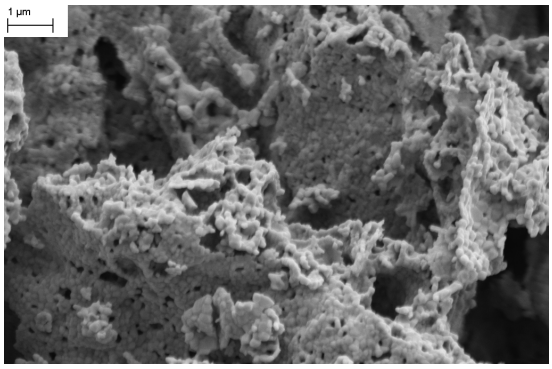

Figure 3.54: LSCM50 — 25000x

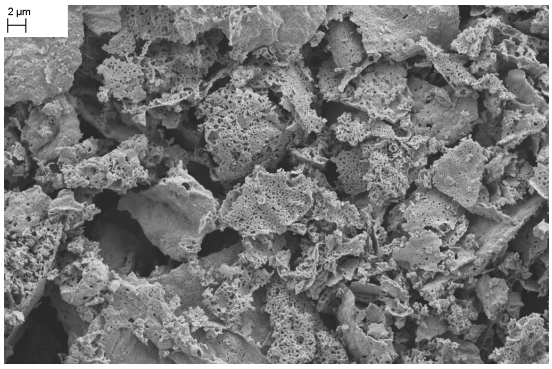

Figure 3.55: LSCM25 — 5000x

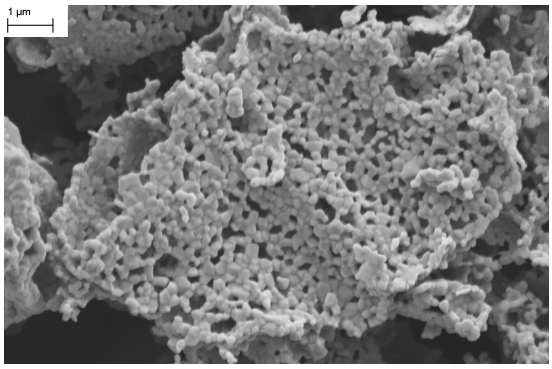

Figure 3.56: LSCM25 — 25000x

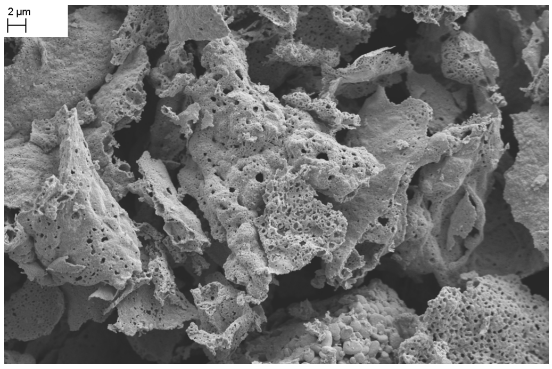

Figure 3.57: LS40CM — 5000x

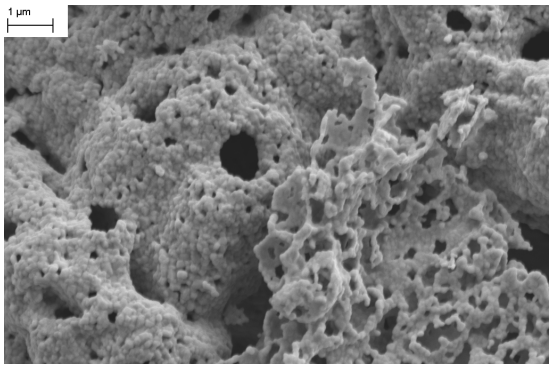

Figure 3.58: LS40CM — 25000x

Post-reaction

Similarly to what has been observed for LSCF, even LSCM do not show any sintering after two catalytic cycles (images 3.59 and 3.60, and A.14 to A.17).

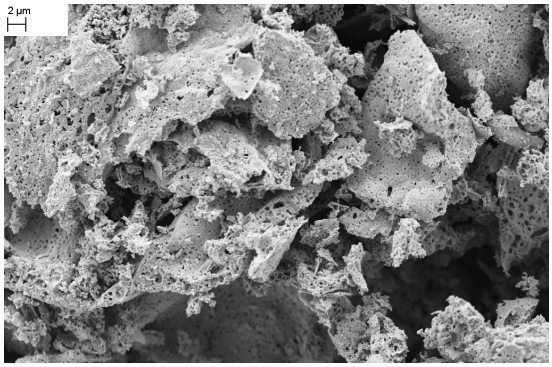

Figure 3.59: LSCM50 post-reaction — 5000x

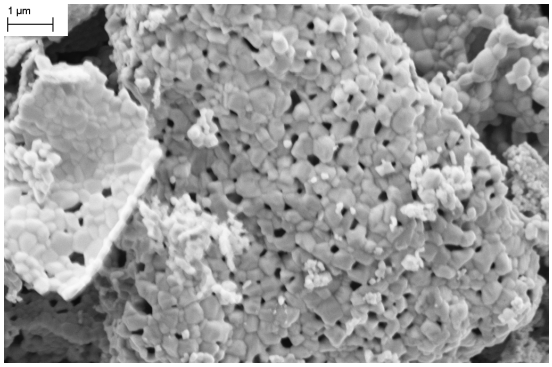

Figure 3.60: LSCM50 post-reaction — 25000x

3.4.3 Composition

As already observed for similar compounds, the compositions of these three materials (in tables 3.18, 3.19, 3.20) have features that appear similar to those of LSCF. Co and (in this case) Mn ratios are close to the expected ones, while La is always in excess and Sr in defect.

Table 3.18: Composition of LSCM50.

Element	Theoretical	Fresh		Post-reaction	
		EDX	XPS	EDX	XPS
La	0.80	0.92	0.88	0.88	0.87
Sr	0.20	0.14	0.24	0.18	0.30
Co	0.50	0.47	0.34	0.44	0.32
Mn	0.50	0.48	0.53	0.49	0.54

Table 3.19: Composition of LSCM25.

Element	Theoretical	Fresh		Post-reaction	
		EDX	XPS	EDX	XPS
La	0.80	0.95	0.86	0.89	0.77
Sr	0.20	0.17	0.23	0.18	0.37
Co	0.75	0.63	0.66	0.66	0.59
Mn	0.25	0.25	0.25	0.27	0.27

Even in this case, the XPS analysis of the material confirms that there is a degree of Sr segregation on the surface, higher when there is more strontium in the perovskite (as expected — see table 3.20). On top of that, the amount of cobalt appears to be always lower than the nominal composition.

Table 3.20: Composition of LS40CM.

Element	Theoretical	Fresh		Post-reaction	
		EDX	XPS	EDX	XPS
La	0.60	0.67	0.56	0.66	0.50
Sr	0.40	0.34	0.55	0.36	0.58
Co	0.75	0.72	0.67	0.73	0.62
Mn	0.25	0.27	0.24	0.25	0.31

Post-reaction

The comparison between pre- and post-reaction surface compositions shows many features in common with the previously observed ones.

In particular, the percentage of superficial cobalt is lower than expected but, mainly, there is a great excess (up to +85% in the case of LSCM25) of strontium. The relative amount of Sr is higher after two cycles than in the fresh material: this might pose stability issues over many catalytic activity.

3.4.4 XPS: qualitative analysis

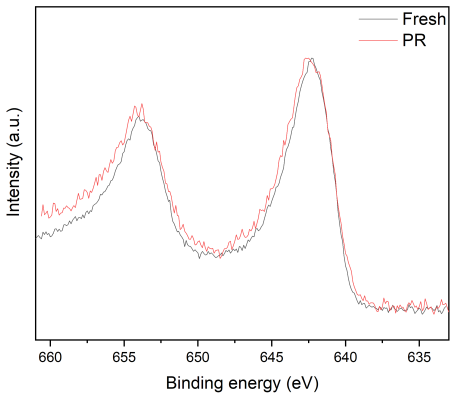

Figure 3.61: LSCM - Mn2p.

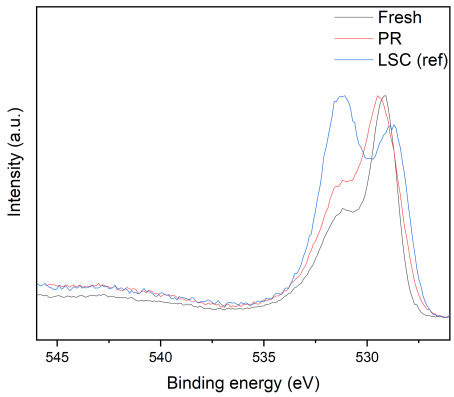

Figure 3.62: LSCM - O1s.

Mn2p (3.61) has the main peak ($2p\frac{3}{2}$) slightly above 642 eV, typical of manganese oxides. In particular, the peak position is compatible with the presence of Mn(III) and/or Mn(IV). The peaks shape does not change thus suggesting that no significant changes can be induced by the treatment on the Mn(III)/Mn(IV) surface atomic ratio. The absence of a satellite peak at about 646 eV excludes the presence of Mn^{2+}, even in the post-reaction

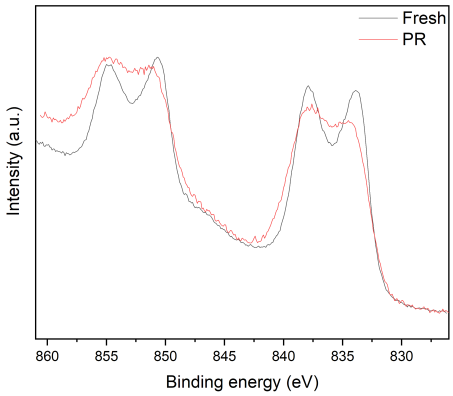

Figure 3.63: LSCM - La3d.

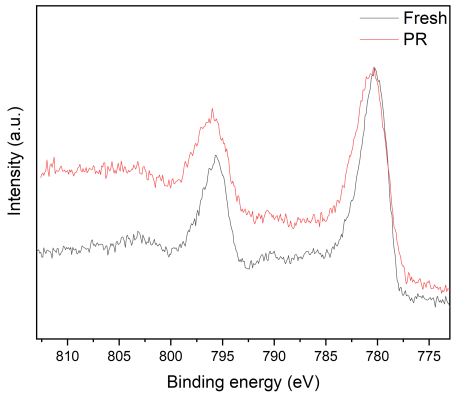

Figure 3.64: LSCM - Co2p.

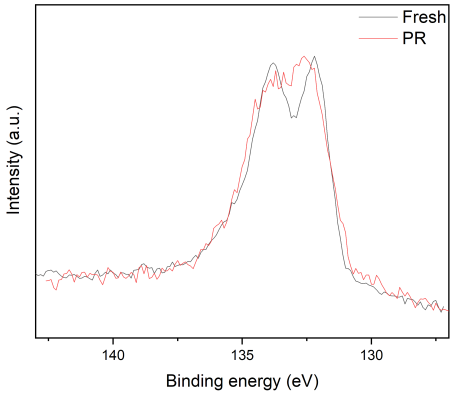

Figure 3.65: LSCM - Sr3d.

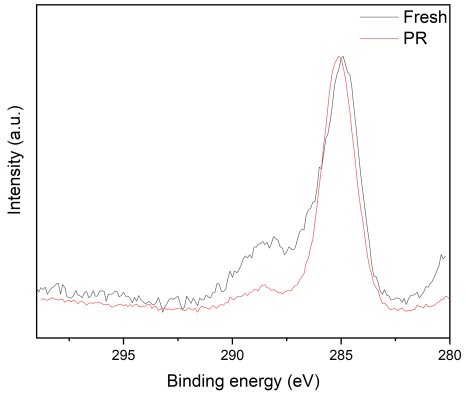

Figure 3.66: LSCM - C1s.

material.[69]

O1s (3.62) two components, the first attributed to lattice oxygen (at 529.2 eV), the second (at 531 eV) attributed to surface oxygen-containing species (hydroxyl and carbonates). This last peak is even weaker than the LSCF one (in blue, the LSC profile is compared), because of a lesser extent of these species on the surface. The already mentioned increase in the peak at higher BE in the post-reaction material is due to SiO_2.[69]

La3d (3.63), showing $3d\frac{5}{2}$ (834 eV) and $3d\frac{3}{2}$ (851 eV) components, has no relevant shifting between the pre- and post-reaction material. The peaks, though, increase in FWHM after the reaction, possibly indicating the presence of a higher amount of hydroxides and other compounds, decreasing the purity of the perovskite phase on the surface.

Co2p (3.64), in a similar manner, shows typical peaks (for Co(III)) at the same BE for pre- and post-reaction samples (780.2 eV, without satellites at 786 eV which might

indicate Co(II)), but with an increase in FWHM, which might be due to the emergence of hydroxides.

The peak of Sr3d (3.65) at lower binding energies can be found at 132.2 eV, and it has an intensity comparable to the one of the second peak (133.8 eV), confirming the presence of both oxides and carbonates. In the post-reaction material the intensity ratio is in favour of the oxide peak: C1s spectrum (3.66) is in agreement with a decrease of the carbonate contribution observable in the peak at 288.4 eV, after normalisation on the peak attributed to the adventitious carbon (284.8 eV).[69]

3.4.5 Surface area

This family of materials shows specific surface areas higher than LSCF, ranging between 2.0 m^2/g and 3.5 m^2/g, as in table 3.21. This is in agreement with literature results for $LaMnO_3$ compared to $LaFeO_3$ in similar conditions.[72]

Table 3.21: BET surface areas of LSCM perovskites.

Sample	Specific surface area (m^2/g)
LSCM50	3.390 ± 0.068
LSCM25	3.42 ± 0.11
LS40CM	2.021 ± 0.055

In this case, the variation in specific surface area from LSCM50 to LSCM25 (increasing Co content) is almost negligible. Nevertheless, the great decrease after the addition of strontium is confirmed (-41%).

Pore size distributions (PSD, in figure 3.67) show a slight degree of variation, with the maximums increasing from 2.9 nm to 3.1 nm and 3.2 nm along the three materials. The range is about the same as the previous materials (1.9 nm to 7.5 nm) for LSCM50 and LSCM25, while a bit wider for LS40CM (1.8 nm to 8.3 nm). Nevertheless, all three materials are clearly mesoporous.[57]

Another BET analysis has been conducted on post-reaction LSCM50, measuring a specific surface area of $5.07 \pm 0.23\ m^2/g$, with an increase of almost 50% if compared to the fresh material (a phenomenon previously observed for LSC and LSCF50). The pore size distribution, in figure 3.67, is similar to the previous one, with a peak at 3.3 nm and a slightly wider range (1.7 nm to 9.1 nm).

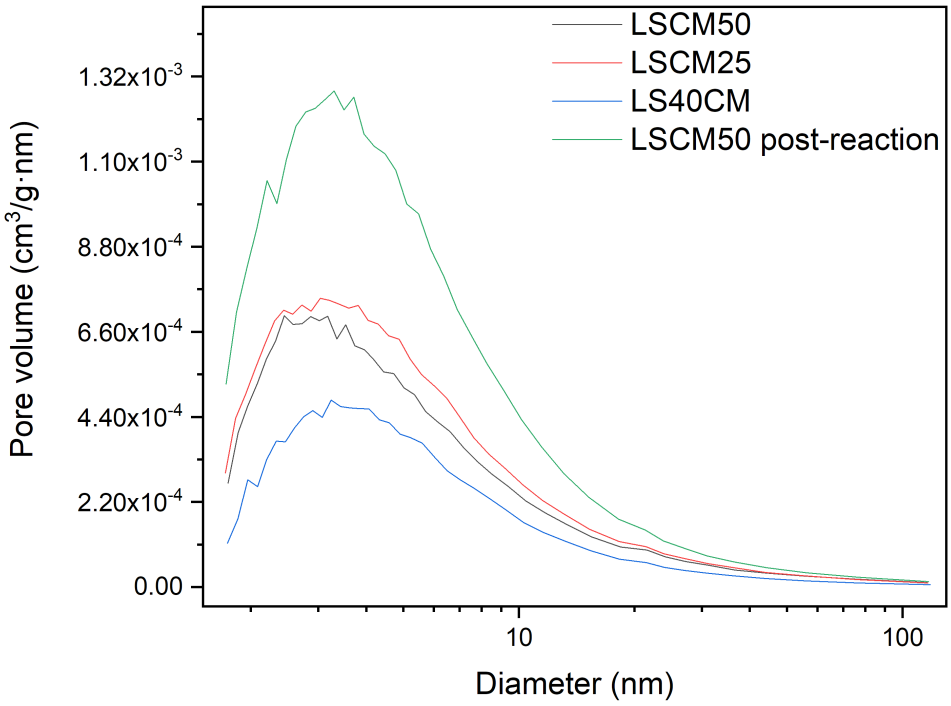

Figure 3.67: Pore size distribution of LSCM materials.

3.4.6 TPR

In figure 3.68 the TPR profiles of the three material of this last family are illustrated. They share many similar features with LSC (figure 3.28) and LSCF (figure 3.48).

However, the peaks that range from 400 °C to 450 °C are much wider than the previously observed ones: this is likely due to the overlapping between three processes, two of which have been already discussed earlier ($Co^{4+} \longrightarrow Co^{3+}$ and $Co^{3+} \longrightarrow Co^{2+}$), while the third one involves manganese ($Mn^{4+} \longrightarrow Mn^{3+}$).[81–83]

This is further confirmed by the shoulder at higher temperatures on the second peak of the LSCM50 curve, in the 600 °C to 800 °C range (that is due to the further reductions of $Mn^{3+} \longrightarrow Mn^{2+}$ and $Co^{2+} \longrightarrow Co^{0}$)[74,84]: it has been previously reported that the reduction of Mn(III) in perovskites falls at higher temperatures than Co(II), in similar conditions.[85]

Nevertheless, while quantifying the hydrogen consumption (displayed in table 3.22), it appears that the reduction is not complete: while the total amount of Co and Mn in the perovskite is 1 mol/mol (as both B-site cations are active in reduction reactions),

Table 3.22: Hydrogen consumption of LSCM materials in the two main steps of reduction.

Sample	Co, Mn (mol/mol)	Temperature range and center (°C)	H_2 (mol/mol)
LSCM50	0.5, 0.5	300-550 (435) 600-800 (690)	0.37 0.25
LSCM25	0.75, 0.25	300-550 (439) 600-800 (675)	0.44 0.38
LS40CM	0.75, 0.25	300-550 (415) 600-800 (635)	0.48 0.44

depending on the composition, the hydrogen consumption in the first step (with stoichiometry M:H_2=2:1, not taking into account the eventual amount of Co(IV)) ranges between 0.37 mol/mol and 0.48 mol/mol. This is even more evident in the second peak, where the same amounts of metal ions (with stoichiometry 2:1 for manganese and 1:1 for cobalt) react with just 0.25 mol/mol to 0.44 mol/mol of hydrogen, leading to an incomplete reduction of the material. This could be indicative of a low availability of the various oxidation states, although only the first steps of reduction are usually involved in the oxygen exchange reactions.[82]

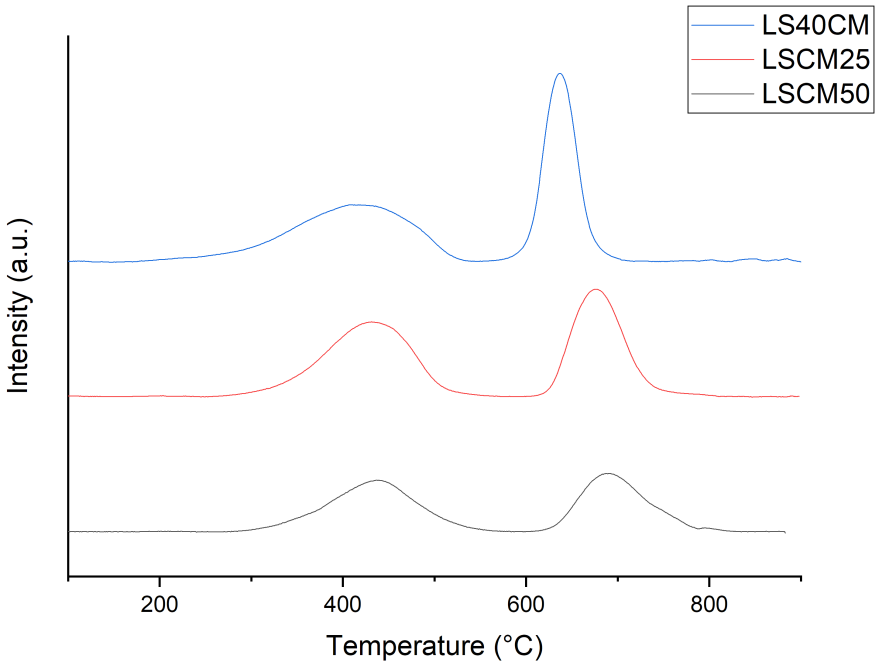

Figure 3.68: TPR profile of the three LSCM perovskites.

Despite this, it is clear that the amount of Sr in the sample positively correlates with the reducibility of the material: in both steps, LS40CM has the highest hydrogen consumption.

3.5 Compositions - summary

Table 3.23: Composition of all investigated materials.

Material	Element	Theoretical	Fresh		Post-reaction	
			EDX	XPS	EDX	XPS
LAN	La	1.00	0.97		1.14	
	Al	0.20	0.22		0.25	
	Ni	0.80	0.81		0.61	
LSC	La	0.80	0.84	0.77	0.78	0.69
	Sr	0.20	0.18	0.35	0.26	0.35
	Co	1.00	0.98	0.89	0.96	0.96
LSCN10	La	0.80	0.73		0.95	
	Sr	0.20	0.14		0.25	
	Co	0.90	1.02		0.69	
	Ni	0.10	0.12		0.11	
LSCF50	La	0.80	0.87	0.89	0.89	0.70
	Sr	0.20	0.18	0.25	0.16	0.56
	Co	0.50	0.45	0.64	0.48	0.51
	Fe	0.50	0.50	0.23	0.48	0.21
LSCF25	La	0.80	0.88	0.75	0.88	0.86
	Sr	0.20	0.17	0.21	0.15	0.23
	Co	0.75	0.69	0.68	0.70	0.63
	Fe	0.25	0.26	0.36	0.27	0.28
LS40CF	La	0.60	0.74	0.67	0.72	0.55
	Sr	0.40	0.20	0.32	0.23	0.55
	Co	0.75	0.79	0.72	0.74	0.67
	Fe	0.25	0.26	0.28	0.25	0.23
LSCM50	La	0.80	0.92	0.88	0.88	0.87
	Sr	0.20	0.14	0.24	0.18	0.30
	Co	0.50	0.47	0.34	0.44	0.32
	Mn	0.50	0.48	0.53	0.49	0.54
LSCM25	La	0.80	0.95	0.86	0.89	0.77
	Sr	0.20	0.17	0.23	0.18	0.37
	Co	0.75	0.63	0.66	0.66	0.59
	Mn	0.25	0.25	0.25	0.27	0.27
LS40CM	La	0.60	0.67	0.56	0.66	0.50
	Sr	0.40	0.34	0.55	0.36	0.58
	Co	0.75	0.72	0.67	0.73	0.62
	Mn	0.25	0.27	0.24	0.25	0.31

Chapter 4

Oxygen exchange

4.1 Results

Measures of released oxygen for each material have been conducted as follows: 200 mg of sample have been placed in a U-shaped tubular quartz reactor over a quartz wool bed and exposed to a flow of 50 sccm He. While flowing the carrier, the sample has been heated up to 600 °C with a ramp of 10 °C/min and then up to 1000 °C at 5 °C/min, at the end of which the material was kept at 1000 °C for 15 min. This has been done while recording the difference in conductivity between the pure carrier and the gas coming from the sample. In order to quantify the released oxygen, assuming a continuous release at high temperatures, every hundred degrees starting at 600 °C the flow was modified excluding the sample, allowing to have a baseline of (theoretically) pure He against pure He. Areas between the curve and the baseline have been integrated to correlate the value to the oxygen quantity through a previous calibration.

The sample was then cooled to room temperature at 10 °C/min while flowing 50 sccm of 5% O_2 in He, with a 30 min break at 850 °C, in order to oxidise all the material. Then, another heating cycle in He was conducted as mentioned before, and the resulting material was cooled without gas flow in the leftover helium and then analysed.

Four measurements of the background have been conducted, placing in the instrument an empty reactor with just quartz wool in it and exposing it to the same conditions. A virtual mass of 200 mg has been considered for the quantification of the background values in mL/g.

4.1.1 LAN

The results for LAN after integration and background subtraction are illustrated in figure 4.1, expressed in STP millilitres of $O_{2(g)}$ released per gram of material at each 100 °C interval.

The total is 4.34 mL/g in the first cycle and 3.01 mL/g in the second one, with a 31% decrease. This originates mainly from a sharp decrease in the last segment (900-1000 °C), that falls from 3.43 mL/g to 1.82 mL/g between the two cycles (−47%).

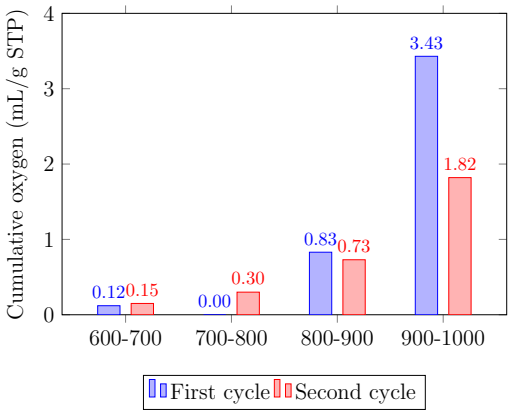

Figure 4.1: Oxygen release of LAN.

4.1.2 LSC

Figures 4.2 and 4.3 illustrate the results of oxygen release measurements for LSC and LSCN10 respectively. The activity appears to be much higher than the previously discussed LAN, with a total of 9.72 mL/g for LSC and 12.57 mL/g for LSCN10 in the first cycle. After the oxidation, though, the released quantity is much lower, totalling 3.18 mL/g for LSC (−67%) and 5.80 mL/g for LSCN10 (−54%).

The trend across temperatures in LSC might raise some questions: there is a very high spike in the 800-900 °C interval, that corresponds to more than 50% of the total oxygen released, which is not observed again in the second cycle. To explain this, a TPD of the material has been conducted (without breaking the flow every 100 °C, although this makes it difficult to quantify the continuous release at higher temperatures, highlighting only the evident peaks of oxygen production). Results can be seen in figure 4.4.

Quantification of this two observable peaks can be found in table 4.1.

As per the aforementioned figure, another peak at 445 °C appears in the profile. This was not included in the previous quantification, since it only ranged between 600 °C

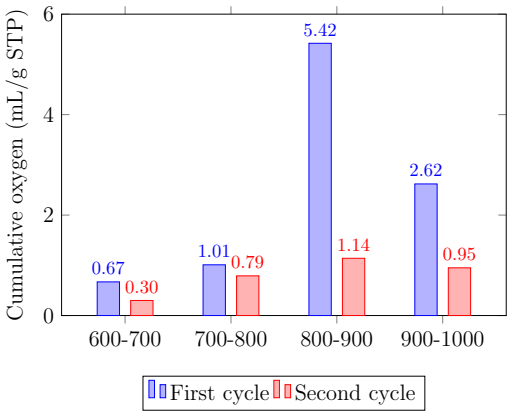

Figure 4.2: Oxygen release of LSC.

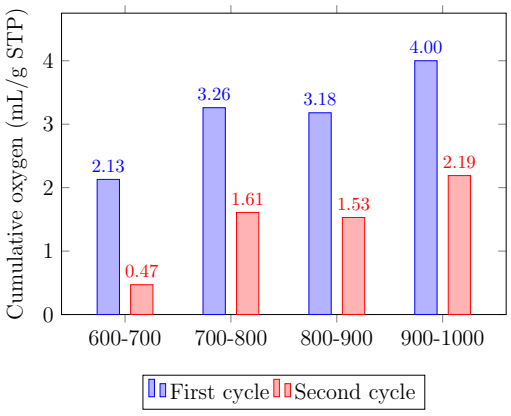

Figure 4.3: Oxygen release of LSCN10.

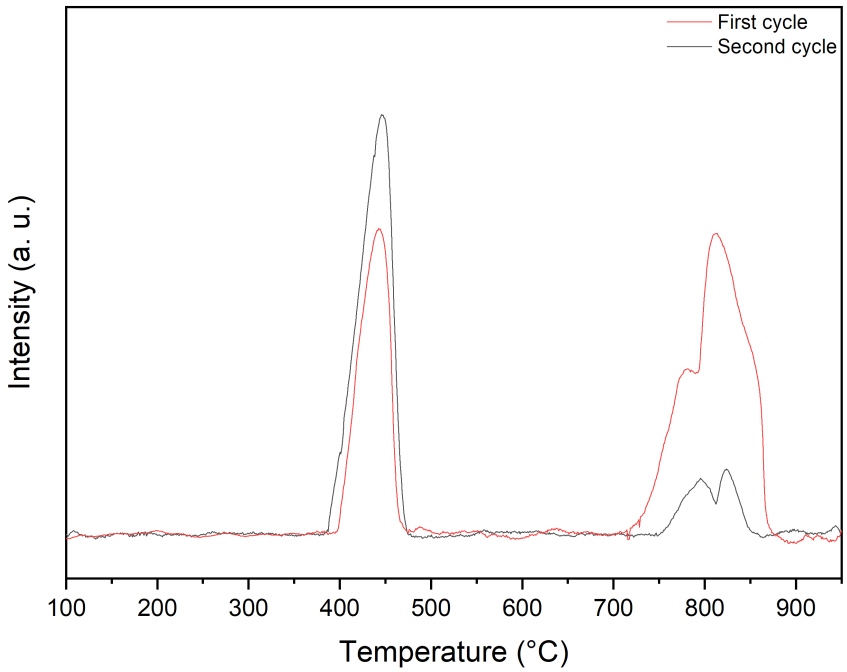

Figure 4.4: Comparison between first and second catalytic cycle of LSC.

Table 4.1: Released oxygen (mL/g STP).

Cycle n.	400-500 °C	700-900 °C
1	3.02	5.36
2	4.63	1.07

and 1000 °C and was conducted in assumption that oxygen was released only at high temperatures, and therefore did not add up to the total oxygen release: the new total

values are 12.74 mL/g for the first cycle and 7.81 mL/g for the second one (−39%).

4.1.3 LSCF

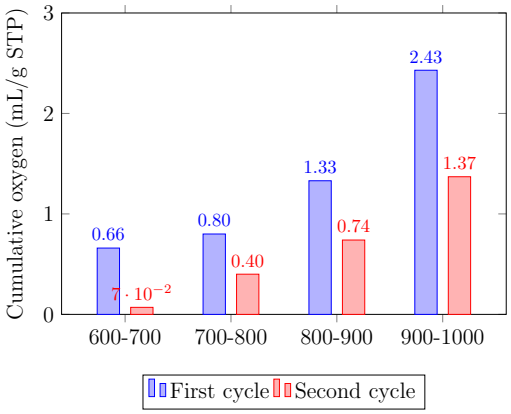

Figure 4.5: Oxygen release of LSCF50.

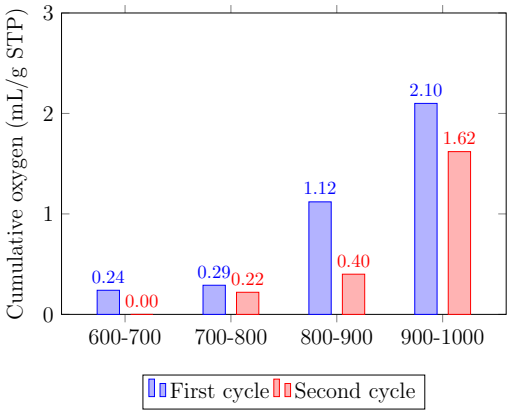

Figure 4.6: Oxygen release of LSCF25.

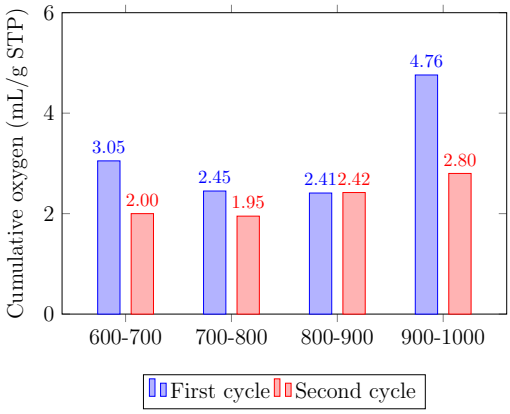

Figure 4.7: Oxygen release of LS40CF.

TPD measurements over two cycles have been conducted on this family of materials with the method described in section 2.4. Results of the quantifications are illustrated in figures 4.5, 4.6 and 4.7.

The total oxygen released is 5.21 mL/g for LSCF50, 3.75 mL/g for LSCF25 and 12.67 mL/g for LS40CF in the first cycle. After re-oxidation of the material, in the second cycle the materials produced 2.59 mL/g (−50%), 2.15 mL/g (−43%) and 9.17 mL/g (−28%) respectively.

While LSCF50 and LSCF25 show a typical trend of gradually increasing oxygen release,[86] LS40CF decreases after the first step (3.05 mL/g to 2.45 mL/g) and then has the maximum in the last step, as expected. The trend might be confirmed by the second

cycle, although the very small difference (0.05 mL/g) is not really indicative of a decrease but just of the absence of a relevant increase between the two steps.

4.1.4 LSCM

Figures 4.8, 4.9 and 4.10 show the measured oxygen release of the three materials of the LSCM family.

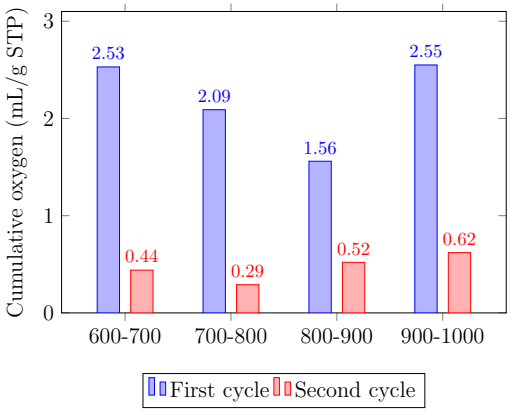

Figure 4.8: Oxygen release of LSCM50.

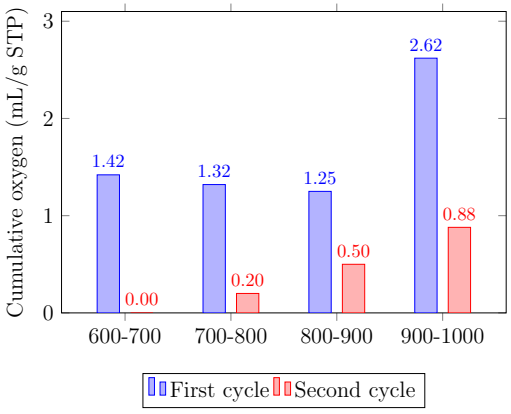

Figure 4.9: Oxygen release of LSCM25.

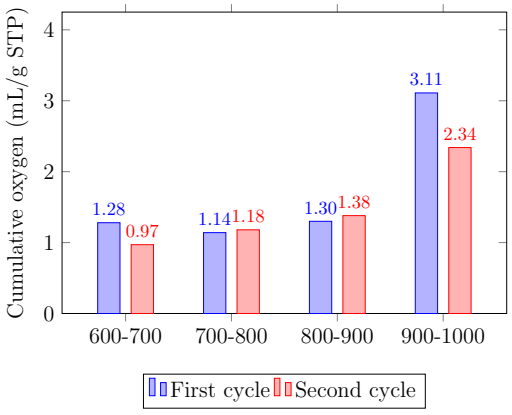

Figure 4.10: Oxygen release of LS40CM.

LSCM50 releases 8.72 mL/g of oxygen in the first cycle, while LSCM25 stops at 6.61 mL/g and LS40CM at 6.81 mL/g. In terms of cyclability, the decrease in the second cycle is very sharp for LSCM50 (1.87 mL/g, −79%) and LSCM25 (1.49 mL/g, −77%), while LS40CM maintains a good oxygen release (5.87 mL/g, −13%).

For all the first cycles and also for the second cycle of LSCM50, the growth from the first to the fourth step is not monotonous: the oxygen release between 600 °C and 700 °C is high, with a minimum in the second (LSCM50-2, LS40CM-1) or third (LSCM50-1,

LSCM25-1) step and the absolute maximum in the last interval. On the other hand, for the remaining two cycles (LSCM25-2, LS40CM-2) the growth is monotonous.

4.2 Discussion

In table 4.2, all measured oxygen release values are summarized.

Table 4.2: Released oxygen (mL/g STP) .

Sample	Composition	First cycle	Second cycle	Loss
LAN	$LaAl_{0.2}Ni_{0.8}O_3$	4.34	3.01	31%
LSC	$La_{0.8}Sr_{0.2}CoO_3$	12.74	7.81	39%
LSCN10	$La_{0.8}Sr_{0.2}Co_{0.9}Ni_{0.1}O_3$	12.57	5.80	54%
LSCF50	$La_{0.8}Sr_{0.2}Co_{0.5}Fe_{0.5}O_3$	5.21	2.59	50%
LSCF25	$La_{0.8}Sr_{0.2}Co_{0.75}Fe_{0.25}O_3$	3.75	2.15	43%
LS40CF	$La_{0.6}Sr_{0.4}Co_{0.75}Fe_{0.25}O_3$	12.67	9.17	28%
LSCM50	$La_{0.8}Sr_{0.2}Co_{0.5}Mn_{0.5}O_3$	8.72	1.87	79%
LSCM25	$La_{0.8}Sr_{0.2}Co_{0.75}Mn_{0.25}O_3$	6.61	1.49	77%
LS40CM	$La_{0.6}Sr_{0.4}Co_{0.75}Mn_{0.25}O_3$	6.81	5.87	13%

The first two materials can be compared to the reported data from Pérez et al.[23] and Orfila et al.[24]: the reported hydrogen production is 4.4 mL/g for LAN and 15.8 mL/g for LSC. Considering a theoretical stoichiometry of 2:1 for H_2:O_2 (an assumption not always verified, with real values ranging from 1.8 to 2.0)[32,87] this corresponds to an oxygen release of 2.2 mL/g for LAN and 7.9 mL/g for LSC. Actual oxygen release of LSC has been measured, with an initial value slightly below 10.5 mL/g in the first cycle and a stabilisation at about 8.2 mL/g over more cycles.[23,24]

The measured values are in agreement with the mentioned results. For LAN, the value is higher, but it has to be noted that in literature the cycles are conducted at 800 °C both for reduction and for oxidation, therefore a higher reduction temperature might lead to a higher oxygen release. However, there is a larger decrease between the first and the second cycle: this is observed by Pérez et al.[23] while working with thermal reductions at 1000 °C and it is due to the segregation of less-active phases that can be observed in the diffraction pattern in section 3.1. The value for LSC is higher than the reported value in the first cycle but lower in the second, although it is really close to the average.[24]

The addition of nickel in LSC (LSCN10) results in keeping a high release of oxygen even with the loss of the peak at 450 °C in the O_2-desorption measure, which could be observed for LSC (as in figure 4.4). Nevertheless, in the second cycle there is a drastic decrease (-54%) which suggests that the material has a very low cyclability. The post-reaction diffraction pattern (in section 3.1) shows a variety of secondary phases segregating after the cycles, a phenomenon that can be detrimental for the activity of the material if the new phases are not as active as the main one: in this case, the great decrease in oxygen

release confirms that the new phases are indeed less active for this reaction.

According to the literature, released oxygen comes from three main sources: surface, grain boundaries and bulk. On the surface the main species are O^- and O^{2-} (and occasionally the superoxide species $O_2{}^-$), while only O^{2-} occurs on grain boundaries and in the bulk.[88] M^{n+} / $M^{(n-1)+}$ redox couples are active in oxygen exchange reactions: upon reduction of surface ions, superficial oxygen is released (usually referred to as *α-oxygen*). Then, through formation and mobility of oxygen vacancies, the surface exchanges with the grain boundaries, with a further release of O_2 at higher temperatures (*β-oxygen*). Finally, at high temperatures (reportedly $> 900\,°C$) bulk oxygen is activated and partially released.[14,88]

The inferior values for LSCF50 and LSCF25 with respect to LSCM50 and LSCM25 can be explained by the lower reducibility of iron perovskites, if compared to manganese ones.[88,89] This is further supported by the TPR profiles: LSCM perovskites have an higher hydrogen consumption in the first peak (between 350 °C and 600 °C) if compared to LSCF (tables 3.14 and 3.22). The processes involved in this step of reduction are the same involved in oxygen mobility: the main contribution comes from cobalt reduction ($Co^{4+} \longrightarrow Co^{3+}$ and $Co^{3+} \longrightarrow Co^{2+}$), with also manganese reduction in the case of LSCM ($Mn^{4+} \longrightarrow Mn^{3+}$):[81–83] in the case of manganese doping, the attitude of the dopant to easily form the species Mn(IV) might enhance the release of oxygen.

Nevertheless, losses over 70% between the first and the second cycle show that manganese materials have a very low cyclability, despite the good results in post-reaction XRD (section 3.4) where no new phase can be found and with general low level of impurities. This can be explained by the lower oxygen mobility observed in manganese perovskites compared to iron ones:[90] it is possible that, after releasing oxygen in the first cycle from the surface and the grain boundaries, the material is not able to fill the formed vacancies successfully, therefore not having enough oxygen to release it in the second cycle.

In the case of La:Sr= 60 : 40 in the A-site, a much greater oxygen release is observed. This behaviour is widely reported in literature and is further confirmed by the present materials.[31,32,91,92] This is due mainly to the formation of M^{4+} species to compensate Sr^{2+} in the A-site: as discussed before, Co^{4+} and Mn^{4+} are ready to exchange oxygen while reducing to the corresponding M^{3+} species. Moreover, the strontium−oxygen bond has a lower dissociation energy if compared to lanthanum in oxide lattices:[93] it is therefore predictable that a larger amount of Sr in the structure decreases the energy requirements for the reaction of both superficial and bulk oxygen. Combined with the higher mobility of oxygen ions in iron perovskites, this explains the high value for LS40CF (12.67 mL/g), almost double the quantity measured for LS40CM (6.81 mL/g).

Notably, the positive effect of strontium doping both in vacancy formation and oxygen mobility guarantees a modest loss in the second cycle, as low as −28% for LS40CF and −13% for LS40CM. If the former is comparable to the one of LAN (but with a net oxygen release which is almost triple), the latter is the lowest observed value and a very low value overall, taking into account the fact that the first cycle is often an "activation" cycle, in which it is usual that not all the lost oxygen is recovered afterwards.[23,24]

Profiles of oxygen release allow to have an insight in the specific mechanism of each material. LSC is the only one to have a clear and observable α-oxygen peak at low temperatures (450 °C) and a β-oxygen peak around 800 °C. Interestingly, this second peak is almost not detectable in the second cycle (−80%), while the first one is maintained and even increased. This might be due to an inefficient oxygen mobility in the material, which allows the total recovery of oxygen on the surface (α) but not on grain boundaries and in the bulk (β).

LAN, LSCF50 and LSCF25 show a monotonous growth in the quantity of released oxygen across temperatures, showing that it is exchanged in a temperature-activated process. It is not possible, in this case, to discriminate between α- and β-oxygen.

LS40CF, LSCM50, LSCM25 and LS40CM, on the other hand, show a clear relative maximum in the first measured step (600-700 °C) that suggests the presence of an α-oxygen contribution to the exchange. The higher extent of strontium doping is known to have the effect of enhancing the α-oxygen peak, thus favouring exchange at lower temperatures.[14] The release of low-temperature α-oxygen for manganese perovskites has not been observed by the same studies.[14,94]

The abrupt start at more than 2 mL/g of some of the materials in the first step (namely LSCN10, LS40CF, LSCM50) suggests that the oxygen exchange process is already active at lower temperature, and should then be investigated with TPD studies across the whole range.

Starting from the obtained values of oxygen release it is possible to calculate the new stoichiometry of the perovskite $ABO_{3-\delta}$ in terms of δ. Results are displayed in table 4.3. This was calculated in the assumption that all the oxygen release processes happened in a stoichiometric reduction of the positive ions in the material. It has to be considered that, since perovskites are well known to be able to accommodate a number of oxygen vacancies relocating the electrons,[13] this has to be taken as the theoretical maximum extent of reduction in the material.

The mechanism for LAN might involve the reduction of Ni^{3+} to Ni^{2+}, which happens at low temperatures as observed by the TPR (peak at 370 °C). Therefore, there is no

Table 4.3: Stoichiometric oxygen release of the thermally reduced perovskites.

Material	δ
LAN	0.09
LSC	0.27
LSCN10	0.26
LSCF50	0.11
LSCF25	0.08
LS40CF	0.25
LSCM50	0.18
LSCM25	0.14
LS40CM	0.14

theoretical limitation to the released oxygen, although the value of δ suggests that only about 18% of the nickel is involved in the reaction $0.18\,Ni^{3+} + 0.09\,O^{2-} \longrightarrow 0.18\,Ni^{2+} + 0.09\,O$ (if the reaction is assumed to occur stoichiometrically).

For all the other materials, as discussed above, the process involved is the reduction of M^{4+} species to M^{3+} in the following reaction:

$$2\,M^{4+} + O^{2-} \longrightarrow 2\,M^{3+} + O$$

Since this species are present in the material because of the charge disequilibrium derived from Sr^{2+}, it is expected that the oxygen deficiency is directly correlated to the stoichiometry of strontium in the formula. Therefore, the presence of 4+ species can account for $\delta = 0.2$ in the case of LS40CF and LS40CM and $\delta = 0.1$ for all the other materials. LS40CM is the only one for which a stoichiometric reduction could be assumed, since the value of $\delta = 0.14 < 0.2$, but for all the other materials other processes should be taken into account, confirming the aforementioned presence of oxygen vacancies. On top of that, post-reaction diffraction pattern of LSCN10 (section 3.2) shows the presence of CoO, suggesting that some of the oxygen release comes from the further reduction of Co^{3+} to Co^{2+}. This is excluded in the case of LSC, the other material with a very high δ, since post-reaction XPS analysis shows no trace of the satellite peak for Co^{2+}, as discussed.

To fully explain the observed behaviour, nonstoichiometric processes are likely to be involved: besides the stoichiometric reduction to M(III) and M(II) species, vacancies can form in the crystal lattice leaving behind two electrons which are then coordinated by the positive ions, allowing a further release of O_2 without the need for additional reduction.[13,93]

Chapter 5

Conclusions and outlooks

Hydrogen is a promising energy carrier for future applications in net-zero emissions energy systems,[5,11] although several problems need to be addressed in terms of storage and production.[7] In particular, a relevant amount (more than 80%) of the commercial hydrogen comes from fossil sources, with large CO_2 emissions.[8]

Many steps towards a greener hydrogen production (obtained from water splitting) have been made, in particular for electrolysis,[95,96] while thermolysis is less explored.[11] For this reason, the present thesis work focused on materials that can be used as catalysts in cycles of thermal reduction and subsequent oxidation in hot steam. The two involved reactions can be schematised as follows:

$$MO_x \xrightarrow{\Delta} MO_{x-\delta} + \frac{\delta}{2}O_2$$

$$MO_{x-\delta} + \delta H_2O_{(g)} \longrightarrow MO_x + \delta H_2$$

Typical catalysts for this reaction, such as doped ceria, ferrites and perovskites, usually operate at a reduction temperature of 1400 °C.[16,19] In this work, one of the main goals was to find materials with satisfying activity at lower temperatures, up to 1000 °C.

Typical oxygen release values for these materials, displayed in table 5.1, range from 3 mL/g to 9 mL/g STP of O_2.

Table 5.1: Oxygen release values representative of state-of-the-art materials.

Material	T_{red} (°C)	H_2 (mL/g STP)	O_2 (mL/g STP)
$Ce_{0.8}Zr_{0.2}O_2$[25]	1400	9.5	4.8*
$Ni_xFe_{3-x}O_4/ZrO_2$[18]	1400	15	7.5*
$LaCoO_3$[26]	1300	/	8.3

For the aforementioned temperature boundaries, the starting points were two perovskites recently described to be active at low temperatures, namely $La_{0.8}Al_{0.2}NiO_3$

($T_{red} = 800\,°C$)[23] and $La_{0.8}Sr_{0.2}CoO_3$ ($T_{red} = 1000\,°C$)[24].

A self-combustion synthesis route was chosen for all material, since this approach is water-based and scalable. For nickel-containing perovskites, Pechini method was followed (with citrate and ethylene glycol as complexing agents), while Marcilly method was used for all the others, as detailed in section 2.2.

The actual composition of the first one has been discussed and found to be $LaAl_{0.2}Ni_{0.8}O_3$ (LAN). This material has proved to be difficult to synthesize, with many impurities emerging in the diffraction pattern even while following the literature process, therefore no further work except the full characterisation has been conducted on this path.

$La_{0.8}Sr_{0.2}CoO_3$ (LSC) has been synthesized in good purity, with properties in agreement with those mentioned by the literature. Several changes have been made on this composition, with various degrees of B-site doping with Ni, Fe and Mn and different A-site ratios, summarized in table 5.2. These other cations have been chosen because of their comparable activity in similar reactions and since they are more sustainable, in particular in the case of iron and manganese, as these two elements are cheaper, safer and more abundant.[40,97] Similar materials have been investigated in literature, but without a precise comparison between different A-site and B-site compositions, and often overlooking the mechanism of oxygen release at various temperatures.

Table 5.2: Various doping of LSC.

Composition	Abbreviation
$La_{0.8}Sr_{0.2}Co_{0.9}Ni_{0.1}O_3$	LSCN10
$La_{0.8}Sr_{0.2}Co_{0.5}Fe_{0.5}O_3$	LSCF50
$La_{0.8}Sr_{0.2}Co_{0.75}Fe_{0.25}O_3$	LSCF25
$La_{0.6}Sr_{0.4}Co_{0.75}Fe_{0.25}O_3$	LS40CF
$La_{0.8}Sr_{0.2}Co_{0.5}Mn_{0.5}O_3$	LSCM50
$La_{0.8}Sr_{0.2}Co_{0.75}Mn_{0.25}O_3$	LSCM25
$La_{0.6}Sr_{0.4}Co_{0.75}Mn_{0.25}O_3$	LS40CM

Diffraction patterns confirm the crystallisation in the desired phase for all of them. SEM images show a scale-like morphology with a reticulate structure. From EDX and XPS compositions, slight deviation from ideality can be observed in all samples. In particular, this is noticed for Sr, which has the tendency to segregate on the surface.[63] This is balanced by an excess of La in the deeper layers, as confirmed by EDX. Please refer to chapter 3 for full information on the topic here discussed.

N_2 adsorption isotherms allowed to calculate specific surface areas. These are the range from $1.5\,m^2/g$ to $4.0\,m^2/g$ for all cobalt-containing materials, while LAN reaches

more than $9\,m^2/g$. Pore size distribution, with a maximum usually between 3.0 nm and 3.5 nm, indicates that all the materials are mesoporous, as confirmed by the shape of adsorption isotherms.[57]

The post-reaction material has undergone the same analyses conducted on the fresh sample. Diffraction patterns show mixed results: while LAN and LSCN10 appear to be degraded, only slight modifications emerge from the analysis of LSC and the two families of LSCF and LSCM. SEM images confirm the initial morphology, without any major sintering. The composition is further deviated in some samples, with a great amount of Sr on the surface especially in LSCM, as observed by EDX analysis. Surface areas appear to have increased by an average 40%, while the pore size distribution is maintained.

XPS spectra of every element present in the material have been taken for LSC, LSCF50 and LSCM50, both fresh and post-reaction. Different amounts of surface hydroxides and carbonates have been observed in O1s, C1s and Sr3d spectra. The quantity of these species is particularly relevant in the case of LSC (section 3.2), for both pre- and post-reaction samples. Progressively decreasing quantities are found in LSCF50 and LSCM50.

TPR measures in 10% H_2/Ar on the fresh sample are coherent with the expected behaviours for the material, with Co(IV) and Co(III) reacting at low temperatures (350 °C to 450 °C), together with Mn(IV). Nickel appears to be stabilised both in LAN, partially, with a high temperature peak, and in LSCN10 (in which the two peaks fall above 550 °C). The extent of reduction is increased by the amount of strontium in the A-site, as confirmed by the quantifications of consumed H_2.

Measures of thermal conductivity of an inert gas flowing on the sample allowed to determine the quantity of oxygen released by the material over two catalytic cycles, obtaining information about the cyclability of the various compositions. The most relevant results are displayed in table 5.3

Table 5.3: Released oxygen (mL/g STP) .

Sample	Composition	First cycle	Second cycle	Loss
LAN	$LaAl_{0.2}Ni_{0.8}O_3$	4.34	3.01	31%
LSC	$La_{0.8}Sr_{0.2}CoO_3$	12.74	7.81	39%
LSCF50	$La_{0.8}Sr_{0.2}Co_{0.5}Fe_{0.5}O_3$	5.21	2.59	50%
LS40CF	$La_{0.6}Sr_{0.4}Co_{0.75}Fe_{0.25}O_3$	12.67	9.17	28%
LSCM50	$La_{0.8}Sr_{0.2}Co_{0.5}Mn_{0.5}O_3$	8.72	1.87	79%
LS40CM	$La_{0.6}Sr_{0.4}Co_{0.75}Mn_{0.25}O_3$	6.81	5.87	13%

Results from both LAN and LSC are comparable to those in the literature, confirming the high activity of LSC. A slightly higher value for LAN is due to the higher reduction

temperature (1000 °C).

Evaluating in particular the second cycle, which is usually closer to the average value over a long number of cycles, all new materials except LSCM50 (and LSCM25) have results in the same range as state-of-the-art materials. Nevertheless, reduction temperatures are much lower than the reported ones for ceria and ferrites (over 1400 °C). LSCM50 actually has a good first-cycle oxygen release, but with a 79% loss in the second cycle the cyclability is excluded.

The lower results for low-strontium iron perovskites can be explained because of the lower reducibility if compared to manganese ones.[88] Nevertheless, the higher oxygen mobility observed when iron is present in crystal lattices guarantees a higher cyclability, which is almost completely loss in manganese-doped samples.[90]

Strontium-rich materials (LS40CF, LS40CM) have a good-to-high oxygen release, a behaviour expected from this doping since the +2 oxidation state enhances the formation of M(IV) species in the B-site, which are more readily reduced in the thermal treatment. Besides, they present very good cyclability, with losses as low as 28% and 13% respectively. These materials appear to be the most promising for large-scale applications, in particular LS40CF, with an oxygen release of 9.17 mL/g in the second cycle, higher than LSC.

Differentiating oxygen release in temperature steps allowed to have an insight on the mechanism of this reaction, sometimes overlooked by the literature, in which only net releases up to a certain temperature are usually reported.[98–100] Two peaks, due to α-oxygen (from surface) and β-oxygen (from grain boundaries) can be observed for LSC, at 450 °C and 800 °C respectively. Furthermore, a contribution from bulk oxygen is revealed by the steady increase in oxygen release at higher temperatures. While in the case of Co-Fe perovskites this can be seen only in the one with 40% Sr, in Co-Mn materials all first cycles show a maximum for the first step, indicating that a similar mechanism is in action.

Nevertheless, some aspects would need further clarification. While characterising the materials, a trend in crystallite size emerged: this value increased with increasing cobalt content both in LSCF and LSCM families. In a similar way, specific surface area decreased with increasing strontium content, with LS40CF and LS40CM having lower area than other materials in their family. They proved to be very active nonetheless, suggesting that this characteristic might be to some extent secondary in the development of this kind of catalysts.

Besides, all values have been obtained while oxidizing the reacted sample in oxygen atmosphere. To evaluate the actual production of hydrogen from this series of materials,

some measurements should be conducted in water vapour flow at appropriate temperatures (in literature, $T_{ox} = 800\,^{\circ}\mathrm{C}$ is suggested as efficient reaction temperature).

Despite needing additional investigation on some specific aspects, these materials seem overall promising: the activity is comparable or superior to literature references, while working at a much lower temperature. Mn shows good activity but low cyclability, while Fe has the opposite features, except with a higher strontium content, which gives the best result. It is not excluded that a double B-site doping, both with Fe and Mn, could overcome some of the issues that each ion shows (if taken individually) and perform well even in a real condition of water splitting.

References

[1] H. Lee, J. Romero, Synthesis report of the IPCC sixth Assessment Report, IPCC, **2023**.

[2] IEA, Global Energy Review 2021, **2021**.

[3] J. Speirs, M. Contestabile, Y. Houari, R. Gross, *Renewable and Sustainable Energy Reviews* **2014**, *35*, 183–193, DOI https://doi.org/10.1016/j.rser.2014.04.018.

[4] M. Fischer, M. Werber, P. V. Schwartz, *Energy Policy* **2009**, *37*, 2639–2641, DOI https://doi.org/10.1016/j.enpol.2009.02.030.

[5] S. J. Davis, N. S. Lewis, M. Shaner, S. Aggarwal, D. Arent, I. L. Azevedo, S. M. Benson, T. Bradley, J. Brouwer, Y.-M. Chiang, C. T. M. Clack, A. Cohen, S. Doig, J. Edmonds, P. Fennell, C. B. Field, B. Hannegan, B.-M. Hodge, M. I. Hoffert, E. Ingersoll, P. Jaramillo, K. S. Lackner, K. J. Mach, M. Mastrandrea, J. Ogden, P. F. Peterson, D. L. Sanchez, D. Sperling, J. Stagner, J. E. Trancik, C.-J. Yang, K. Caldeira, *Science* **2018**, *360*, DOI 10.1126/science.aas9793.

[6] S. M. M. Ehteshami, S. Chan, *Energy Policy* **2014**, *73*, 103–109, DOI https://doi.org/10.1016/j.enpol.2014.04.046.

[7] N. Armaroli, V. Balzani, *ChemSusChem* **2011**, *4*, 21–36, DOI https://doi.org/10.1002/cssc.201000182.

[8] IEA, Global Hydrogen Review 2022, **2022**.

[9] M. F. Vostakola, B. Salamatinia, B. A. Horri, *Energies* **2022**, *15*, DOI 10.3390/en15031209.

[10] M. A. Khan, T. Al-Attas, S. Roy, M. M. Rahman, N. Ghaffour, V. Thangadurai, S. Larter, J. Hu, P. M. Ajayan, M. G. Kibria, *Energy Environ. Sci.* **2021**, *14*, 4831–4839, DOI 10.1039/D1EE00870F.

[11] V. K. Budama, J. P. R. Duarte, M. Roeb, C. Sattler, *Solar Energy* **2023**, *249*, 353–366, DOI 10.1016/j.solener.2022.11.001.

[12] D. Oudejans, M. Offidani, A. Constantinou, S. Albonetti, N. Dimitratos, A. Bansode, *Energies* **2022**, *15*, DOI 10.3390/en15093044.

[13] M. A. Peña, J. L. Fierro, *Chemical Reviews* **2001**, *101*, 1981–2017, DOI 10.1021/cr980129f.

[14] Y. Teraoka, M. Yoshimatsu, N. Yamazoe, T. Seiyama, *Chemistry Letters* **1984**, 893–896.

[15] Y. Tamaura, Y. Ueda, J. Matsunami, N. Hasegawa, M. Nezuka, T. Sano, M. Tsuji, *Solar Energy* **1999**, *65*, 55–57, DOI https://doi.org/10.1016/S0038-092X(98)00087-5.

[16] S. Lorentzou, D. Dimitrakis, A. Zygogianni, G. Karagiannakis, A. Konstandopoulos, *Solar Energy* **2017**, *155*, 1462–1481, DOI https://doi.org/10.1016/j.solener.2017.07.001.

[17] S. Abanades, *Energies* **2022**, *15*, DOI 10.3390/en15197061.

[18] T. Kodama, N. Gokon, R. Yamamoto, *Solar Energy* **2008**, *82*, 73–79, DOI 10.1016/j.solener.2007.03.005.

[19] R. R. Bhosale, G. Takalkar, P. Sutar, A. Kumar, F. AlMomani, M. Khraisheh, *International Journal of Hydrogen Energy* **2019**, 34–60, DOI 10.1016/j.ijhydene.2018.04.080.

[20] F. A. C. Oliveira, M. A. Barreiros, A. Haeussler, A. P. Caetano, A. I. Mouquinho, P. M. O. e Silva, R. M. Novais, R. C. Pullar, S. Abanades, *Sustainable Energy and Fuels* **2020**, *4*, 3077–3089, DOI 10.1039/d0se00318b.

[21] Y. Hao, C.-K. Yang, S. M. Haile, *Chemistry of Materials* **2014**, *26*, 6073–6082, DOI 10.1021/cm503131p.

[22] A. Haeussler, S. Abanades, J. Jouannaux, A. Julbe, *Catalysts* **2018**, *8*, DOI 10.3390/catal8120611.

[23] A. Pérez, M. Orfila, M. Linares, R. Sanz, J. Marugán, R. Molina, J. A. Botas, *Catalysis Today* **2022**, *390-391*, 22–33, DOI 10.1016/j.cattod.2021.12.014.

[24] M. Orfila, M. Linares, A. Pérez, I. Barras-García, R. Molina, J. Marugán, J. A. Botas, R. Sanz, *International Journal of Hydrogen Energy* **2022**, *47*, 41209–41222, DOI 10.1016/j.ijhydene.2022.03.077.

[25] Y. Mao, Y. Gao, W. Dong, H. Wu, Z. Song, X. Zhao, J. Sun, W. Wang, *Applied Energy* **2020**, *267*, DOI 10.1016/j.apenergy.2020.114860.

[26] M. M. Nair, S. Abanades, *Sustainable Energy Fuels* **2018**, *2*, 843–854, DOI 10.1039/C7SE00516D.

[27] A. Demont, S. Abanades, E. Beche, *Journal of Physical Chemistry C* **2014**, *118*, 12682–12692, DOI 10.1021/jp5034849.

[28] V. M. Goldschmidt, *Naturwissenschaften* **1926**, *14*, 477–485.

[29] M. Johnsson, P. Lemmens, **2007**, DOI https://doi.org/10.1002/9780470022184.hmm411.

[30] R. D. Shannon, *Acta Crystallographica Section A* **1976**, *32*, 751–767, DOI 10.1107/S0567739476001551.

[31] M. Ezbiri, V. Becattini, M. Hoes, R. Michalsky, A. Steinfeld, *ChemSusChem* **2017**, *10*, 1517–1525, DOI 10.1002/cssc.201601869.

[32] C. K. Yang, Y. Yamazaki, A. Aydin, S. M. Haile, *Journal of Materials Chemistry A* **2014**, *2*, 13612–13623, DOI 10.1039/c4ta02694b.

[33] M. Kubicek, A. H. Bork, J. L. Rupp, *Journal of Materials Chemistry A* **2017**, *5*, 11983–12000, DOI 10.1039/c7ta00987a.

[34] X. Wu, K. Onuki, *Tsinghua Science and Technology* **2005**, *10*, 270–276, DOI 10.1016/S1007-0214(05)70066-3.

[35] L. Nalbandian, A. Evdou, V. Zaspalis, *International Journal of Hydrogen Energy* **2009**, *34*, 7162–7172, DOI 10.1016/j.ijhydene.2009.06.076.

[36] S. Dey, B. S. Naidu, C. N. Rao, *Chemistry - A European Journal* **2015**, *21*, 7077–7081, DOI 10.1002/chem.201500442.

[37] L. Wang, M. Al-Mamun, Y. L. Zhong, L. Jiang, P. Liu, Y. Wang, H. G. Yang, H. Zhao, *Sustainable Energy and Fuels* **2017**, *1*, 1013–1017, DOI 10.1039/c6se00097e.

[38] X. Qian, J. He, E. Mastronardo, B. Baldassarri, C. Wolverton, S. M. Haile, *Chemistry of Materials* **2020**, *32*, 9335–9346, DOI 10.1021/acs.chemmater.0c03278.

[39] H. Shi, V. R. Bhethanabotla, J. N. Kuhn, *Journal of CO2 Utilization* **2021**, *51*, DOI 10.1016/j.jcou.2021.101638.

[40] ECHA, REACH - Registration, Evaluation, Authorisation and Restriction of Chemicals Regulation.

[41] Y. R. Wang, H. L. Tao, Y. Cui, S. M. Liu, M. He, B. Song, J. K. Jian, Z. H. Zhang, *Chemical Physics Letters* **2020**, *757*, DOI 10.1016/j.cplett.2020.137879.

[42] S. B. Şanlı, B. Pişkin, *International Journal of Hydrogen Energy* **2022**, *47*, 19411–19421, DOI 10.1016/j.ijhydene.2021.12.047.

[43] S. Chen, H. Cheng, Y. Liu, X. Xiong, Q. Sun, Q. Xu, X. Lu, S. Li, *Physical Chemistry Chemical Physics* **2022**, *24*, 28975–28983, DOI 10.1039/d2cp03931a.

[44] P. Anastas, N. Eghbali, *Chem. Soc. Rev.* **2010**, *39*, 301–312, DOI 10.1039/B918763B.

[45] F. Fresno, R. Fernández-Saavedra, M. B. Gómez-Mancebo, A. Vidal, M. Sánchez, M. I. Rucandio, A. J. Quejido, M. Romero, *International Journal of Hydrogen Energy* **2009**, *34*, 2918–2924, DOI 10.1016/j.ijhydene.2009.02.020.

[46] N. B. Goikoetxea, M. B. Gómez-Mancebo, R. Fernández-Saavedra, F. García-Pérez, J. A. Jiménez, J. Rodríguez, I. Rucandio, A. J. Quejido, *International Journal of Hydrogen Energy* **2016**, *41*, 16696–16704, DOI 10.1016/j.ijhydene.2016.07.085.

[47] T. Sano, M. Kojima, N. Hasegawa, M. Tsuji, Y. Tamaura, THERMOCHEMICAL WATER-SPLITTING BY A CARBON-BEARING Ni(I1) FERRITE AT 300°C, **1996**, pp. 781–787.

[48] C. Marcilly, P. Courty, B. Delmon, *Journal of The American Ceramic Society-Discussions and Notes* **1970**, *53*, 56–57.

[49] D. Pinto, A. Glisenti, *Catalysis Science and Technology* **2019**, *9*, 2749–2757, DOI 10.1039/c9cy00210c.

[50] A. Glisenti, M. Pacella, M. Guiotto, M. M. Natile, P. Canu, *Applied Catalysis B: Environmental* **2016**, *180*, 94–105, DOI 10.1016/j.apcatb.2015.06.017.

[51] M. Pechini, Method of preparing lead and alkaline earth titanates and niobates and coating method using the same to form a capacitor, **1967**.

[52] M. Thommes, K. Kaneko, A. V. Neimark, J. P. Olivier, F. Rodriguez-Reinoso, J. Rouquerol, K. S. Sing, *Pure and Applied Chemistry* **2015**, *87*, 1051–1069, DOI doi:10.1515/pac-2014-1117.

[53] C. Giacovazzo, H. L. Monaco, G. Artioli, D. Viterbo, M. Milanesio, G. Gilli, P. Gilli, G. Zanotti, G. Ferraris, M. Catti, *Fundamentals of Crystallography*, Oxford University Press, **2011**, DOI 10.1093/acprof:oso/9780199573653.001.0001.

[54] A. L. Patterson, *Phys. Rev.* **1939**, *56*, 978–982, DOI 10.1103/PhysRev.56.978.

[55] S. Gražulis, D. Chateigner, R. T. Downs, A. F. T. Yokochi, M. Quirós, L. Lutterotti, E. Manakova, J. Butkus, P. Moeck, A. Le Bail, *Journal of Applied Crystallography* **2009**, *42*, 726–729, DOI 10.1107/S0021889809016690.

[56] K. Rida, M. A. Peña, E. Sastre, A. Martínez-Arias, *Journal of Rare Earths* **2012**, *30*, 210–216, DOI 10.1016/S1002-0721(12)60025-8.

[57] S. Polarz, B. Smarsly, *Journal of Nanoscience and Nanotechnology* **2002**, *2*, 581–612, DOI 10.1166/jnn.2002.151.

[58] J. C. Santos, M. J. Souza, J. A. Ruiz, D. M. Melo, M. E. Mesquita, A. M. G. Pedrosa, **2012**, *23*, 1858–1862, DOI https://doi.org/10.1590/S0103-50532012005000052.

[59] Q. N. Tran, O. Gimello, N. Tanchoux, M. Ceretti, S. Albonetti, W. Paulus, B. Bonelli, F. Di Renzo, *Catalysts* **2021**, *11*, DOI 10.3390/catal11030344.

[60] G. L. Dimas-Rivera, J. R. De la Rosa, C. J. Lucio-Ortiz, J. A. De los Reyes Heredia, V. G. González, T. Hernández, *Materials* **2014**, *7*, 527–541, DOI 10.3390/ma7010527.

[61] S. Weber, K. L. Abel, R. T. Zimmermann, X. Huang, J. Bremer, L. K. Rihko-Struckmann, D. Batey, S. Cipiccia, J. Titus, D. Poppitz, C. Kübel, K. Sundmacher, R. Gläser, T. L. Sheppard, *Catalysts* **2020**, *10*, DOI 10.3390/catal10121471.

[62] C. Li, Y.-W. Chen, *Thermochimica Acta* **1995**, *256*, 457–465.

[63] W. Jung, H. L. Tuller, *Energy and Environmental Science* **2012**, *5*, 5370–5378, DOI 10.1039/c1ee02762j.

[64] E. Brusamarello, G. Peron, F. Nigrelli, A. Glisenti, *Topics in Catalysis* **2022**, DOI 10.1007/s11244-022-01726-y.

[65] M. Kubicek, A. Limbeck, T. Frömling, H. Hutter, J. Fleig, *Journal of The Electrochemical Society* **2011**, *158*, B727–B734, DOI 10.1149/1.3581114.

[66] S. P. Jiang, J. G. Love, *Solid State Ionics* **2001**, *138*, 183–190.

[67] B. Koo, K. Kim, J. K. Kim, H. Kwon, J. W. Han, W. C. Jung, *Joule* **2018**, *2*, 1476–1499, DOI 10.1016/j.joule.2018.07.016.

[68] NIST, XPS database, https://srdata.nist.gov/xps/main_search_menu.aspx, [Online; accessed 20/09/2023], **2023**.

[69] ThermoFisher, XPS database, https://www.thermofisher.com/it/en/home/materials-science/learning-center/periodic-table.html, [Online; accessed 20/09/2023], **2023**.

[70] A. Nenning, A. K. Opitz, C. Rameshan, R. Rameshan, R. Blume, M. Hävecker, A. Knop-Gericke, G. Rupprechter, B. Klötzer, J. Fleig, *The Journal of Physical Chemistry C* **2016**, *120*, PMID: 26877827, 1461–1471, DOI 10.1021/acs.jpcc.5b08596.

[71] P. V. Gosavi, R. B. Biniwale, *Materials Chemistry and Physics* **2010**, *119*, 324–329, DOI 10.1016/j.matchemphys.2009.09.005.

[72] H.-M. Zhang, Y. Teraoka, N. Yamazoe, *Chemistry Letters* **1987**, 665–668.

[73] M. S. G. Baythoun, F. R. Sale, *Journal of Materials Science* **1982**, *17*, 2757–2769.

[74] N. A. Merino, B. P. Barbero, P. Grange, L. E. Cadús, *Journal of Catalysis* **2005**, *231*, 232–244, DOI 10.1016/j.jcat.2005.01.003.

[75] R. Lago, G. Bini, M. A. Peña, P. Peña, J. L. G. Fierro, *Journal of Catalysis* **1997**, *167*, 198–209.

[76] M. Futai, C. Yonghua, Louhui, *Kinet. Catal. Lett* **1986**, *31*, 47–53.

[77] F. Puleo, L. F. Liotta, V. L. Parola, D. Banerjee, A. Martorana, A. Longo, *Physical Chemistry Chemical Physics* **2014**, *16*, 22677–22686, DOI 10.1039/c4cp03214d.

[78] M. Pacella, A. Garbujo, J. Fabro, M. Guiotto, Q. Xin, M. M. Natile, P. Canu, P. Cool, A. Glisenti, *Applied Catalysis B: Environmental* **2018**, *227*, 446–458, DOI 10.1016/j.apcatb.2018.01.053.

[79] S. Ponce, M. A. Peña, J. L. G. Fierro, *Applied Catalysis B: Environmental* **2000**, *24*, 193–205.

[80] A. Wattiaux, L. Fournès, A. Demourgues, N. Bernaben, J. Grenier, M. Pouchard, *Solid State Communications* **1991**, *77*, 489–493, DOI https://doi.org/10.1016/0038-1098(91)90726-C.

[81] A. Tarjomannejad, A. Niaei, A. Farzi, D. Salari, P. R. Zonouz, *Catalysis Letters* **2016**, *146*, 1544–1551, DOI 10.1007/s10562-016-1788-4.

[82] S. Cimino, L. Lisi, R. Pirone, G. Russo, M. Turco, *Catalysis Today* **2000**, *59*.

[83] M. L. Rojas, J. L. G. Fierro, L. G. Tejuca, A. T. Bell, *Journal of Catalysis* **1990**, *124*, 41–51.

[84] Y. Zhu, Y. Sun, X. Niu, F. Yuan, H. Fu, *Catalysis Letters* **2010**, *135*, 152–158, DOI 10.1007/s10562-009-0034-8.

[85] L. Lisi, G. Bagnasco, P. Ciambelli, S. D. Rossi, P. Porta, G. Russo, M. Turco, *Journal of Solid State Chemistry* **1999**, *146*.

[86] Q. Yin, J. Kniep, Y. S. Lin, *Chemical Engineering Science* **2008**, *63*, 2211–2218, DOI 10.1016/j.ces.2008.01.016.

[87] N. Gokon, T. Hasegawa, S. Takahashi, T. Kodama, *Energy* **2008**, *33*, 1407–1416, DOI 10.1016/j.energy.2008.04.011.

[88] S. Royer, D. Duprez, S. Kaliaguine, *Catalysis Today* **2006**, *112*, 99–102, DOI 10.1016/j.cattod.2005.11.020.

[89] Y. He, X. Zhu, Q. Li, W. Yang, *AIChE Journal* **2009**, *55*, 3125–3133, DOI 10.1002/aic.11931.

[90] K. Zhao, F. He, Z. Huang, G. Wei, A. Zheng, H. Li, Z. Zhao, *Korean Journal of Chemical Engineering* **2017**, *34*, 1651–1660, DOI 10.1007/s11814-016-0329-6.

[91] M. Orfila, M. Linares, R. Molina, J. Á. Botas, R. Sanz, J. Marugán, *International Journal of Hydrogen Energy* **2016**, *41*, 19329–19338, DOI 10.1016/j.ijhydene.2016.07.041.

[92] A. H. Bork, M. Kubicek, M. Struzik, J. L. Rupp, *Journal of Materials Chemistry A* **2015**, *3*, 15546–15557, DOI 10.1039/c5ta02519b.

[93] R. B. Wexler, G. S. Gautam, E. B. Stechel, E. A. Carter, *Journal of the American Chemical Society* **2021**, *143*, 13212–13227, DOI 10.1021/jacs.1c05570.

[94] D. Fino, N. Russo, G. Saracco, V. Specchia, *Journal of Catalysis* **2003**, *217*, 367–375, DOI 10.1016/S0021-9517(03)00143-X.

[95] P. M. Rajaitha, S. Hajra, K. Mistewicz, S. Panda, M. Sahu, D. Dubal, Y. Yamauchi, H. J. Kim, *Journal of Materials Chemistry A* **2022**, *10*, 15906–15931, DOI 10.1039/d2ta01869a.

[96] I. Stenina, A. Yaroslavtsev, *Processes* **2022**, *11*, 56, DOI 10.3390/pr11010056.

[97] L. Wang, M. Al-Mamun, P. Liu, Y. Wang, H. G. Yang, H. Zhao, *Journal of Materials Science* **2018**, *53*, 6796–6806, DOI 10.1007/s10853-018-2004-2.

[98] E. Gager, M. Frye, D. McCord, J. Scheffe, J. C. Nino, *International Journal of Hydrogen Energy* **2022**, *47*, 31152–31164, DOI 10.1016/j.ijhydene.2022.07.052.

[99] D. Zhang, H. A. De Santiago, B. Xu, C. Liu, J. A. Trindell, W. Li, J. Park, M. A. Rodriguez, E. N. Coker, J. D. Sugar, A. H. McDaniel, S. Lany, L. Ma, Y. Wang, G. Collins, H. Tian, W. Li, Y. Qi, X. Liu, J. Luo, *Chemistry of Materials* **2023**, *35*, 1901–1915, DOI 10.1021/acs.chemmater.2c03054.

[100] J. E. Park, Z. J. Bare, R. J. Morelock, M. A. Rodriguez, A. Ambrosini, C. B. Musgrave, A. H. McDaniel, E. N. Coker, *Frontiers in Energy Research* **2021**, *9*, DOI 10.3389/fenrg.2021.750600.

Appendix A

A.1 SEM

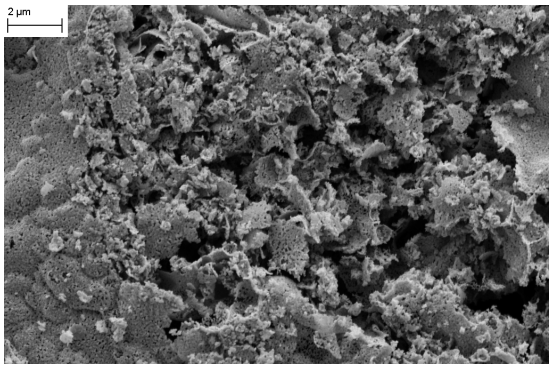

Figure A.1: LAN — 15000x

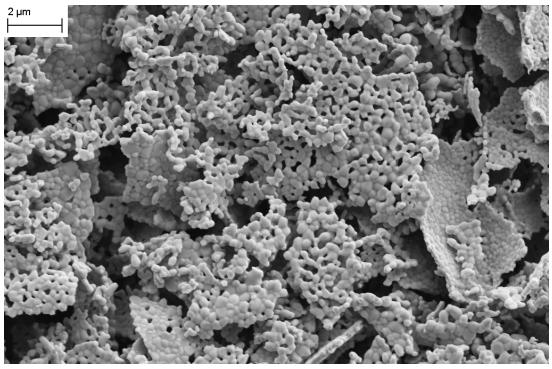

Figure A.2: LSC — 15000x

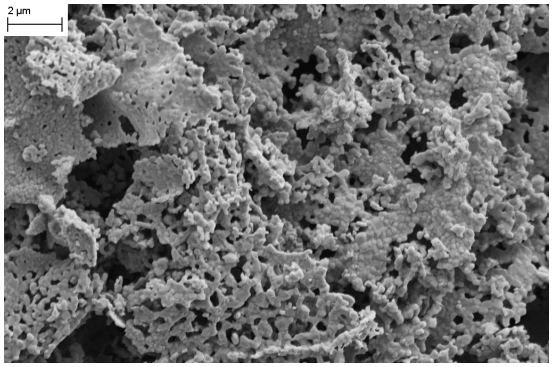

Figure A.3: LSCN10 — 15000x

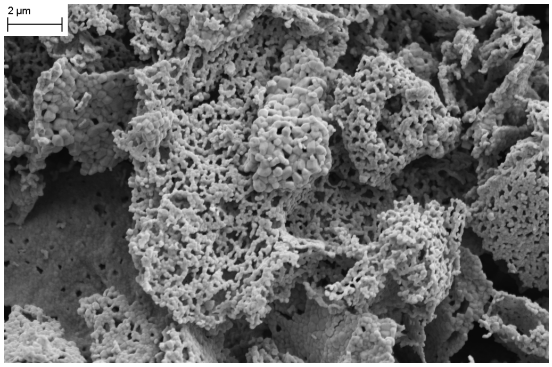

Figure A.4: LSCF50 — 15000x

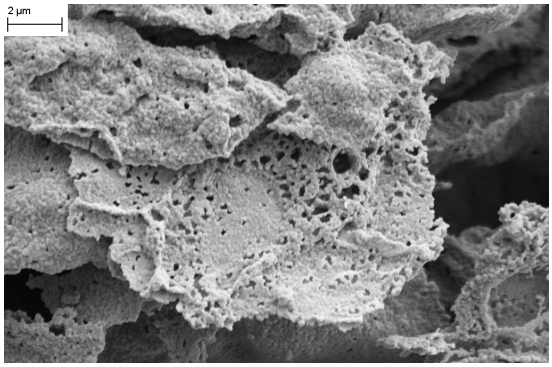

Figure A.5: LSCF25 — 15000x

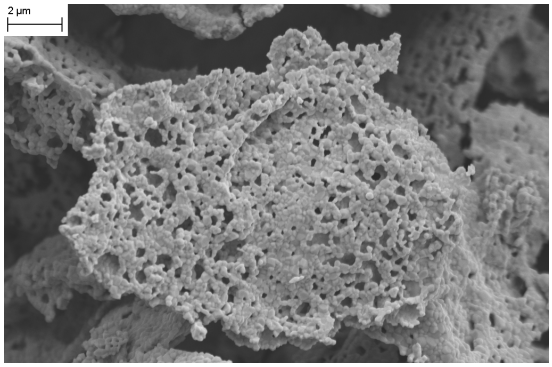

Figure A.6: LS40CF — 15000x

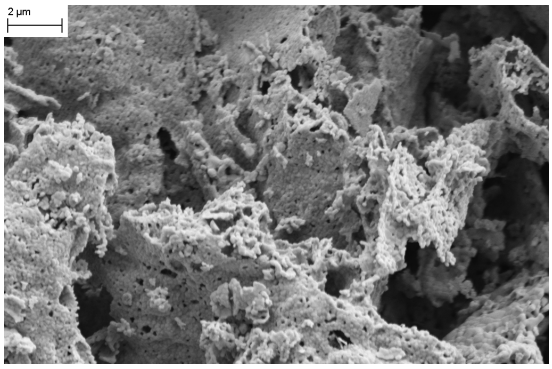

Figure A.7: LSCM50 — 15000x

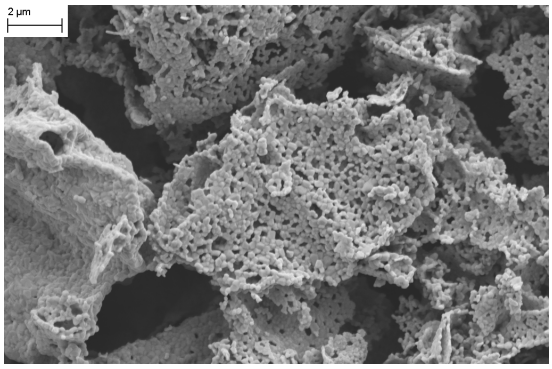

Figure A.8: LSCM25 — 15000x

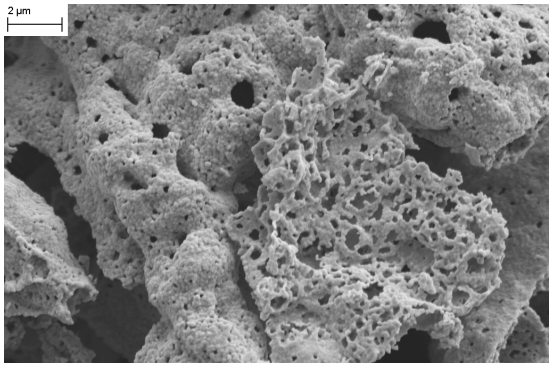

Figure A.9: LS40CM — 15000x

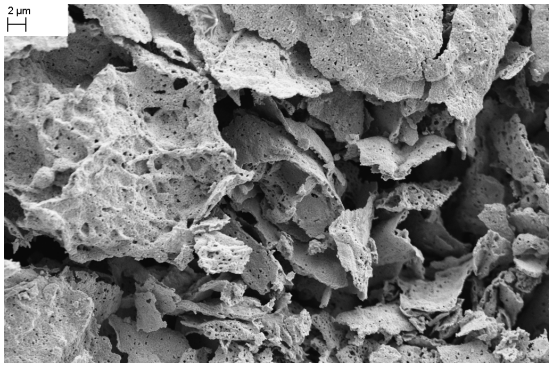

Figure A.10: LSCF25 post-reaction — 5000x

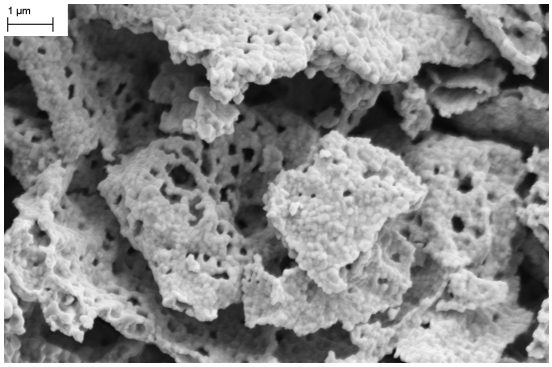

Figure A.11: LSCF25 post-reaction — 25000x

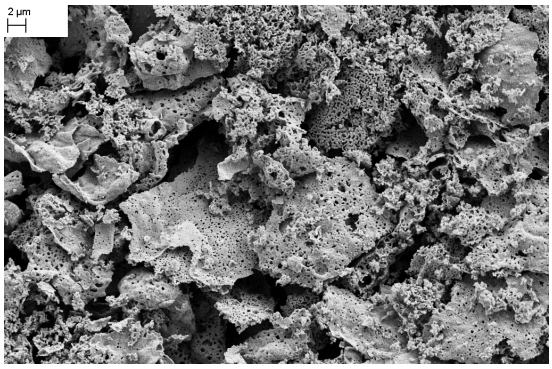

Figure A.12: LS40CF post-reaction — 5000x

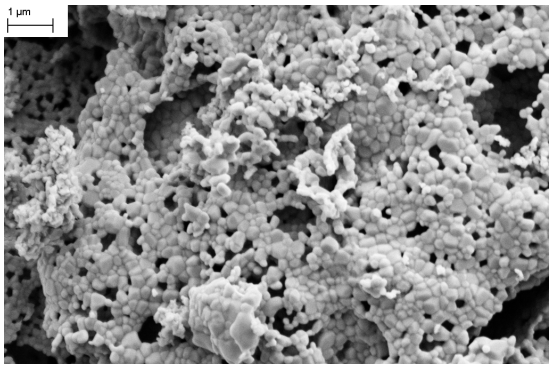

Figure A.13: LS40CF post-reaction — 25000x

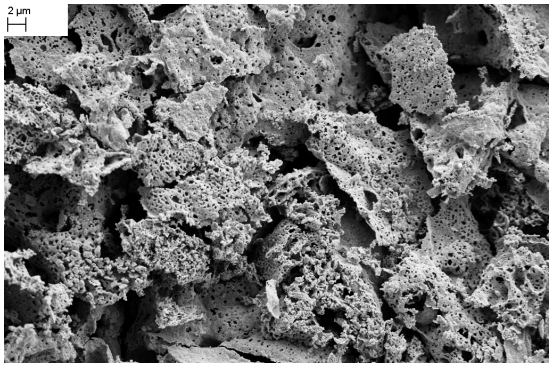

Figure A.14: LSCM25 post-reaction — 5000x

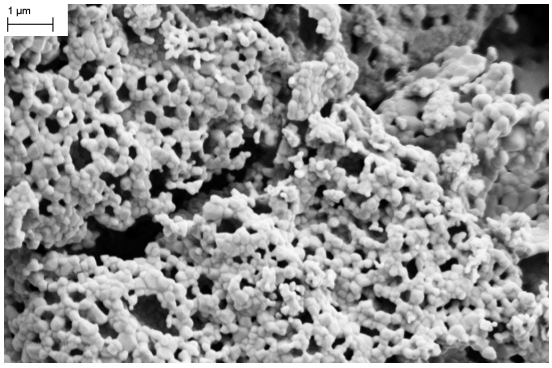

Figure A.15: LSCM25 post-reaction — 25000x

Figure A.16: LS40CM post-reaction — 5000x

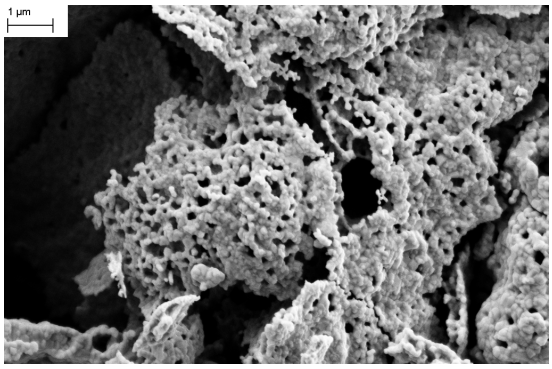

Figure A.17: LS40CM post-reaction — 25000x

A.2 BET

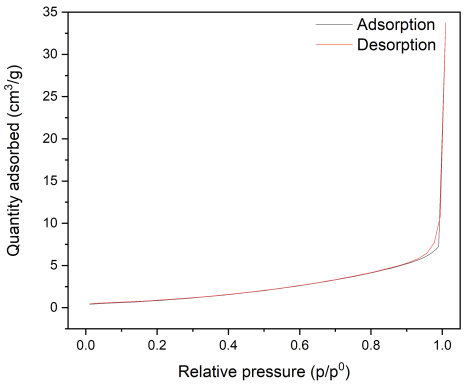

Figure A.18: Isotherms of LSC in N_2.

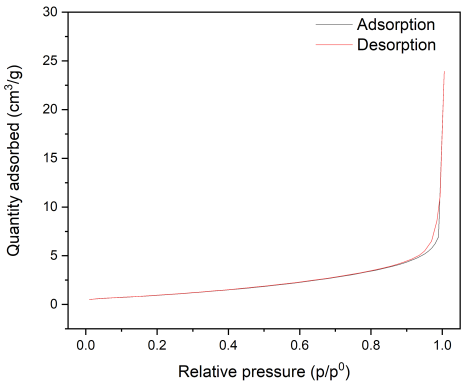

Figure A.19: Isotherms of LSCN10 in N_2.

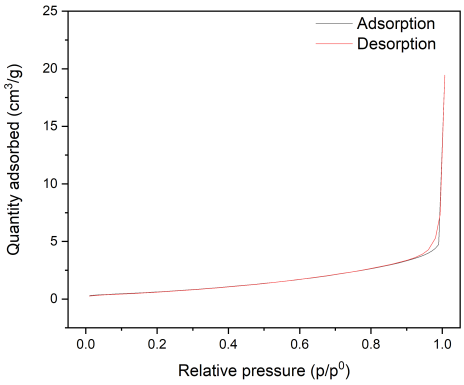

Figure A.20: Isotherms of LSCF50 in N_2.

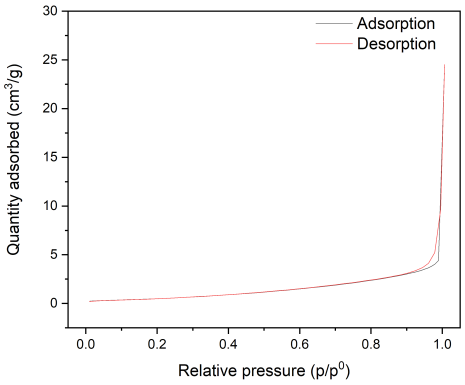

Figure A.21: Isotherms of LSCF25 in N_2.

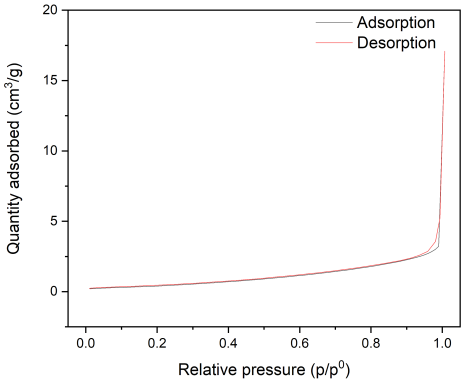

Figure A.22: Isotherms of LS40CF in N_2.

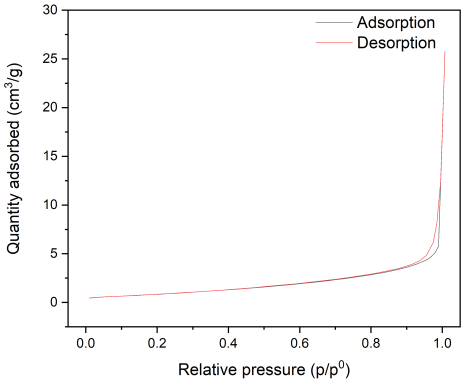

Figure A.23: Isotherms of LSCM50 in N_2.

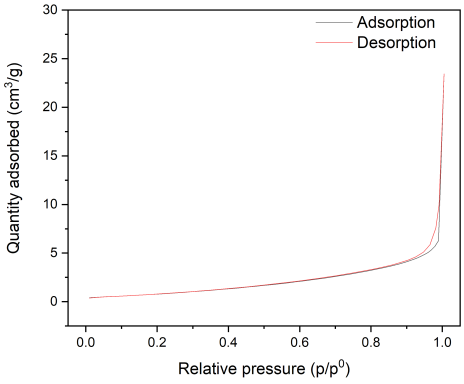

Figure A.24: Isotherms of LSCM25 in N_2.

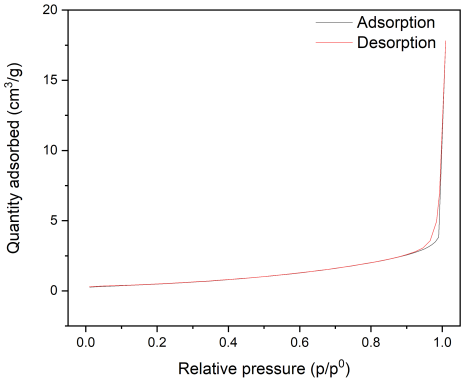

Figure A.25: Isotherms of LS40CM in N_2.

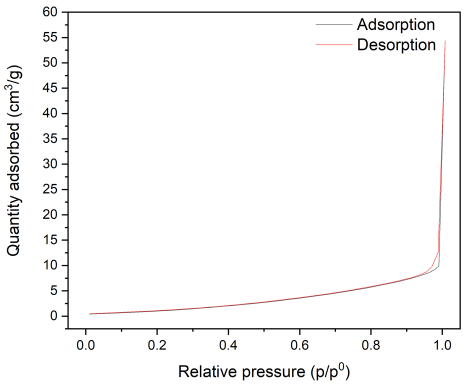

Figure A.26: Isotherms of post-reaction LSC in N_2.

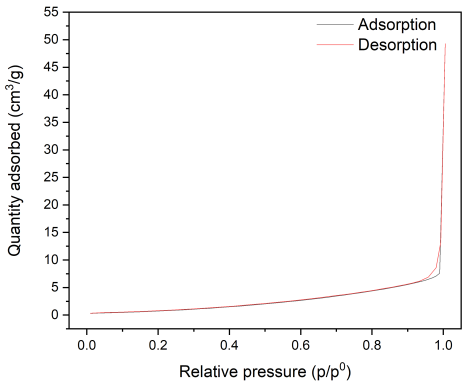

Figure A.27: Isotherms of post-reaction LSCF50 in N_2.

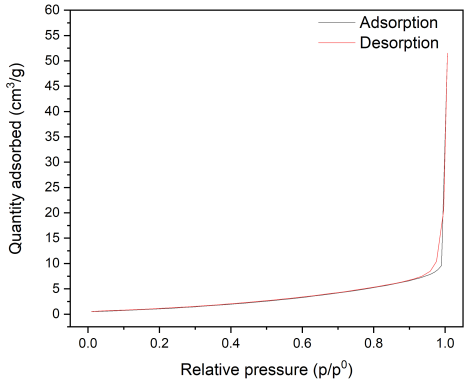

Figure A.28: Isotherms of post-reaction LSCM50 in N_2.

List of Figures

List of Tables

Acknowledgements

First of all, I need to thank my thesis supervisor prof. A. Glisenti, for her invaluable guidance both in this thesis work and in my life choices.

Working in the IMPACT group has taught me a wonderful way of doing research and working together which is well beyond being colleagues. In particular, I want to thank Simone C., which has thoroughly followed me in my research activity, and Chiara, Davide and Simone T. (in alphabetical order), for being companions of this journey, all having supported me physically and morally. All group members have given a contribution in my months here, and I want to name them all: Andrea, Lorenzo, Pietro, Jonathan, Gabriel, Enrico, Giacomo, Mattia, Beatrice, Matteo and Ambra.

A further thanks goes to my parents Stefania and Paolo, my brother Federico, my relatives and my girlfriend Emma; all my friends from Treviso, my hometown, with whom I have shared a decade of my life; my friends here in Padova, some of which have lived with me for the past five years. All of them have supported and sustained me for a relevant share of my life, some having endured me since day 0, while some other got to know me only when my sanity was somewhat more stable. Nevertheless, the fundamental contribution of each one of them is unquestionable, and if I am right here right now I have to thank each one of them.